ORGANIC-INORGANIC HYBRID SOLAR CELLS VIA ELECTROPOLYMERIZATION

By

WENCHUN FENG

A Dissertation submitted to the

Graduate School-New Brunswick

Rutgers, The State University of New Jersey

in partial fulfillment of the requirements

for the degree of

Doctor of Philosophy

Graduate Program in Chemistry

written under the direction of

Eric Garfunkel

and approved by

_____

_____

_____

_____

New Brunswick, New Jersey

May, 2014

ABSTRACT OF THE DISSERTATION

ORGANIC-INORGANIC HYBRID SOLAR CELLS VIA ELECTROPOLYMERIZATION

by WENCHUN FENG

Dissertation Director:
Eric Garfunkel

Integrating polymers with inorganic nanostructures is difficult due to wetting and surface energy considerations. We developed an electropolymerization method to grow conformal polymers on high aspect ratio nanostructures. Our method is shown to improve the polymer filling rate inside the nanostructures and can be used in the development of efficient hybrid solar cells. As an example, we have studied the hybrid system of electropolymerized polythiophene (e-PT) on a variety of conductive (Au and ITO) and semiconductive substrates (Si, Ge, ZnO). In particular, e-PT/ZnO hybrid structure can be further developed into organic photovoltaics (OPV). Although unsubstituted PT is not the ideal polymer material for high efficiency solar cells, it is an excellent choice for studying basic bonding and morphology in hybrid structures. We find that e-PT is covalently bound to the polar ZnO planar substrate via a Zn-S bond, adopting an upright geometry. By contrast, no strong covalent bonding was observed between e-PT and ZnO nanorods that consist of non-polar ZnO surfaces predominantly.

Energy level alignment at interfaces is critical for fundamental understanding and optimization of OPV as band offsets of the donor and acceptor materials largely determine the open circuit voltage (V_{oc}) of the device. Using ultraviolet photoemission spectroscopy (UPS) and inverse photoemission spectroscopy (IPS), we examined the correlation between

energy alignment and photovoltaic properties of a model hybrid solar cell structure incorporating undoped electrodeposited polythiophene (e-PT) films on ZnO planar substrates. The electrolyte anion (BF_4^-, PF_6^-, ClO_4^- or $CF_3SO_3^-$) used in the electrodeposition solution was found to exert a strong influence on the neutral e-PT film morphology and adhesion, the band alignment at the interface, and ultimately the photovoltaic behavior. The interfacial dipole lowers polythiophene energy levels, increasing the theoretical and actual V_{oc} in polythiophene/ZnO photovoltaics.

Our electropolymerization approach to integrate the organic and inorganic phases aims at understanding the chemistry at the interface, and the electronic and morphological properties of the system. This work should be generally applicable to other conjugated polymers and nanostructures, and it contributes to an understanding of organic-inorganic interfaces and electronic structures that may be advantageous to a range of electronic/photonic applications.

Acknowledgement

First of all, I would like to acknowledge my thesis advisor, Prof. Eric Garfunkel, for his endless support and guidance throughout my graduate career. When I first joined the group, he gave me time and freedom to choose what I would like to accomplish for my thesis project. He has acute observation and offers useful advice on how to overcome the scientific challenges. With his help and approval, I was able to go back to my hometown and visited Jilin University on two occasions, once with him for a short period of 10 days and the other as a visiting scholar for over two months. I value this precious experience and see it as a maturing process for me as a scientist, as it is the first time I have led a team of both students and young professors to investigate collaborative projects.

I would also like to thank Dr. Alan S. Wan, a colleague who took on the mentoring role for me when I first joined the group. His immense knowledge on ultra-high-vacuum system proves to be a catalyst for my adjustment into the group. I would like to extend my grateful thanks to all the other members (past and present) of Garfunkel group: Dr. Chien-Lan Hsueh, Dr. Lei Yu, Dr. Lauren Klein, Feixiang Luo, Szu-Ying Wang, Dr. Ning Wu, Yi Xu, Aleksandra Biedron and Malathi Kalyanikar. In addition, I'd like to thank colleagues from the Gustafsson group and Feldman group for their help: Prof. Torgny Gustafsson, Prof. Leonard Feldman, Dr. Hong Dong Lee, Can Xu and Dr. Samir Shubeita. Together we make a great surface science team. Special thanks to Prof. Len Feldman for giving a beautifully written book about how to write a dissertation, which is a relief to read during long hours of work and a magic bullet for writing this thesis.

For the majority of the UPS work, Dr. Sylvie Rangan from Bartynski group deserves many thanks because of the hours and thinking she put into the experiments, analysis and

paper corrections/comments. It is such a pleasure to work with an expert on photoemission and I learned a lot from her constructive critiques.

Other scientists I'd like to acknowledge: Dr. Leszek Wielunski, a world-class RBS expert, carried out many measurements for my samples. He has just retired and I will miss him dearly. Dr. Alexei Ermikov, for assistance with troubleshooting instruments. Dr. Tom Emge, a great XRD scientist, helped analyze ZnO and polymer samples. Bill Schneider, from the Physics machine shop, helped me make the sample stages and masks. Yan Cao and her advisor Prof. Elena Galoppini, from Chemistry Department at Rutgers Newark Campus, offered their help on the FTIR-ATR measurements. Prof. Gene Hall, helped me with Raman measurements. Dr. Steve Miller, as well as Dr. Sukanya Murali, offered generous help on SEM and sputtering deposition training. Rajesh Kappera, for teaching me how to use the solar simulator and the electrical testing station.

I would like to thank my committee members Prof. Jing Li and Prof. Ralf Warmuth. They have provided me with support and guidance throughout my entire graduate career.

Finally, I would like to thank my parents for their unconditional love and for all the valuable life lessons that I keep on reaping rewards with. I will not be where I am without you.

Table of Contents

List of Tables

Chapter 3. Electropolymerization of Polythiophene on Au, ITO, Ge, Si

Chapter 4. Electropolymerization of Polythiophene on ZnO

List of Illustrations

Chapter 1. Introduction

Chapter 2. Experimental Methods

Chapter 3. Electropolymerization of Polythiophene on Au, ITO, Ge, Si

Chapter 4. Electropolymerization of Polythiophene on ZnO

Chapter 1. Introduction

1.1 Solar Cells Rising

The detrimental environmental and societal effects associated with our reliance on fossil fuels, including the emission of CO_2 and other greenhouse gases, have motivated intense research activities towards finding more environmental friendly energy conversion systems, especially those employing renewable energy resources. The current power consumption across the globe, 16.5 terawatts (TW) per year, represents only ~0.01% of the total solar energy reaching the earth's surface at 162,000 TW per year.[1, 2] The solar energy that hits the earth surface in one hour is about equal to the global energy consumption per year.[3] In reality, however, current solar energy capacity supplies much less than 1% of the energy consumed globally. Oil, coal and natural gas are the three leading conventional energy sources, followed by hydroelectricity and nuclear energy (characterized as "other fuel", but not renewable energy, in some reports) are the next two energy sources (Fig. 1-1-1).[4] Renewable forms of energy (wind, geothermal, solar, biomass and waste) accounted for 2.4% of global energy consumption in 2012,[4] among which solar photovoltaic (PV) installed capacity attributes 100 gigawatts (GW), a growth of 41% in 2012 compared to the previous year. Although the base number is small, the rapid growth shows the potential for an even higher fraction of energy consumed coming from solar sources in the future. By 2050, PV has been estimated to provide 11% of the global electricity production and in the process reduce CO_2 emission by 2.3 gigatonnes (Gt) per year.[3]

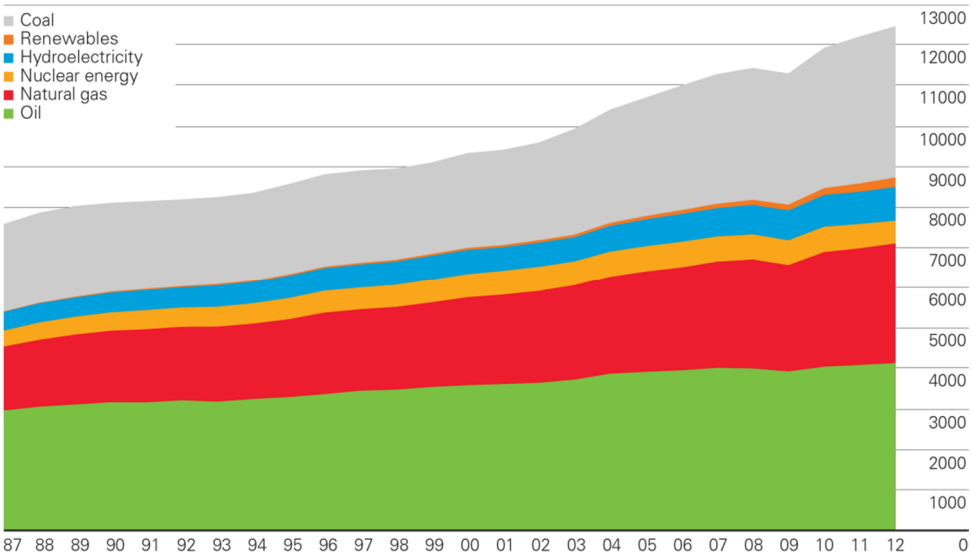

Fig. 1-1-1. World Energy Consumption by Energy Source[4]

The US Department of Energy (DOE) estimates that if the price of solar electricity can lower its prices to $0.33/W (this estimate may have to be further lowered to take into account of increased supply of fuel through hydraulic fracturing, or fracking), it will be cost-competitive with other non-renewable forms of electricity. This is not out of reach considering the current trend of module prices. From 2010 to 2012, the solar industry saw a precipitous cost decline of roughly $0.70/W to the current level of $0.50/W. This is made possible by oversupply, competitive pricing (or pricing below cost, which is considered dumping), and eroded profit margins in the polysilicon and PV materials market. The DOE cost goal is fast approaching, with estimation of $0.36/W (very close to the cost goal of $0.33/W) by 2017, with the majority of these cost declines deriving from technological innovations such as diamond wire sawing for PV wafers, advanced metallization solutions, and increased automation replacing manual labor.[5]

The PV market is predominately based on crystalline and polycrystalline Si technology which represents 85-90% of the market. The other 10-15% of the market share is occupied by thin film technologies, further divided into three main families: (1) amorphous (a-Si) and micromorph silicon (a-Si/μc-Si); (2) Cadmium-Telluride (CdTe); (3) Copper-Indium-Diselenide (CIS) and Copper-Indium-Gallium-Diselenide (CIGS). In terms of research-cell efficiencies (Fig. 1-1-2), the best performing solar cells, multi-junction solar cells, can achieve efficiencies up to 44%, but they are prohibitively expensive for mass consumption and have yet to penetrate the market. There are single junction GaAs solar cells approaching the 30% efficiency mark; thin-film Si and Si heterostructure technologies, approaching 20% and 25% efficiencies, respectively; CdTe and CIS/CIGS solar cells at approximately 20% efficiency, and emerging PVs (organic PVs and DSSC), the best of which have efficiencies in the range of 10-15%. Of the emerging PVs, organic photovoltaics (OPVs) have developed rapidly as they show high potential for low-cost manufacturing, without the need of vacuum processing. A key aspect of OPV technology is that the organic small molecule or polymer of interest would be inexpensive (if mass produced), has high optical absorption coefficients, is compatible with plastic substrates (therefore flexible), can be fabricated using mild-temperature high-throughput roll-to-roll processes. Another important aspect of the organic materials is its synthetic versatility, allowing for tailoring of properties from synthesis. Recently, there has been intensive research activity directed toward perovskite solar cells, [6, 7] made of methylammonium lead halide and are pushing the efficiency rapidly over 15% in only a few years. Although not regarded as a typical OPV material, there is considerably organic component in this solar cell system.

From the PV roadmap, one can see that the efficiency of OPVs, though starting very low at 3-4%, have quickly increased to over 11% in the past 10 years (Mitsubishi Chemicals, 11.1%, Fig. 1-1-3). However, although high efficiencies have been attained on a small scale laboratory cells, there is some uncertainty over how much the efficiency will drop when grown in industrial production. The submodules of OPVs achieved an efficiency of 8.2% on a cell area of 25 cm^2 by Toshiba, while a lower efficiency of 6.8% was reported also by Toshiba on a much larger submodule of 396 cm^2.[8] The efficiency drop in these two cases compared to the best performing OPVs in research conditions illustrates the scale-up issue which should be addressed when considering realistic efficiencies of OPVs. Another issue is the stability of OPVs. Silicon solar cells typically boast 20-30 years of lifetime, while studies for the lifetime of OPVs have just begun. There remains a lot of work to be done on improving the stability, but studies have shown that lifetime over 10,000 hours can be achieved. [9, 10]

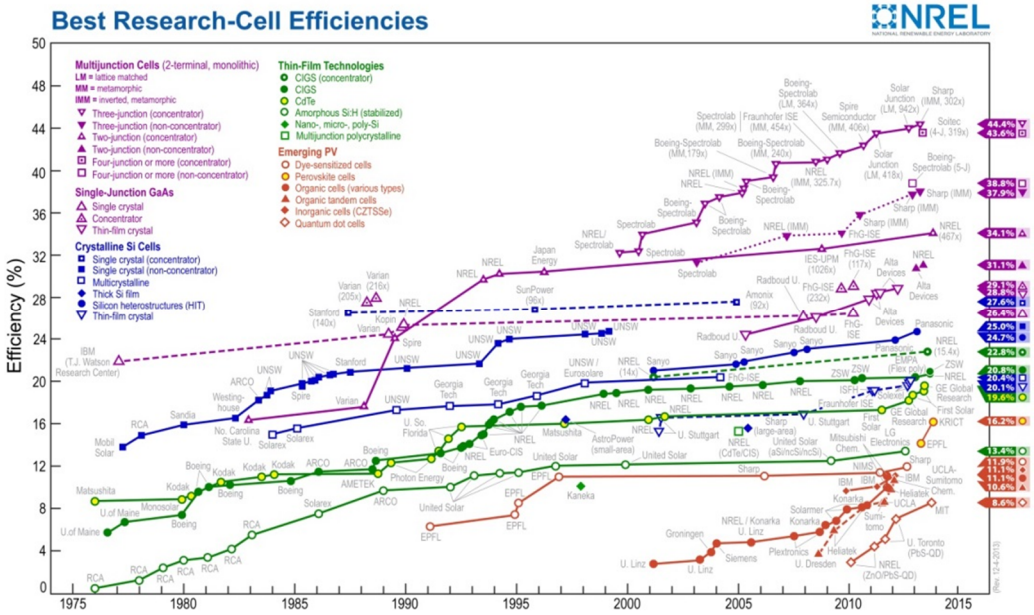

Fig. 1-1-2. Best Research-Cell Efficiencies Chart (NREL)

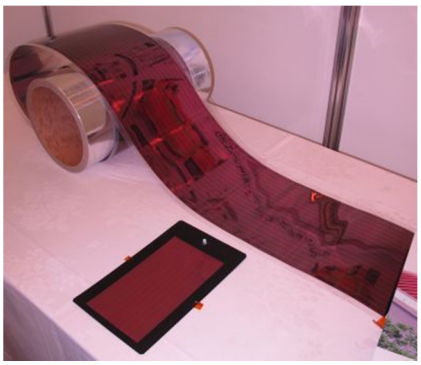

Fig. 1-1-3. Mitsubishi Chemical OPV Cell (the roll width is ~20 cm in this picture)

1.2 Motivation

Conducting conjugated polymers have received considerable attention in a wide range of electronic and opto-electronic technologies, including OPVs, organic light emitting diodes (OLEDs), organic thin film transistors and organic memory devices.[11] In particular, the p-type conducting polymer polythiophene (PT) and its derivatives [the most notable being poly(3-hexylthiophene), P3HT] have been among the most extensively studied materials for OPVs because of their optical properties, relatively high hole mobilities, synthetic versatility, and potential for cost-effective mass production.

One class of next-generation PVs, hybrid (organic-inorganic) solar cells, employ a p-type conducting polymer (such as the aforementioned PT) as the electron donor, and an n-type inorganic nanostructure as the electron acceptor. The hybrid architecture offers several potential advantages over its all-organic counterparts: considerably higher electron mobility in the inorganic phase, better morphological stability, and low-cost fabrication of the inorganic nanostructure. An ideal hybrid solar cell should have an

optimized nanostructure enabling efficient exciton diffusion, maximized interfacial area for charge separation and direct pathways for charge transfer.[12] High density ZnO nanorod arrays interdigitated with PT in which the two phases are in intimate contact, satisfactorily meets the requirement of such an ideal architecture. Herein, ZnO nanorods were chosen as the electron acceptor because they have relatively high electron mobility, have a reasonable energy gap and an appropriate band alignment with PT and other polymers at the interface. From a practical manufacturing perspective, ZnO has the advantages of high natural abundance, low cost, small environmental impact and non-toxicity. For the p-type conducting polymer, unsubstituted PT was chosen because it serves as a model system with a thiophene backbone and no side chains. Although PT is far from the ideal polymer system for high efficiency OPVs (which currently employ an alternating donor-acceptor polymer structure[13]), we are taking advantage of its simple molecular construction and ease of electropolymerization as our model polymer as opposed to more complex polymer structures.

The exciton diffusion length (a short one limits the exciton lifetime, and hence the efficiency of the system) in a conducting polymer system is typically less than 10 nm.[14] For efficient exciton diffusion to the organic-inorganic interface, the ZnO rod-to-rod spacing should be less than or equal to twice the exciton diffusion length. This small length scale makes it challenging for complete polymer infiltration into the ZnO nanorods. Conventional methods involve spin-coating and thermal or solvent vapor annealing, with limited success at filling into the nanorod arrays.[15-17] Vapor phase deposition has been explored as an alternative deposition technique.[18] The mechanism proposed was a multi-step process: upon heating the polymer chains were fragmented,

vaporized, transported to the substrate, and then re-polymerized once condensed. However, vapor phase deposition onto high aspect ratio surfaces such as ZnO nanorods has yet to be demonstrated. Another alternative method which involves chemical grafting of end-functionalized oligothiophenes and P3HT onto ZnO nanorods, has produced promising core-shell structures.[19] However, due to the nature of self-assembly, it is difficult to control the thickness of the polymer layer or grow polymer layers thicker than 20 nm. Integrating polymers into high-density arrays of ZnO nanorods to fabricate high quality core-shell and bulk heterojunction structures, was a key motivating factor for this work.

Electrodeposition (or electropolymerization, used synonymously in this thesis), where monomers in solution are polymerized onto the electrode surface to form oligomers and eventually polymers, is a logical pathway to enhance polymer infiltration due to its surface-initiated polymerization nature. Electrodeposition of conductive polymers has been developed as an efficient synthetic method since their discovery in the late 1970s.[20] Recently, there is renewed interest in the field of polymer electrodeposition as prospects for efficient organic or hybrid organic-inorganic solar cells have greatly improved.[21-26]

The polymerization starts with monomer adsorption onto the electrode, serving as anchor sites for subsequent polymer chain growth. Assuming that the adsorption is relatively uniform without cluster formation from initial nuclei, the hypothesis was that conformal polymer growth along the electrode surface could be attained and intimate contact between the electropolymerized-PT (e-PT) and the ZnO nanorods could be realized. Electropolymerization of monomers directly onto high density nanoscale

structures provides a promising alternative to standard polymer processing. First, because of their much smaller size, the steric hindrance of monomers diffusing into nanostructured materials will be much less than that of polymer chains. Secondly, because electropolymerization initiates from the surface,[20, 27] it should lead to a higher density organic-inorganic structures than conventional film deposition methods. The only requirement for electropolymerization is a sufficiently conductive electrode and polymer; this is adequately satisfied in our study.

There has been considerable research effort directed at incorporating electrodeposited polymers into PV devices. Electropolymerization has recently been applied to the fabrication of efficient hybrid solar cells. Exemplary reports include e-P3HT/CdS nanorods[23], e-P3HT/CdS/ZnO nanorods[24], e-PEDOT [Poly(3,4-ethylenedioxythiophene)]/ZnO nanorods[21] and e-P3HT[28] or e-PEDOT[26] on GaAs nanowires.

Despite extensive studies on select OPV systems, many fundamental questions remain unresolved or have been only cursorily examined. For example, since the polymer growth appears to achieve conformal coverage along the high-aspect ratio ZnO nanostructures, what is the nature of the interfacial bonding (chemical or physical adsorption)? How would a variety of electrochemical conditions (solvent, electrolyte, etc.) influence the electrodeposition process? In addition, we intend to shed light on the correlated relationship between the energy alignment at the interface and the photovoltaic properties. In turn, elucidating and taking advantage of such a correlation can lead to improvement of the solar cell performance. Utilizing a variety of synthetic methods (sol-gel, hydrothermal, electrochemical syntheses) and multiple surface and bulk

characterization techniques, we aim to contribute to the PV research community's understanding of hybrid solar cell materials and structures using our electrodeposited polymer/ZnO as a model system with a particular focus on the interface between the organic and inorganic phase, and to elucidate fundamental guidelines for optimizing such systems for high performance PV devices.

1.3 Outline

This thesis is structured as follows:

Following this introduction (Chapter 1), we present an overview of the experimental tools and methods used throughout the thesis and related work (Chapter 2).

In Chapter 3, we discuss PT electrodeposition on common conductive and semiconductive substrates, including Au, ITO, Si and Ge. This serves as background information, helpful before moving to electrodeposition on ZnO substrates.

In Chapter 4, the main body of the thesis, electrodeposition of PT on ZnO is discussed. This chapter is further divided into five sections. Section 4.1 discusses the growth conditions of ZnO films and nanorods. Nanorods growth can be controlled by a variety of factors, such as the growth time, growth temperature, solution concentration and substrate preparation conditions. Sections 4.2-4.5 examine the electrodeposition of PT on ZnO with a firm focus on the interface between the organic and the inorganic phase. Specifically, Section 4.2 focuses on the interfacial bonding of e-PT films on ZnO planar and nanorod substrates. Section 4.3 discusses the morphological control achieved on the e-PT/ZnO nanorods system. Section 4.4 outlines the correlation between the electronic energy level alignment and the photovoltaic properties of e-PT/ZnO film

devices. Section 4.5 discusses procedures needed to measure and understand device parameters and reviews results for PV device testing on our devices.

The Summary and Conclusions are discussed in Chapter 5.

Our approach of using electropolymerization to integrate the organic and inorganic phases, aims at understanding the chemistry at the organic-inorganic interface and the electronic/morphological properties of the electrodeposited polymer. Our work is generally applicable to other conjugated polymers and nanostructures and contributes to the understanding of the organic-inorganic interfaces and structures that are likely to be advantageous for solar cell applications.

1.4 Introduction to Organic Solar Cells

In 1985, Tang introduced an organic small molecule donor-acceptor bilayer OPV device with the donor as copper phthalocyanine (CuPc) and the acceptor as 3,4,9,10-perylenetetracarboxyl-bis-benzimidazole (PTCB) and achieved a power conversion efficiency (PCE) of ~1%.[29] This is the first demonstration that an OPV can achieve a significant PCE by selection of donor and acceptor molecules that have suitable offset energy bands to drive the exciton dissociation at the interface.

In Tang's bilayer device, the photogenerated excitons need to be close to the interface for dissociation to occur before recombination. The exciton diffusion length in conjugated polymer has been determined to be of order 10 nm.[14] The typical material thickness for optimal light absorption in these bilayer OPVs is ~100 nm, therefore the exciton diffusion length is much smaller than the typical thickness of the device and the

PCE is mainly limited by the number of absorbed photons within close proximity (~10 nm) to the interface.

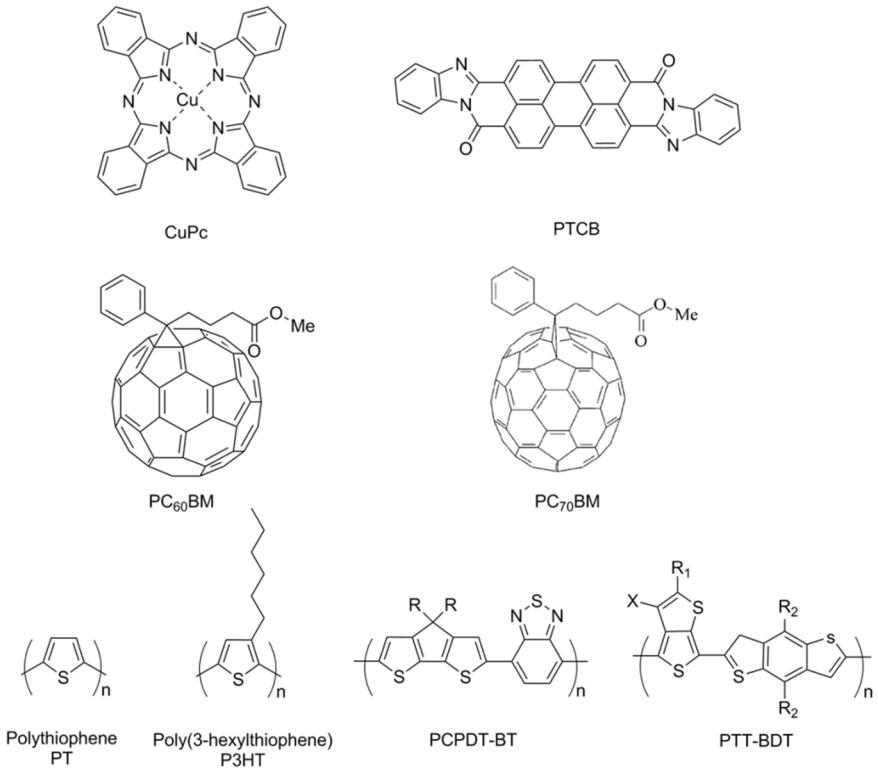

Fig. 1-4-1 Chemical Structures of representative donor and acceptor molecules and polymers

In order to bypass this problem and produce a large network of interpenetrating materials for more efficient photon absorption, OPVs consisting of two conjugated polymers intermixed within the active layer are produced in 1995.[30, 31] These polymer-polymer OPVs can be considered as one of the first bulk heterojunction (BHJ) solar cells made. This device structure made it possible that almost all excitons generated by photon excitation can diffuse to the interface for dissociation before recombination occurs.

Plagued by low PCE values at the beginning, improvements on the device morphology and better selection of the donor and acceptor polymers led to a PCE value of 1.9%.[32]

A major breakthrough in the OPV field at around this time is the usage of C_{60} and its derivatives (e.g. [6,6]-phenyl-C_{61}-butyric acid methyl ester, PCBM) as the acceptor material. [33] PCBM exhibits strong electronegativity and high electron affinity and forms advantageous interpenetrating percolating networks for both electrons and holes to be transported to the corresponding electrode when mixed with conjugated polymers such as P3HT. Polymer-C_{60} OPVs are one of the most extensive studied systems in the field and as of now still dominates the field of high efficiency OPVs.

1.5 New Materials

There has been considerable progress made on new polymer materials that have lower bandgap for more efficient light absorption and improved transport ability compared to P3HT, as well as new fullerene derivatives that exhibit better absorption relative to PCBM. The new polymer materials are designed to exhibit an alternating donor-acceptor structure or a structure that stabilizes the quinoidal form of the polymer.[11] The alternating donor-acceptor structure is the most common method to design a lower bandgap polymer, in which the "push-pull" forces between the donor and the acceptor units in the polymer facilitate electron delocalization and consequently hybridization of molecular orbitals and electron redistribution along the orbitals participating in hybridization. This results in two new hybrid orbitals which consist of a higher HOMO level and lower LUMO level, and thereby a narrower bandgap polymer.[11] One example is PCPDT-BT, which combines an electron donating dialkyl-cyclopentabithiophene

(CPDT) group and an electron accepting benzothiadiazole (BT) group, with a narrow bandgap of 1.4 eV.

The other method to lower the bandgap is to stabilize the quinoidal state. The ground state of the conjugated polymer can take on two possible states: the aromatic or the quinoidal state. The quinoidal structure is energetically less favorable due to the lower bandgap, therefore securing a stable quinoidal structure through polymer design will produce a lower bandgap polymer. It was found that the thieno[3,4-b]thiophene (TT) unit can stabilize the quinoidal structure of the backbone that narrows the bandgap of the resulting polymer to 1.6 eV.[34] This particular polymer has an alternating TT unit and benzodithiophene (BDT), in which the BDT unit was chosen because of its more extended conjugation and proper side chain patterns for improved solubility. Both of these newly designed polymer materials, PCPDT-BT and PTT-BDT, are incorporated in OPVs capable of reaching PCEs of 7-8%.

Development of new acceptor materials can also improve the PCE. C_{70} derivative $PC_{70}BM$, for example, is shown to have better absorption properties than C_{60}. Substituting the C_{60} with the C_{70} derivative often leads to an increase in J_{sc}.[35]

The above approaches for synthesizing novel polymer and acceptor materials, aim at improving the light absorption and consequently J_{sc}. However, it remains a challenge to improve both J_{sc} and V_{oc}. The reason is that a narrowed bandgap improves J_{sc}, however, V_{oc} may also decrease due to the higher HOMO levels that usually accompany such lowered bandgaps. It was recently shown to be possible to obtain a lower bandgap without upshifting the HOMO level of the polymer by structural fine-tuning. Introducing a fluorine atom into the TT unit of PTT-BDT downshifts the HOMO

and LUMO levels simultaneously, which maintains the low bandgap as well as enhances the V_{oc}.[34] As another example of this powerful method, inserting a strong electron-donating oxygen atom into the CPDT unit of the PCPDT-BT polymer resulted in a reduction in the bandgap of the resulting polymer. [36]

1.6 The Concept of Tandem Solar Cells

Tandem solar cells can take advantage of broader solar spectrum coverage and reduce the thermalization loss of photonic energy from the photon to electron conversion.[36] Typically the device is stacked with a high bandgap material in the front cell, which is responsible for absorption of high-energy (such as UV) photons and providing a higher V_{oc} than lower bandgap materials. Using PCPDT-BT as a synthetic template with some structural modification, a tandem solar cell with 10.6% efficiency was reported recently (Fig. 1-6-1).[36] However, it must be kept in mind that tandem solar cells are expected to be more expensive to manufacture than single junction solar cells. The scale-up of the polymer synthesis, the environmental impact of these polymer materials along with appropriate cost analysis of synthesizing a multiplayer polymer structure, have been lacking and these concerns need to be addressed before OPVs can transfer into success stories in the market. Indeed, there are other voices that expressed concern over whether OPVs by themselves will ever be commercially viable if not coupled with another high performing high V_{oc} solar cell such as CIGS solar cells as the top cell in a tandem structure.[37]

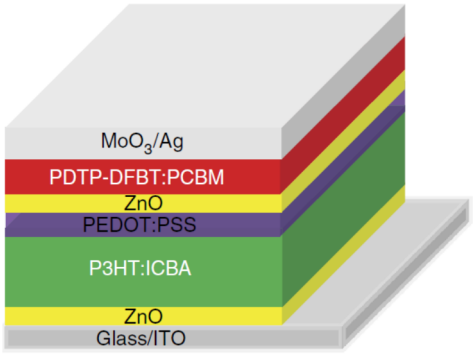

Fig. 1-6-1 Device structure of a tandem solar cell. Reused from Ref(36), which is open access and can be used for educational purposes without obtaining additional permission from Nature Publishing Group.

1.7 Design Rules for High Efficiency Solar Cells

1.7.1 Solar Cell Parameters

The *I-V* characteristics of a solar cell under illumination are shown in Fig. 1-7-1. In the fourth quadrant, the device generates power under illumination. At the maximum power point (*m*), the product of current and voltage is the largest. The fill factor, FF, represents the ideality of the diode and is defined as:

$$FF = \frac{V_m \times I_m}{V_{oc} \times I_{sc}}$$

where V_m and I_m represent the voltage and current at the maximum power point.

The PCE is defined as follows:

$$PCE = \frac{V_{oc} \times I_{sc} \times FF}{P_i} = \frac{P_m}{P_i}$$

where P_m is the maximum power output by the solar cell and P_i is the incident light power intensity. This intensity is standardized at 1000 W/m^2 with a spectral intensity distribution matching that of the sun on the earth's surface at an incident angle of 48.2°, which is called the AM 1.5 spectrum.

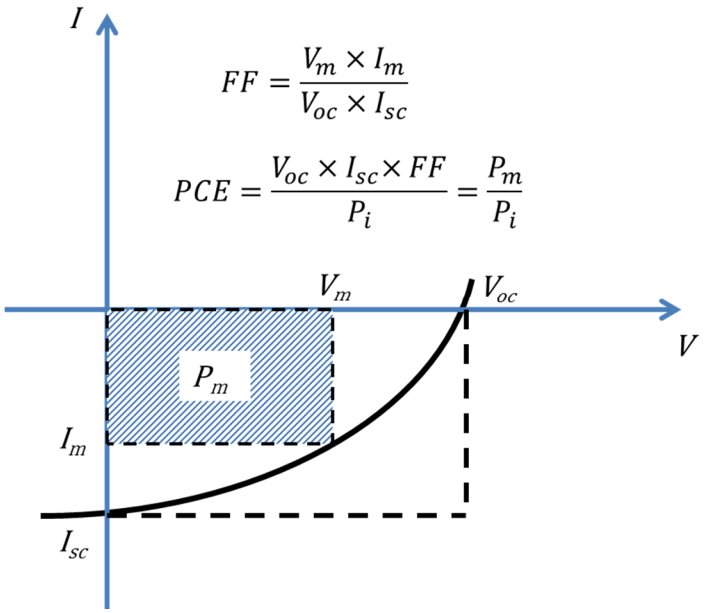

Fig. 1-7-1 Illustration of I-V curve of an OPV.

1.7.2 General Design Rules

From the above discussion, OPV efficiency is determined by V_{oc}, J_{sc} and FF. The commonly accepted design rules call for a more optimized donor-acceptor HOMO-LUMO offset for a higher V_{oc}, controlled active-layer morphology and thickness and improved charge carrier mobility for a higher J_{sc}. Out of the three parameters, the origins of V_{oc} and J_{sc} are the best understood. The theoretical maximum V_{oc} has been found to be:[38]

$$V_{oc}=|E^{Donor}HOMO| - |E^{Acceptor}LUMO| - 0.3\ V$$

where the 0.3 V loss is explained to be caused by dark current of the diode (~0.2 V) as well as the fact that the vast majority of photocurrent in BHJ devices is field-driven (~0.1 V).

High J_{sc} values can be achieved by optimizing the absorption window of the polymer, as well as its charge carrier mobility. A lower bandgap polymer will take advantage of a wider absorption window, while charge carrier mobility can be improved by designing a polymer with higher crystallinity and more packing order. However, the charge carrier mobility must be considered in connection with the balance of both charge carriers in the active layer and therefore the morphology of the polymer material as well as the acceptor material will have an impact on the carrier mobility issue.

FF is the ratio between the maximum obtainable power and the product of J_{sc} and V_{oc}, and remains the least understood parameter out of the three. It is affected by a variety of factors, including charge carrier mobility, recombination rates, series and shunt resistance, film morphology and donor/acceptor miscibility. In order to achieve a high FF, molecular planarity, molecular chain packing and carrier mobility should all be taken into account in structural design.[11]

The bandgap of the donor material (or polymer), E_g, and the LUMO level of the donor have been taken into consideration and a contour plot (Fig. 1-7-2) has been devised to illustrate how to achieve 10% efficiency for single junction solar cells. From the line that represents a donor HOMO level of -5.7 eV, one can see that a donor HOMO level just 0.3 eV above the HOMO level of PCBM may eventually lead to high efficiency if the donor bandgap is ~1.75 eV or lower. Such a polymer has not been synthesized yet. For example, one of the highest performing polymer materials, the

PDTP-DFBT, with PCPDT-BT as the backbone with some modification to fine-tune the HOMO and LUMO levels, has a HOMO level of ~5.3 eV, which is 0.7 eV (not 0.3 eV) higher than the acceptor HOMO level higher. Although the donor bandgap satisfied the requirement of being below 1.75 eV at 1.38 eV, the non-ideal HOMO level will lead to a smaller V_{oc} than the theoretical achievable V_{oc}.[36]

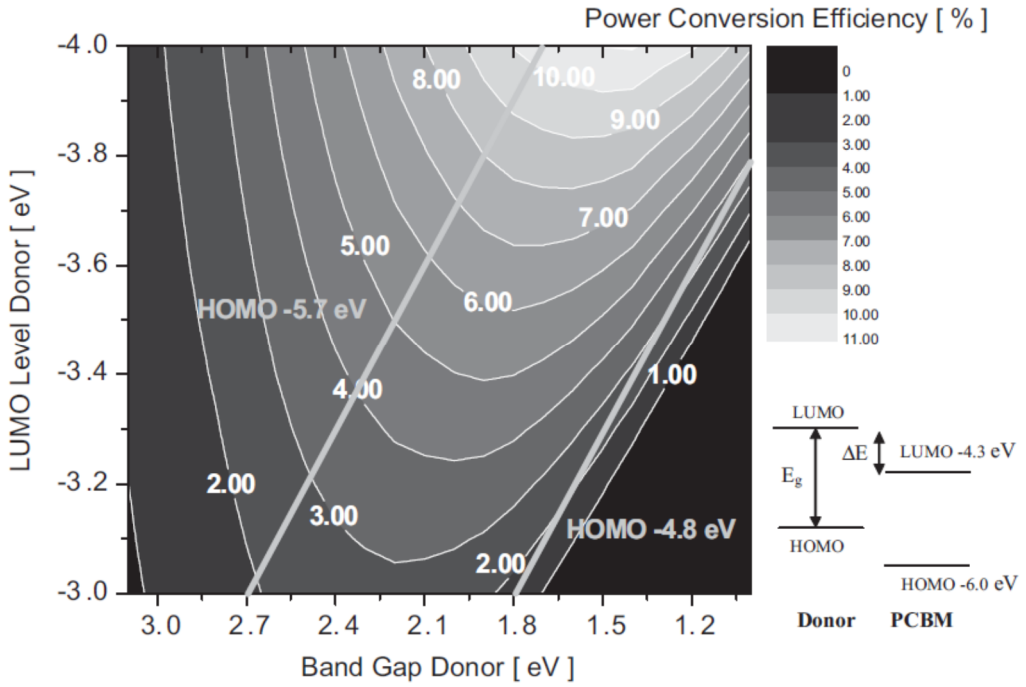

Fig. 1-7-2 A contour plot showing the calculated energy-conversion efficiency versus the bandgap and the LUMO level of the donor polymer according to the model described in this paper. Straight lines starting at 2.7 eV and 1.8 eV indicate HOMO levels of -5.7 eV and -4.8 eV, respectively. A schematic energy diagram of a donor-PCBM system with the bandgap energy (E_g) and the energy difference (ΔE) is also shown. Adapted with permission from Ref (38). Copyright © 2006 WILEY-VCH Verlag GmbH & Co. KGaA, Weinheim.

1.7.3 Morphology: Ideal Architecture

Aside from designing low bandgap polymers, as we have mentioned earlier the morphology of the two phases in the active layer critically impacts the J_{sc}. Therefore, manipulating the morphology in the active layer is crucial in achieving high performances. Thermal and solvent annealing are two most common methods to optimize the morphology in BHJ active layer. These annealing procedures mostly improve the crystallinity of the polymer, however, the basic architecture in the active layer of common BHJ cells is far from ideal. The charge transport within the two phases tends to be insufficient due to the lack of a straightforward and direct pathway to the corresponding electrodes. There is a lack of precise nanometer scale control in this complex morphology that is necessary to ensure that all photogenerated excitons will reach the interface for dissociation and separation before recombination. To eliminate these shortcomings in the traditional BHJ architecture, a new type of BHJ is introduced with a more ordered and controllable structure called ordered BHJ (Fig. 1-4-3).[39] In this architecture, ordered nanostructures interdigitated with the polymer material forming active layers. The stacking of donor and acceptor has to be interspaced with an average length scale of ~10 nm or less which is equal to the exciton diffusion length to ensure exciton diffusion and charge separation. This architecture will ensure that all of the photogenerated excitons can reach the interface without suffering from recombination. The two phases present direct pathways for charge carriers to reach the corresponding electrodes, minimizing charge transport time and reducing the probability of back electron transfer. Finally, a pure donor phase at the hole collecting electrode and a pure acceptor phase at electron collecting electrode should be placed, so as to minimize

carrier loss at the electrodes. Such an architecture has been suggested to be the "ideal" architecture in several reviews in the field.[12, 39, 40]

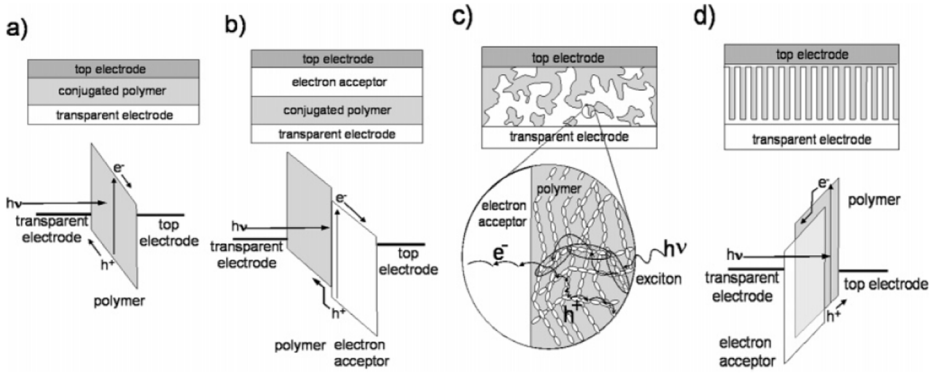

Fig. 1-7-3 Four device architectures of conjugated polymer-based OPVs. (a) single-layer PV cell; (b) bilayer PV cell; (c) traditional (disordered) BHJ; (d) ordered BHJ. Reprinted with permission from Ref (39). Copyright (2004) American Chemical Society

A simple way to achieve a nanoscale interdigitated architecture is to make use of vertically standing metal oxide nanorods or nanowire substrates as the n-type material and filling it with p-type polymers (P3HT in most cases) (Fig. 1-7-4),[41-43] though there is also one report on using the polymer fibers as a template and filling them with CdSe nanocrystals.[44] The nanorod or nanowires provide us with nm scale control over the morphology, as opposed to difficult-to-control morphology in traditional BHJs. An additional positive aspect of this architecture is the potential for higher stability, however, systematic studies concerning the stability of the hybrid solar cells must be carried out before we draw any conclusions.[40]

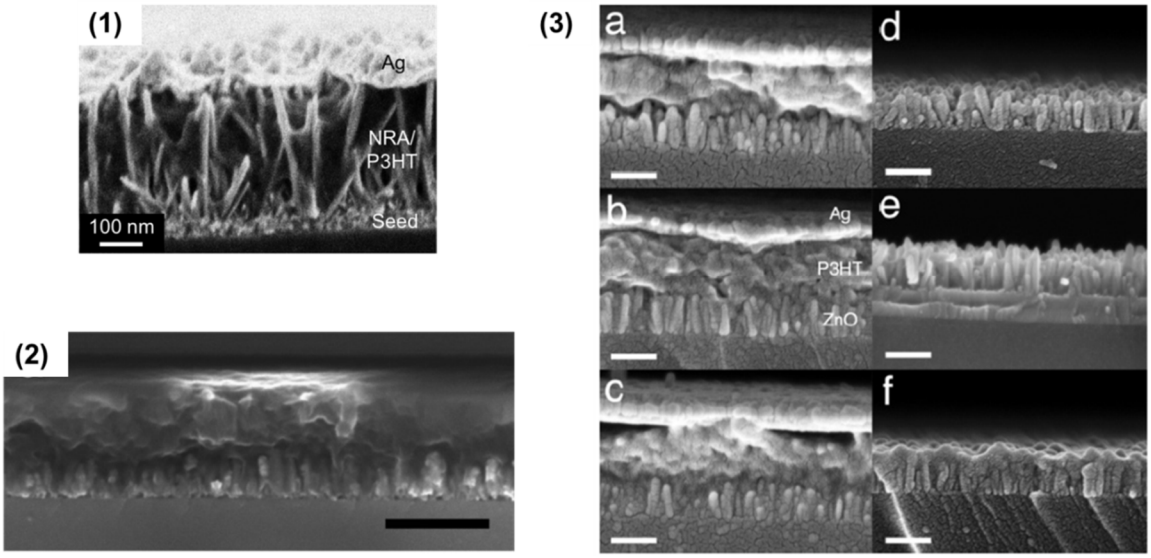

Fig. 1-7-4 (1) Cross-sectional SEM images of P3HT/ZnO nanorod PV devices with annealing at 225 °C. Reprinted with permission from Ref (41). Copyright (2009) American Chemical Society.

(2) Cross-sectional SEM image of P3HT/ZnO-TiO_2 array grown on silicon, with annealing at 220 °C. Scale bar = 200 nm. Reprinted with permission from Ref (42). Copyright (2007) American Chemical Society.

(3) Cross-sectional SEM images of P3HT/ZnO nanorod PV devices: without annealing (a); with annealing at 150 °C (b); with annealing at 225 °C (c). Also shown are images after removing the polymer on top of the rods: without annealing (d); with annealing at 150 °C (e); with annealing at 225 °C (f). Scale bar = 200 nm. Reprinted with permission from Ref (43). Copyright (2007) American Chemical Society.

ZnO nanorod-P3HT device systems have become prime examples in the pursuit of this ideal architecture. However, even with exhaustive optimization techniques the efficiency for such devices still remains low (< 1%).[45] It was thought that there should be

no intrinsic drawback for using these metal oxide nanostructures, because they do exhibit beneficial crystallinity and high electron mobility. However, the dimension of the ZnO nanorod arrays is not optimized to the ideal 10 nm spacing throughout the substrate. In fact, the ZnO nanorod arrays show relatively large rod-to-rod spacing which would cause detrimental effects to the efficient exciton diffusion and dissociation and in turn enhance geminate recombination. The optimization of ZnO nanorod spacing will inevitably pose another problem on the polymer material. From Fig. 1-7-4, it appears that the polymer infiltration is mostly incomplete, often with no polymer filled in the nanorod spacing. If we further decrease the ZnO nanorod dimension, the polymer infiltration will be even more difficult and be limited to the polymer chain length which is on the same length scale as the opening of these dense nanorod arrays. To this end, our electrodeposition method attempts to mitigate the infiltration problem by employing a surface-initiated polymerization method that starts from the very surface of the nanorods which are exactly the region where we would like intimate contact between the two phases. Excellent coverage along high aspect ratio nanostructures has been reported in this thesis as well as other work involving electrodeposited PEDOT on GaAs nanopillar arrays (Fig. 1-7-5).[26]

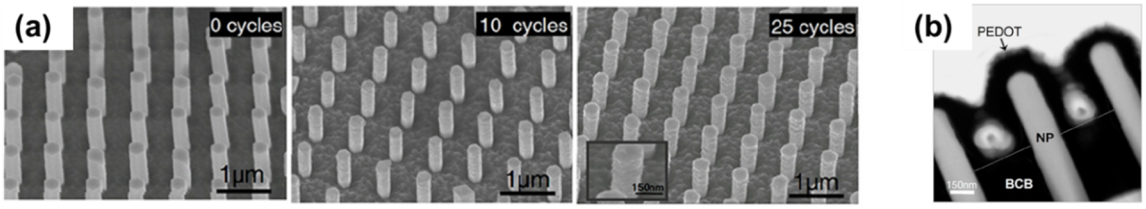

Fig. 1-7-5 (a) SEM images of electrodeposition applied to 190 nm diameter nanopillars, with increasing CV cycles (constant center-to-center pitch of 600 nm). (b) Cross sectional TEM image showing complete conformal polymer coverage around the GaAs nanopillars. Reprinted with permission from Ref (26). Copyright (2012) American Chemical Society.

Based on the above discussion, we chose ZnO nanorod/e-PT as our device architecture as illustrated in Fig. 1-7-6:

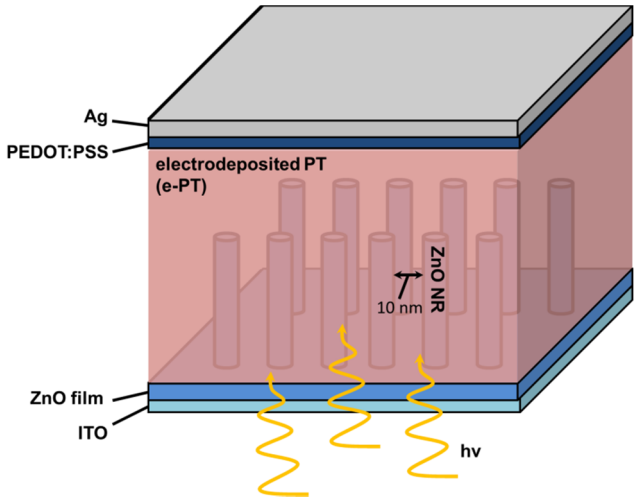

Fig. 1-7-6 Our electrodeposited PT/ZnO nanorod architecture

1.7.4 Interface

Multiple reports on various systems suggest that the interface between the organic and the inorganic phase play a critical role in charge separation and recombination processes.[40] Metal oxide surface treatment, doping and core-shell structures have shown the potential to increase the possibility of charge dissociation and reduce recombination events, resulting in more efficient devices. TiO_2 nanostructured devices show a better efficiency after $TiCl_4$ treatment.[46] This is supposed to fill Ti vacancies at the TiO_2 surface and repair surface defects. Self-assembled monolayers (SAMs) of alkanethiols attached to ZnO nanorods improved the packing order of P3HT close to the interface region. It results in reduced combination and improved J_{sc} and a more efficient OPV.[47] A monolayer of carboxylated polymer dyes is grafted to the metal oxide surface, possibly working as a crystallization seed layer and inducing favorable P3HT alignment along the nanostructure.[48]

Doping has also been shown to influence the charge transport properties and location of valence and conduction bands. Bilayer ZnO-P3HT hybrid solar cells showed an almost doubled V_{oc} upon doping the ZnO with Mg.[49]

ZnO-TiO_2 core-shell structures have been applied to P3HT based OPVs.[42] A five-fold J_{sc} increase is observed upon incorporation of a thin TiO_2 shell on ZnO nanorods. However, the working mechanism of this TiO_2 layer is not clear. It is hypothesized that because the V_{oc} and FF both increased markedly, the exciton dissociation across the organic-metal oxide interface is enhanced and/or it is acting as an energy barrier to reduce recombination events.

Current knowledge of the organic-inorganic interface dictates that the reduction of recombination losses will be an important prerequisite for these hybrid solar cells

employing an ordered BHJ architecture to progress forward with higher efficiency. Unhindered fast transport of charge carriers away from the interface is generally considered to be key to avoid recombination. For a system with unbalanced charge mobilities and slow transport of one type of carriers, the system may approach a space charge limited regime. In this case, the slower charge carrier is not sufficiently transported away from the interface and charge accumulation region leads to an increased probability of recombination. On the other hand, if mobilities are too high, the detrimental back-transfer of charges toward the interface may also be enhanced.[40] Although not well understood, core-shell structures with a recombination retardation shell layer seem to offer some insight for future endeavors in the field.

References:

1. D. Ginley, M. A. Green and R. Collins, *MRS Bull.*, 2008, **33**, 355-364.
2. *Equinox Enegy 2030: A Technological Roadmap for a Low Carbon Electrified Future*, Waterloo Institute for Sustainable Energy, Waterloo, ON, Canada, 2012.
3. *Technology Roadmap:Solar Photovoltaic Energy*, 2010.
4. *BP Statistical Review of World Energy*, 2013.
5. S. Mehta, *PV TECHNOLOGY AND COST OUTLOOK, 2013-2017*, 2013.
6. M. Liu, M. B. Johnston and H. J. Snaith, *Nature*, 2013, **501**, 395-398.
7. M. M. Lee, J. Teuscher, T. Mitasaka, T. N. Murakami and H. J. Snaith, *Science*, 2012, **338**, 643-647.
8. M. A. Green, K. Emery, Y. Hishikawa, W. Warta and E. D. Dunlop, *Prog. Photovolt: Res. Appl.*, 2013, **21**, 827-837.
9. M. Jorgensen, K. Norrman, S. A. Gevorgyan, T. Tromholt, B. Andreasen and F. C. Krebs, *Adv. Mater.*, 2012, **24**, 580-612.
10. S. A. Gevorgyan, M. V. Madsen, H. F. Dam, M. Jorgensen, C. J. Fell, K. F. Anderson, B. C. Duck, A. Mescheloff, E. A. Katz, A. Elschner, R. Roesch, H. Hoppe, M. Hermenau, M. Riede and F. C. Krebs, *Sol. Energy Mater. Sol. Cells*, 2013, **116**, 187-196.
11. G. Li, R. Zhu and Y. Yang, *Nature Photon.*, 2012, **6**, 153-161.
12. S. Gunes, H. Neugebauer and N. S. Sariciftci, *Chem. Rev.*, 2007, **107**, 1324-1338.
13. Y. Li, *Acc. Chem. Res.*, 2012, **45**, 723-733.
14. P. E. Shaw, A. Ruseckas and I. D. W. Samuel, *Adv. Mater.*, 2008, **20**.
15. J. Boucle, P. Ravirajan and J. Nelson, *J. Mater. Chem.*, 2007, **17**, 3141-3153.

16. Y.-J. Lee, M. T. Lloyd, D. C. Olson, R. K. Grubbs, P. Lu, R. J. Davis, J. A. Voigt and J. W. P. Hsu, *J. Phys. Chem. C*, 2009, **113**, 15778-15782.
17. G. P. Bartholomew and A. J. Heeger, *Adv. Funct. Mater.*, 2005, **15**, 677-682.
18. H. Wei, L. Scudiero and H. Eilers, *Appl. Surf. Sci.*, 2009, **255**, 8593-8597.
19. A. L. Briseno, T. W. Holcombe, A. I. Boukai, E. C. Garnett, S. W. Shelton, J. J. M. Frechet and P. Yang, *Nano Lett.* , 2010, **10**, 334-340.
20. J. Roncali, *Chem. Rev.*, 1992, **92**, 711-738.
21. C. J. Harris, W. J. Belcher and P. C. Dastoor, *Sol. Energy Mater. Sol. Cells*, 2007, **91**, 1127-1136.
22. W. Feng, A. S. Wan and E. Garfunkel, *J. Phys. Chem. C*, 2013, **117**, 9852-9863.
23. D. Xi, H. Zhang, S. Furst, B. Chen and Q. Pei, *J. Phys. Chem. C*, 2008, **112**, 19765-19769.
24. B. Sun, Y. Hao, F. Guo, Y. Cao, Y. Zhang, Y. Li and D. Xu, *J. Phys. Chem. C*, 2011, **116**, 1395-1400.
25. R. B. Laghumavarapu, G. Mariani, B. T. d. Villers, J. Shapiro, P. Senanayake, A. Lin, B. J. Schwartz and D. L. Huffaker, in *Photovoltaic Specialists Conference (PVSC), 2010 35th IEEE*, Honolulu, HI, 2010, pp. 000943-000945.
26. M. Giacomo, Y. Wang, P.-S. Wong, A. Lech, C.-H. Hung, J. Shapiro, S. Prikhodko, M. El-Kady, R. B. Kaner and D. L. Huffaker, *Nano Lett.* , 2012, **12**, 3581-3586.
27. R. J. Waltman and J. Bargon, *Can. J. Chem*, 1986, **64**, 76-95.
28. G. Mariani, R. B. Laghumavarapu, B. T. d. Villers, J. Shapiro, P. Senanayake, A. Lin, B. J. Schwartz and D. L. Huffaker, *Appl. Phys. Lett.*, 2010, **97**, 013107.
29. C. W. Tang, *Appl. Phys. Lett.*, 1986, **48**, 183-185.
30. G. Yu and A. J. Heeger, *J. Appl. Phys.*, 1995, **78**, 4510-4515.
31. J. J. M. Halls, C. A. Walsh, N. C. Greenham, E. A. Marseglia, R. H. Friend, S. C. Moratti and A. B. Holmes, *Nature*, 1995, **376**, 498-500.
32. M. Granstrom, K. Petritsch, A. C. Arias, A. Lux, M. R. Andersson and R. H. Friend, *Nature*, 1998, **395**, 257-260.
33. G. Yu, J. Gao, J. C. Hummelen, F. Wudl and A. J. Heeger, *Science*, 1995, **270**, 1789-1791.
34. Y. Liang and L. Yu, *Acc. Chem. Res.*, 2010, **43**, 1227-1236.
35. M. M. Wienk, J. M. Kroon, W. J. H. Verhees, J. Knol, J. C. Hummelen, P. A. v. Hal and R. A. J. Janssen, *Angew. Chemie, Int. Ed.*, 2003, **42**, 3371-3375.
36. J. You, L. Dou, K. Yoshimura, T. Kato, K. Ohya, T. Moriarty, K. Emery, C.-C. Chen, J. Gao, G. Li and Y. Yang, *Nature Communications*, 2013, **4**.
37. Z. M. Beiley and M. D. McGehee, *Energy Environ. Sci.* , 2012, **5**, 9173-9179.
38. M. C. Scharber, D. Muhlbacher, M. Koppe, P. Denk, C. Waldauf, A. J. Heeger and C. J. Brabec, *Adv. Mater.*, 2006, **18**, 789-794.
39. K. M. Coakley and M. D. McGehee, *Chem. Mater.*, 2004, **16**, 4533-4542.
40. J. Weickert, R. B. Dunbar, H. C. Hesse, W. Wiedemann and L. Schmidt-Mende, *Adv. Mater.*, 2011, **23**, 1810-1828.
41. Y.-J. Lee, M. T. Lloyd, D. C. Olson, R. K. Grubbs, P. Lu, R. J. Davis, J. A. Voigt and J. W. P. Hsu, *J. Phys. Chem. C*, 2009, **113**, 15778-15782.
42. L. E. Greene, M. Law, B. D. Yuhas and P. Yang, *J. Phys. Chem. C*, 2007, **111**, 18451-18456.

43. D. C. Olson, Y.-J. Lee, M. S. White, N. Kopidakis, S. E. Shaheen, D. S. Ginley, J. A. Voigt and J. W. P. Hsu, *J. Phys. Chem. B*, 2007, **111**, 16640-16645.
44. H. J. Snaith, G. L. Whiting, B. Sun, N. C. Greenham, W. T. S. Huck and R. H. Friend, *Nano. Lett.*, 2005, **5**, 1653-1657.
45. B. Conings, L. Baeten, H.-G. Boyen, J. D'Haen, M. K. V. Bael and J. V. Manca, *J. Phys. Chem. C*, 2012, **116**, 14237-14242.
46. P. M. Sommeling, B. C. O'Regan, R. R. Haswell, H. J. P. Smit, N. J. Bakker, J. J. T. Smits, J. M. Kroon and J. A. M. v. Oosmalen, *J. Phys. Chem. B*, 2006, **110**, 19191-19197.
47. M. T. Lloyd, R. P. Prasankumar, M. B. Sinclair, A. C. Mayer, D. C. Olson and J. W. P. Hsu, *J. Mater. Chem.*, 2009, **19**, 4609-4614.
48. C. J. Bhongale and M. Thelakkat, *Sol. Energy Mater. Sol. C.*, 2010, **94**, 817-822.
49. D. C. Olson, S. E. Shaheen, M. S. White, W. J. Mitchell, M. F. A. M. v. Hest, R. T. Collins and D. S. Ginley, *Adv. Funct. Mater.*, 2007, **17**, 264-269.

Chapter 2. Experimental Methods

2.1 XPS

X-ray photoelectron spectroscopy (XPS) is a surface-sensitive technique used to probe the chemical composition of the top few atomic layers of the sample. It is also commonly known as electron spectroscopy for chemical analysis (ESCA).[1] The interaction between the incident photons and the sample causes electrons to be emitted from the sample. The basic idea in XPS is to irradiate a sample with X-rays and then collect and energy analyze the electrons emitted from the sample. MgK_α or AlK_α X-rays with energies of 1253.6 eV or 1486.6 eV, respectively, are the most commonly used X-rays in XPS and were used in this study. The kinetic energy (KE) of the emitted electrons has the following relationship with the incident photon energy (hν):

$$KE = h\nu - BE - \varphi$$

where hν is the photon energy, BE is the binding energy of atomic orbital in which the electron is emitted from, and φ is the analyzer work function.

In addition to the aforementioned photoelectric process where electrons are emitted following direct interaction with the incoming photons, additional interactions may also take place in which electrons are emitted due to relaxation of electrons from higher binding energy orbitals into lower binding energy orbitals ionized by the incident photon. This is called the Auger process. This process occurs approximately 10^{-14} seconds after the photoelectric event, and results in richer, albeit sometimes more confusing, spectra.

In Fig. 2-1-1, both the photoelectric process and the Auger process are illustrated.

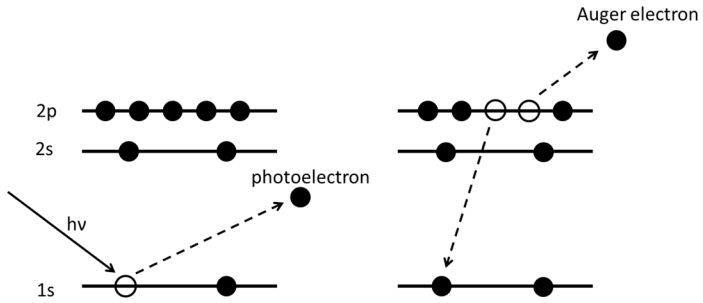

Fig. 2-1-1. Schematic of the photoelectric process (left) and the Auger process (right)

The Auger electron KE is the energy difference between the singly-charged initial ion and the doubly-charged final ion, therefore Auger KE should be independent of the incident X-ray energies. Such an independence can be utilized when trying to distinguish between various peaks in a photoelectron spectrum, as switching between two different X-ray energies (for example, MgK_{α} and AlK_{α}) should not cause a shift in Auger electron processes but will result in shifts in the photoelectron spectrum.

In summary, photoionization usually results in two kinds of emitted electrons, one kind is the photoelectron and the other kind is the Auger electron.

The cross section for interaction between the X-ray photons and a sample is far less than that between low energy electrons and the sample. Put another way, the mean free path for electron transport (1-10 nm, for low energy electrons, <2 keV) is far less than that of the incident photons (typical penetration depth on the order of 1-10 μm), usually on the order of nanometers. This means that although photoionization process

probably occurs within the first few micrometers of the sample, only those electrons within a few nanometers of the sample surface can escape the sample without energy loss. These electrons will form the peaks in the XPS spectra. The electrons that undergone energy loss processes, as well as other electronics scattered in secondary processes, will form the background.

The electrons leaving the sample are detected by an electron spectrometer according to their KE (Fig. 2-1-2). The analyzer is set up to only accept electrons of a certain energy range, and then the analyzer voltages are scanned to obtain the electron spectrum. A retardation voltage in the first lens of the analyzer, the "pass energy" between the inner and outer sectors of the analyzer, the various lens sizes and voltages, and other factors influence the energy and resolution of the spectrometer. Electrons are detected as discrete events impinging on a CCD (charge-coupled device) detector and translated into a digital signal.

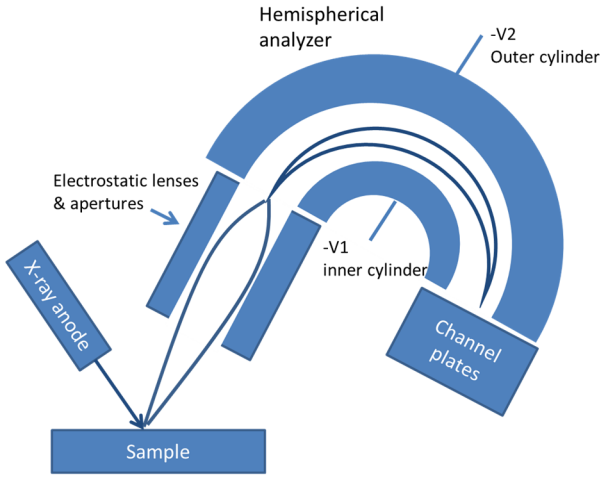

Fig. 2-1-2. Schematic of XPS experimental set-up

Energy referencing in this thesis was performed predominantly with the Au $4f_{7/2}$ peak at 84.0 eV and/or the adventitious carbon peak at 285.0 eV. The pass energy was adjusted so that the optimal balance between signal intensity and resolution could be attained. The number of scans must be sufficient enough to produce a good signal-to-noise ratio, which is proportional to the square root of the counting time. However, care must be taken considering each sample has its own radiation sensitivity and increasing the scan time may induce increased chemical changes within the sample.

In a typical XPS spectrum, there are several other types of lines beside the aforementioned photoelectron and Auger lines, to name a few: X-ray satellites, shake-up lines, multiplet splitting, spin-orbit coupling and energy loss lines. X-ray satellites are due to some lower intensity X-ray components at higher photon energy from the X-ray source. Usually these satellite intensities are less than 10% of the main photoelectron line. Shake-up lines are produced because in some cases the ion formed upon electron emission will remain in an excited state that is a few eVs above the ground state. Consequently, the electron KE will be reduced according to the difference between the ion ground state and the ion excited state. A shake-up peak will appear at a few eVs lower in KE and thus a few eVs higher in BE than the main peak. For example, the C 1s peak in unsaturated compounds may have a characteristic shake-up peak appearing a few eV higher BE than the main peak which originates from the $\pi \rightarrow \pi^*$ process.

Photoelectron peaks appear as pairs due to spin-orbital coupling for any photoelectron line that is not in an s-level. To understand this, we must look at ortibals in the atom. An orbital has orbital angular momentum, termed *l*, and *l* can take on values of 0, 1, 2, 3…. Within each given orbital angular momentum, there is an electronic spin,

called spin momentum and termed *s*. It can take on values of +1/2 or -1/2. The total electronic angular momentum (*j*) is a combination of orbital angular and spin momenta, therefore *j=l+s (all are vectors)*. When $l > 0$ (non-s-level orbitals), *j* can take on two values and represent two possible states of the final ion. The difference in these two states, ΔE_j, reflects the "parallel" and "anti-parallel" nature of the orbital angular momentum and spin momentum vectors of the remaining electron. The energy separation is expected to increase with atomic number Z for a given subshell or to decrease with increasing *l* values for a given principal quantum number *n* (for example, Ag 3p>3d). The intensity ratio of the doublet is given by the ratio of their respective degeneracies ($2j+1$). Thus for p subshell, $l=1$, j could be 1/2 or 3/2 and its respective degeneracies should be 2 or 4. Therefore, the relative intensity ratio of $p_{3/2}$:$p_{1/2}$ is 4:2 or 2:1. Similarly, the doublet relative intensity ratio for d and f are 3:2 and 4:3, respectively.[2]

Energy loss lines can be produced when the photoelectron has enhanced interaction with the other electrons in the surface region, causing loss of a specific amount of energy for the photoelectron.

For quantitative analysis, the integrated peak area and its corresponding sensitivity factor are used to determine the atomic ratio of a certain element in the compound.

There are two general methods to obtain depth information for elements in XPS: one is depth profiling by sputtering, the other is angle resolved measurements. Depth profiling by sputtering is performed by alternately analyzing and sputtering, and is therefore not limited to the electron escape depth. It can usually measure deeper into the

sample than angle resolved technique. However, sputtering can cause damage to the sample and rearrangement or removal of the atoms. In addition, different compounds have different sputtering rates and this causes preferential sputtering which complicates data interpretation. Angle resolved XPS is achieved by altering the angle between the sample plane and the entrance line to the analyzer. At smaller angles the signal from the surface is greatly enhanced comparing to that from the bulk and by varying the angles one can trace the evolution of peaks, thereby identifying whether the origin of the peaks are from the surface or from the bulk near the surface. This method is limited by the mean free path of the photoelectrons, resulting in a meaningful depth profile of only the top 5 nm.

2.2 UPS

UPS stands for ultra-violet photoelectron spectroscopy. Contrary to XPS which utilizes X-ray irradiation in the range of 1200-1500 eV, UPS makes use of ultraviolet radiation whose energy is typically less than 50 eV. Such low energies are only sufficient to eject electrons from the valence (or very shallow core) levels, therefore one usually uses UPS to study the density of states in the valence band. UPS can attain much higher resolution of ~0.1 eV compared to only ~0.5 eV in monochromated XPS systems. Better resolution can be obtained by working with highly energy resolved synchrotron sources and detectors.

He I and He II resonance lines are among the most used in UPS. These lines are resonance fluorescence produced when He is energetically excited and decays back to its

ground state. If the emitting species is a neutral excited He (in the gas phase), then it is called He I emission, while if the emitting species is a singly ionized He, then it is called He II. He I originates from a decay process of $^1P \rightarrow {}^1S$ (584 Å) and has an energy of 21.2 eV. He II results from a decay process of $^2P \rightarrow {}^2S$ (304 Å) and has an energy of 40.8 eV. Typical operating conditions to create He II radiation in a UV sources are ~4 kV and 75 mA, significantly higher than those for He I radiation (~2 kV and ~30 mA).[3] Usually higher voltages and currents and lower He gas pressure produce an increased intensity of He II irradiation. It should be noted that even at higher voltage and current conditions, He I radiation is still dominant relative to He II. This tends to obscure spectral features in the lower kinetic energy region (0-15 eV) due to the superposition of bands from ejection of outer electrons by He I and those from ejection of inner electrons by He II. Therefore He II radiation is mainly useful at higher kinetic energy side (KE > 15 eV).

He I is the dominant resonance line in UPS and therefore when trying to obtain information about the ionization potential we use He I resonance line. A typical He I spectra is depicted in Fig. 2-2-1.

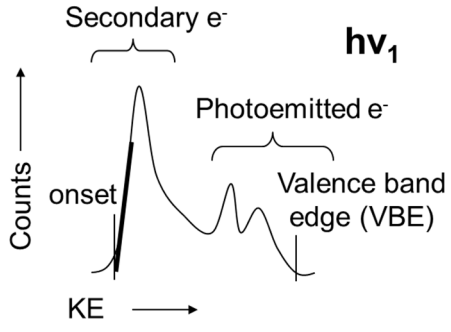

Fig. 2-2-1 Illustration of UPS He I (hv_1)

The onset of the secondary electrons represents the lowest kinetic energy electrons that can manage to escape from the sample surface and be detected (Fig. 2-2-1). We define the lowest energy electrons as the secondary electron cutoff (SEC), whose value is determined by drawing a straight line through the low energy tail of the spectra, extrapolated to the baseline). Electrons with kinetic energies below this value are not detected. Secondary electrons in this case are produced by inelastic collisions of the photoelectrons; they form a broad background with high intensity at lower kinetic energy (<10eV). Because they suffer from energy loss during the process of escaping the sample surface, they do not convey information about the primary photoelectron process. Therefore, this level should be the same regardless of initial photon energy (He I or He II), although the SEC does depend strongly on the work function of the sample.

The electrons from the HOMO level of the molecule (equivalent to the valence band edge, VBE, if using solid state electronic structure language) should exhibit the highest kinetic energy as they are furthest away from the nucleus and experience the least amount of attractive force from the nucleus. The ionization potential (IP, the energy to ionize a molecule) is photon energy minus the difference between the kinetic energy of the secondary electron cutoff and the electrons valence band edge:

$$IP = h\nu - |KE_{SEC} - KE_{VBE}|$$

To measure the secondary electron cutoff, one must apply a sufficiently negative bias to the sample to overcome the work function of the electron detector.

2.3 IPS

IPS stands for inverse photoelectron spectroscopy. While UPS probes the density of states in the valence band, IPS probes the empty states or the conduction band.[4] IPS is an important complementary technique to XPS/UPS, allowing one to study the electronic states above the Fermi level, for example unoccupied dangling bond states on semiconductors and the unoccupied orbitals (LUMO states) of organic materials. Inverse photoemission is more difficult to realize experimentally and harder to model computationally, thus there has been much less progress and far fewer publication using IPS than UPS or XPS. One reason for the experimental difficulty is that the yield is significantly lower than that in photoemission: typically 10^{-8} photons per incident electron, compared to 10^{-3} - 10^{-4} elastic photoelectrons per incident photon. If scanning for a longer period of time to obtain good statistics, possible beam damage must be taken into account. Low energy electrons pose a challenge to inverse photoemission because space charge sets limits to the attainable electron current. An efficient photon detector is required to capture the low intensities emitted from the sample due to the small electron current.

There are two different modes of inverse photoemission. One is realized by keeping the emitted photon energy ($h\nu$) fixed while varying the electron energy; this is called the isochromat mode. The other mode is accomplished by keeping the electron energy constant and measuring the distribution of the detected photon energy; this is called the spectrograph mode. For the isochromat mode, a Geiger-Müller tube filled with iodine gas with an entrance window of SrF_2 is often used as the photon detector. The combination of window and filling gas determines the detected photon energy, so for

iodine gas and SrF_2 window it selects photons of ~9.5 eV in energy. The spectrograph mode has advantages of acquiring different photon energies simultaneously, as well as better and constant focusing of the incident electron beam on the sample, as the energy is fixed. However, it is more complex to set up and more expensive to maintain than the isochromat mode. In our experiments, the home-made instrument with spectrograph mode was used for IPS studies.

2.4 RBS

Rutherford backscattering spectroscopy (RBS) uses high energy ions to probe the composition of a sample. In a typical experimental set up, relatively high energy particles (usually MeV $^4He^+$ ions) in the incident beam collide with target atoms in a sample and are scattered back into the detector for analysis of the scattered particle energies. During the collision process, energy is transferred from the incident particles to the stationary target atoms; the scattered particle experiences energy loss that is dependent on the atomic mass of the incident and target atoms and therefore provides important information about the nature of the target atoms. A schematic is illustrated in the following in Fig. 2-4-1:

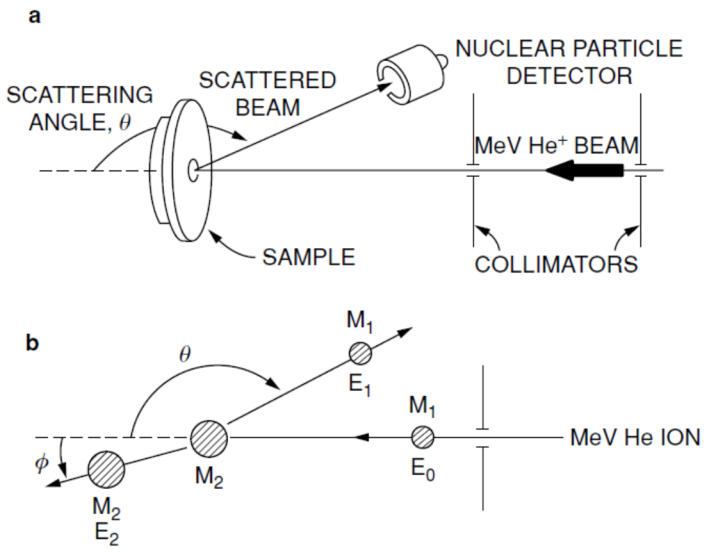

Fig. 2-4-1 Working mechanism and collision model for RBS. Reprinted from Ref (5), with kind permission from Springer Science+Business Media B.V.

As a surface analytical technique, RBS is conceptually the most simple and quantitatively the most accurate in terms of coverage (atoms/cm^2). It is an ideal thin film technique to obtain stoichiometry and depth-dependent composition information. However, as the kinematics of the collision and the scattering cross-section is not influenced by chemical bonding, RBS cannot be used to analyze chemical bonding (unlike XPS). The lateral spatial resolution is ~1 mm for the RBS in Nanophysics Laboratory (NPL) at Rutgers University.

Channeling of ions takes place when the incident beam is meticulously aligned with the symmetry direction of a single crystal. The incident beam will then be steered (channeled) through the tunnels formed by the strings of atoms. Channeled ions fail to approach the target atoms spatially, therefore there is minimal interaction between them

to induce Rutherford backscattering. As a result, the scattering from that single crystalline substrate is markedly reduced by a factor of ~100. This will decrease the background of the substrate and in turn increase the instrumental sensitivity to impurities on the surface. The ability to successfully channel through the substrate with a relatively large decrease in scattering intensity, also serves as experimental proof that the substrate is of single crystalline nature. In practice, the substrate can be maneuvered by a goniometer such that the crystalline planes can be found and channeling can be performed.

2.5 SEM

SEM stands for scanning electron microscopy. In a conventional SEM system, a tungsten wire bent to a sharp angle (hairpin) is used as the electron source. The electrons emitted from the source are focused onto the sample and the secondary electrons are collected off to the side of the sample by a secondary electron detector. At 35 keV acceleration voltage, the resolution is normally 50-400 Å. The resolution degrades rapidly to 500-1000 Å at lower acceleration voltage such as 5 keV. Hence, conventional SEMs are most often operated at a voltage of 10-35 keV due to limited resolution at lower voltage.[6] High-resolution SEM takes advantage of a field emission gun (FEG) electron source and that is why it is also called field emission SEM (FESEM). The model for FESEM used in this thesis is Carl Zeiss SIGMA Series FESEM. The most common FEG is a dual cold-cathode system that has an electron source made of a single-crystalline tungsten tip etched to a radius of curvature of ~1000 Å. The FEG source offers high brightness, small spot size and low energy spread. With this FEG source, FESEM

can achieve resolutions of 15 Å at 30 keV and 75 Å at 1 keV in ideal situations. Lower electron beam energies have the benefit of lower charging and possibly lower beam damage to the sample, especially for organic samples that are sensitive to electron bombardment. When high-energy electrons bombard a material, a range of particles can be emitted, including characteristic X-rays, Bremsstrahlung radiation (broad energy electromagnetic radiation produced by the deceleration of a charged particle when deflected by another charged particle), elastically scattered primary electrons ("backscattered" electrons), and inelastically scattered "secondary" electrons produced by the interaction of the primary or backscattered electrons with the valence-shell electrons of the sample. The backscattered electrons are those that have an energy > 50 eV up to the energy of the primary beam electrons. The secondary electrons are normally considered to have an energy < 50 eV. It is the secondary electrons that are normally detected in SEM, although some SEMs also have an ability to analyze either the backscattered electrons or the x-rays that are emitted when the electrons hit the sample (EDX).

2.6 AFM

Atomic force microscopy (AFM) is a standard analytical tool to probe surface topography. A probe tip at the end of a cantilever arm interacts with the surface and the resulting force deflects a laser beam that is reflected off the cantilever. The tip interacts with a surface in a repulsive manner as described by Hooke's Law (Fig. 2-6-1) when in a contact mode. The interaction between the tip and the surface deflects the cantilever and

the extent of such a deflection is measured by the probe tip displacement. As the probe tip is scanned across a sample surface, the laser beam reflects off the cantilever arm and a three-dimensional image of the surface is constructed. In the constant-force mode of imaging a surface, one uses a piezoelectric drive with a feedback loop to keep the cantilever deflection constant. Tapping mode is another commonly employed mode, as it eliminates the lateral forces between the tip and the sample and overcomes some of the limitations of both contact and noncontact AFM. In tapping mode, the cantilever resonates at its resonant frequency of 100-400 kHz. The probe tip contacts the surface only for a fraction of the resonant period so as to reduce the influence of the lateral forces (such as water contamination) on the probe tip. The feedback loop adjusts itself such that the amplitude of the cantilever resonates at a constant value and an image can be formed from this amplitude signal.

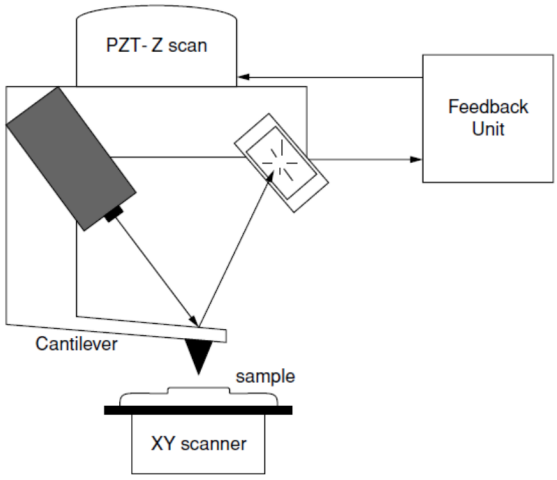

Fig. 2-6-1 AFM working mechanism. Reprinted from Ref (5), with kind permission from Springer Science+Business Media B.V.

2.7 Electrochemistry

Electrochemical methods are powerful both for the synthesis of the new materials as well as the analysis of existing materials. In the dissertation, a majority of the synthetic work was performed using electrodeposition (synonymous with electropolymerization). In particular, we used the electro-oxidation of monomers to form oligomers and eventually polymers on the surface of the electrode. Electrochemical analysis was carried out to investigate the electronic properties of the materials after the electrodeposition.

Electrochemical experiments were carried out with a Princeton Applied Research VersaSTAT potentiostat. A three-electrode system was used. The working electrode can be any conductive substrate. In our case, we have used Au, Si, Ge, ITO, ZnO films and ZnO nanorods. The counter electrode was a Pt gauze. The reference electrode was a Ag/Ag^+ non-aqueous reference electrode consisting of 0.01 M $AgNO_3$ and 0.1 M Bu_4NPF_6 in acetonitrile (ACN). All potentials reported in this paper were referenced to this Ag/Ag^+ reference electrode. Before electropolymerization, the solutions were deoxygenated by bubbling nitrogen through the solution for 10 minutes; a nitrogen overpressure was maintained throughout the experiment. The polymer can be synthesized by a variety of electrochemical methods, such as: potentiodynamic (scanning the potential), potentiostatic (keeping the potential constant), and galvanostatic (keeping the current constant). After electrodeposition, the sample was then removed from the solution and rinsed with copious amounts of solvent. For neutral polymers suitable for photovoltaic applications, the sample was reduced by a standby potential of -1 V (vs. the Ag/Ag^+ reference electrode) in a monomer-free electrolyte solution until the current was stable. The sample was again removed from solution and rinsed thoroughly. For

electrochemical analysis, the as-deposited sample was placed in a monomer-free electrolyte solution and cyclic voltammetry was carried out to obtain its redox waves.

A schematic of our electrochemical set up is as follows (Fig. 2-7-1). Photographs before and after electrodeposition of the apparatus are shown in Fig. 2-7-2.

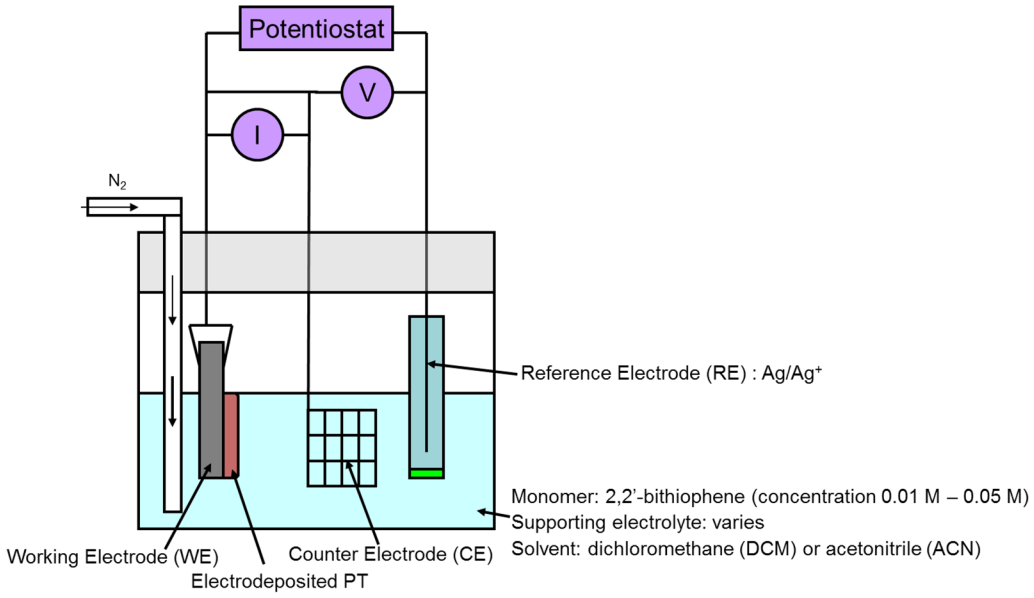

Fig. 2-7-1 Electrodeposition experimental set up

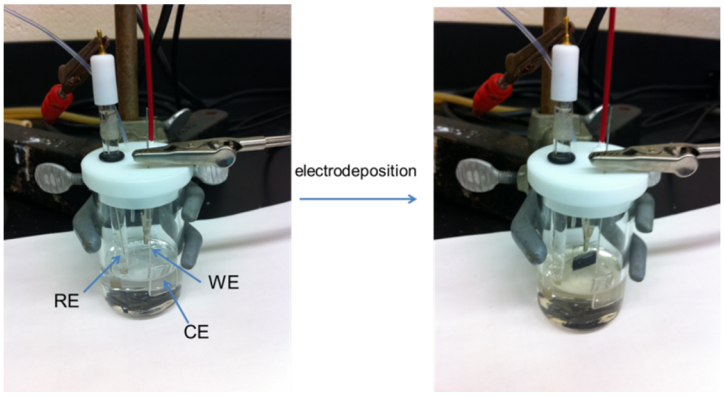

Fig. 2-7-2. Electrodeposition process in photographs.

A Ag/Ag^+ (Ag wire in a $AgNO_3$ solution) was used as a non-aqueous reference electrode and its potential must be calibrated carefully to ensure that its potential is constant over time. We use the ferrocene/ferrocenium couple to calibrate it. We made a 3 mM ferrocene solution in acetonitrile and use a Pt wire as the working electrode and Pt gauze as the counter electrode. The cyclic voltammetry of the ferrocene couple will yield an oxidation and reduction peak. The midpoint of the two peaks will give the ferrocene couple potential measured against our reference electrode. We have consistently obtained 0.1 V as its mid-point potential value, therefore our reference electrode is of constant potential throughout our measurements.

2.8 Other Characterization Techniques

UV-visible absorption spectra were recorded on a Shimadzu UV-3600 UV-Vis-NIR spectrophotometer. PL spectra were obtained on a Horiba Jobin Yvon Fluorolog-3 spectrofluorometer. The morphology of e-PT films was visualized by helium ion microscope (HIM, Zeiss Orion Plus, 30 kV acceleration voltage, 0.2-0.4 pA beam current). Single attenuated total reflectance infrared (FTIR-ATR) spectra were performed on a Thermo Electron Corporation Nicolet 6700 FT-IR (ZnSe Crystal, number of spectra averaged 1024, resolution 4 cm^{-1}).

References:

1. M. Liu, M. B. Johnston and H. J. Snaith, *Nature*, 2013, **501**, 395-398.
2. D. Briggs and M. P. Seah, eds., *Practical Surface Analysis* 2nd edn., John Wiley & Sons, West Sussex, 1990.

3. J. W. Rabalais, *Principles of Ultraviolet Photoelectron Spectroscopy*, John Wileys & Sons, 1977.
4. F. J. Himpsel and T. Fauster, *J. Vac. Sci. Technol. A*, 1984, **2**, 815-821.
5. T. L. Alford, L. C. Feldman and J. W. Mayer, *Fundamentals of Nanoscale Film Analysis*, Springer, New York, NY, 2007.
6. D. L. Vezie, E. L. Thomas and W. W. Adams, *Polymer*, 1995, **36**, 1761-1779.

Chapter 3. Electropolymerization of Polythiophene on Au, ITO, Ge, Si

3.1 Electrodeposition on Au

Au is a noble metal and that does not undergo oxidation in our electrochemical experiments. In addition, it has excellent electrical conductivity and is therefore an ideal substrate for model electropolymerization studies. The growth of PT on Au is evidenced by the progressive redox waves in the cyclic voltammograms (Fig. 3-1-1). In the 1st CV sweep, the current on the reverse scan is larger than that on the forward scan. The formation of this "loop" is characteristic of a nucleation process and only appears during the 1st CV sweep.[1] The oxidation peak of the polymer appears at around 1.1 V during the 2nd CV sweep (Fig. 3-1-1, arrow),[2] suggesting that electrodeposition has occurred during the 1st CV sweep. The current increase in subsequent CV cycles makes the oxidation peaks less well-defined.[3] The reduction peaks, however, are not affected and show continuous expansion vertically on each successive cycle. The increasing reduction peak current indicates the progress of the electropolymerization. The electrochromic switching of the polymer film, which appears black at higher potentials and reddish at lower potentials, is a direct consequence of the polymer oxidation and reduction processes.[4]

Fig. 3-1-2 shows RBS spectra carried out on three polythiophene films PT1-3 grown by CV in 2, 4 and 8 cycles, respectively. PT Film thickness and roughness is estimated by converting the areal density of the PT layer to thickness using the bulk density value (1.5 g/cm^3) from the literature.[5, 6] Analysis of the RBS data shows that both the thickness and roughness of the PT film increase over cycle numbers (see Table 3-1-1).

This observation has been well documented in the literature.[7, 8] The inset in Fig. 3-1-2 shows that the film thickness (by RBS) increases linearly with cycle number in the given range, with an approximate 50 nm film growth per cycle.

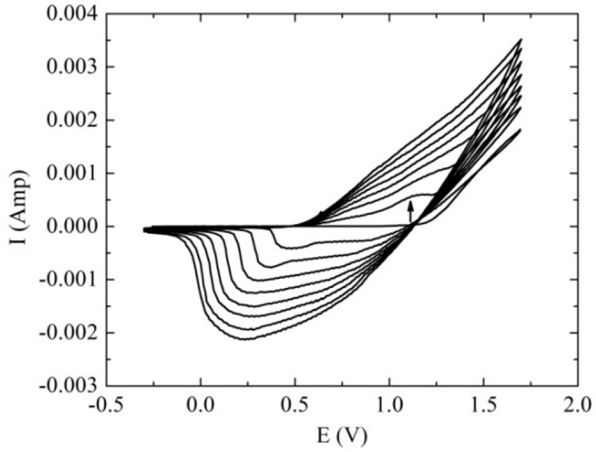

Fig. 3-1-1. CV of PT film growth on Au with 8 consecutive CV sweeps from -0.3 V to 1.7 V. The scan rate is 100 mV/s. The arrow points to the first oxidation peak of the polymer.

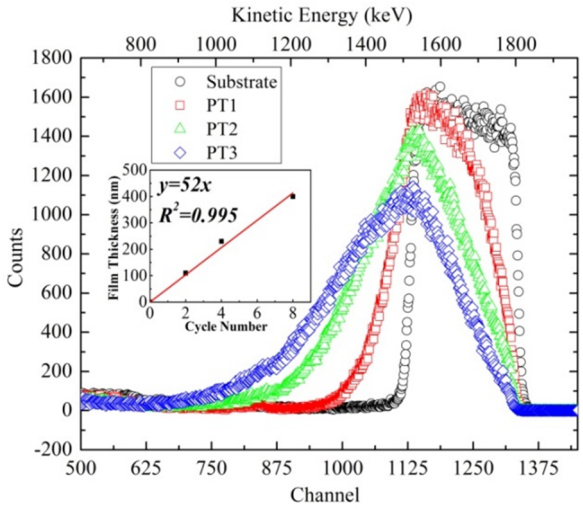

Fig. 3-1-2. RBS spectra of the Au peak of the substrate and samples PT1-3. Inset: film thickness by RBS vs. cycle number.

Table 3-1-1. Film information by RBS and charge integration

sample	thickness (nm)		roughness (nm)
	by RBS	by charge	
PT1	110	100	7×10
PT2	230	260	1.7×10^2
PT3	400	450	2.3×10^2

Film thicknesses can also be estimated from the total charge dissipated during the electropolymerization. The polymerization of each bithiophene monomer unit involves the removal of about 2.25 electrons.[9] Therefore, the resulting film thickness *d* can be estimated by the total charge in the monomer oxidation process, *Q*, using the following equation:

$$\left[\frac{Q}{2.25eN_0}\right]M_w = \rho S d$$

where *e* is the electron charge, N_o is Avogadro's constant, M_w is the molecular weight of bithiophene (166 g/mol), *S* is the area of the film, and ρ is the density of the film and assumed to be 1.5 g/cm^3 according to literature values.[5, 6] *Q* can be calculated by integrating the area under the *I-t* curve where the monomer oxidation occurs. Film thicknesses calculated from the total charge passing through the electrochemical cell are summarized in Table 3-1-1.

Fig. 3-1-3 compares the film thickness obtained by the two methods at 2, 4, and 8 cycles. The film thicknesses calculated from the total charge yielded similar or slightly higher values than those by RBS. This is because the total charge consists of two

constituents: the charge for monomer oxidation which contributes to the film growth and the charge for polymer oxidation which does not induce polymer chain growth.[4] The charge for polymer oxidation is dependent on the amount of polymer on the electrode. When the polymerization has just started, there is a small amount of polymer on the electrode and its influence to the total charge is minimal (Fig. 3-1-3). As the cycle numbers increase, there is a larger amount of polymer electrodeposited onto the electrode and it requires more charge dedicated to the oxidization of the polymer layer. Therefore, the thickness calculated from the total charge appears to be bigger than that by RBS. In addition, the thickness difference of the two methods becomes more pronounce as the electropolymerization progresses, because a higher ratio of the total charge is devoted to polymer oxidation. Fig. 3-1-3 also shows that the film thickness data deduced from the total charge becomes unreliable at longer electropolymerization time. In the electrochemical deposition community, it is a common and widely accepted practice to estimate film thickness with the total charge. However, it is important to be cautious when doing so because the deviation from the actual film thickness increases with time based on our observation.

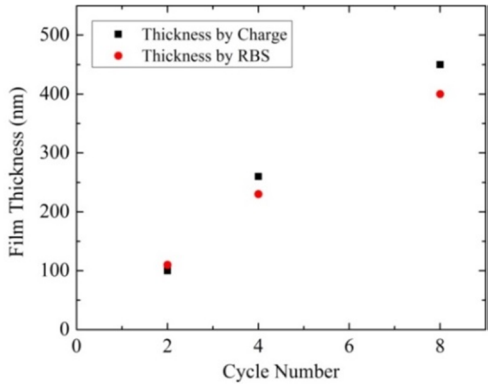

Fig. 3-1-3. Comparison of film thicknesses obtained by two methods: RBS and electrochemical experiments. The samples are PT films on Au.

3.2 Electrodeposition on ITO

In addition to electrochemical and RBS methods, optical absorption can be used to probe the thickness of the film. This is because the absorption is proportional to film thickness according to Beer's law, assuming the substrate is not optically opaque. The substrate ITO meets this optical requirement and is thus used as the substrate for electropolymerized PT. We prepared 3 sets and a total number of 9 PT films that were electrodeposited onto ITO substrates (surface area normalized to 1 cm^2) by CV in 2, 4 and 8 cycles, respectively. Combining the total charge, the UV-vis absorption and the film thickness from RBS, Fig. 3-2-1 shows the plots of the three sets of data against cycle number, which encompass electrochemical, optical and ion scattering techniques.

Fig. 3-2-1a depicts the relationship between the total charge and the cycle number. As mentioned previously, the total charge is consisted of two parts: monomer oxidation and polymer oxidation. The charge needed for polymer oxidation increases as there is more polymer accumulating onto the electrode. This causes the total charge to increase faster than the cycle number as the polymerization proceeds, which is why the slope of the total charge curve is increasing.

Fig. 3-2-1b represents the plot of the intensity at absorption maximum vs. the cycle number. The absorption is proportional to the cycle number. The best fit of the three sets of samples (R^2=0.999) yielded a slope of 0.29 a.u./cycle and an intercept of 4.0 a.u. The ITO coated borosilicate glass substrate has background absorption of ~3.9 a.u at 500 nm. The intercept of the plot matches the absorption intensity of the substrate (ITO/glass), further validating the correlation between the absorption and the film thickness.

The film thickness from RBS analysis is plotted against cycle number in Fig. 3-2-1c. The best fit straight line (R^2=0.997) provides a slope of 35 nm/cycle and an intercept of 2 nm. Comparing to PT grown on Au, the growth rate of PT on ITO is slower, due to the higher resistance of ITO. At the beginning of the experiment, there is no film deposited onto the electrode and therefore the film thickness should be 0. The intercept from the best fit is 2 nm, which is very close to 0. This is indicative of the validity of the linear relationship between the actual film thickness and the cycle number.

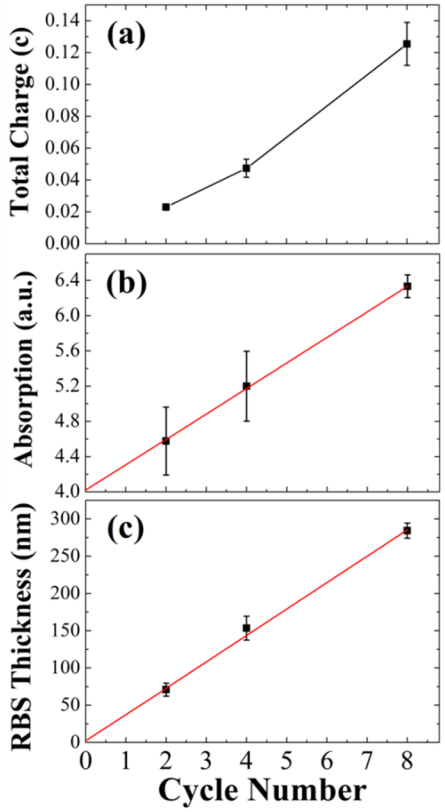

Fig. 3-2-1. Plot of (a) Total Charge, (b) UV-vis absorption and (c) Thickness (RBS), against cycle number. The samples are PT films on ITO.

In summary, we utilized the total charge, optical absorption and RBS to monitor the thickness of the film grown on the ITO electrodes. In particular, optical absorption

and thickness measured by RBS show good linearity with the cycle number. The total charge, due to its inherent limitation, does not exhibit the same degree of linearity. Nonetheless, it provides an estimate of the film thickness by simply integrating the *I-t* curve without the use of other instrumentation. A combination of the three techniques allows for cross-examination of the electrochemical deposition of PT and proves to be more informative than any one of the techniques.

3.3 Valence Band Structure and Ionization Potential: UPS

Valence level UPS He II spectra (e.g. Fig. 3-3-1) shows characteristic peaks indicative of PT.[10] The features at 13.2 and 10.6 eV are attributed to σ states of C 2p. The feature at 7.7 eV is predominantly from σ states of C 2p, with some contribution from the π (S 3p+C 2p).[10] Our measurements are in relatively good agreement with literature values.[11] In addition, the σ features are well-resolved in our UPS He II spectra when compared to literature reports on PT or P3HT using UPS He I radiation.[11, 12]

The region from 0 to 5 eV corresponds to the π states of PT. Literature theoretical calculations of the density of valence states on PT[11] allow the following peak assignment for the π states: (1) The intense peak at 3.6 eV originates from π (S 3p+C 2p). (2) The peak at 1.7 eV represents the π state of contribution from C 2p and partial contribution from S 3p. (3) The feature at around 0.1-0.7 eV is due to strongly delocalized HOMO state of C 2p. The signal-to-noise ratio for this feature is relatively low comparing to the other two π states. However, the clear change in slope between this feature and the higher binding energy feature π (S 3p+C 2p) validates the existence of this weak HOMO state of C 2p.

The insets in Fig. 3-3-1 show the values of E_{onset} and E_{HOMO} for the 5 polymer samples prepared by cyclic voltammetry (CV, voltage scan) or potentiostatic method (PM, voltage hold). IP can thus be calculated from the corresponding E_{onset} and E_{HOMO}:

$$IP=21.2\ eV - |E_{onset} - E_{HOMO}|$$

Table 3-3-1 provides a summary of the UPS data (E_{onset}, E_{HOMO} and IP), film roughness and electrode material. IP values of 4.7-5.2 eV were obtained, which correspond with the reported values of 4.6 to 5.2 eV in the literature.[13-18] Researchers have used different preparation methods to produce PT films, which has been attributed to the variation of IP values in the literature.

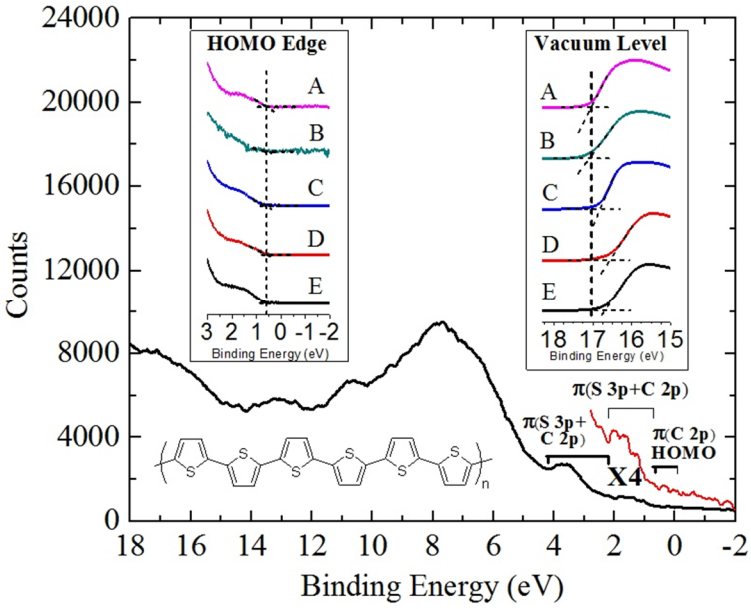

Fig. 3-3-1. UPS He II spectrum of PT. The left inset shows the HOMO edge (He I). The right inset shows the onset of the vacuum level (He I). The spectra in the insets are normalized to enable direct comparison. Films are prepared as follows: **A**: PM (1.7 V, 0.5 s) on Au; **B**: CV (-0.3 V - 1.8 V, 5 cycles) on Si; **C**: CV (-0.3 V - 1.7 V, 8 cycles) on Au;

D: PM (1.9 V, 72 s) on Si; **E**: CV (1 scan 1.7 V - -0.3 V and 2 sweeps -0.3 V - 1.9 V) on Si. CV scan rate is 0.1 V/s.

Table 3-3-1. Summary of UPS and film information

sample	E_{onset} (eV)	E_{HOMO} (eV)	IP (eV)
A	17	0.6	4.8
B	17.1	0.6	4.7
C	16.8	0.7	5.1
D	16.6	0.6	5.2
E	16.7	0.6	5.1

The polymer film was studied in a monomer-free solution by CV. Fig. 3-3-2 shows the cyclic voltammogram of a PT film in an electrolyte solution free of monomers. The oxidation peak is around 1.0 V and the reduction peaks are around 0.4 V and 0.8 V. The two reduction peaks represent the two stable states of partially undoped PT. In the process of undoping, anions are expelled from the polymer matrix and this induces conformational changes in the polymer chains.[2]

The onset of the oxidation peak can be converted to the IP of the polymer as follows based on certain extrathermodynamic assumptions:[19]

$$IP = 4.6\ eV + eE_{ox}$$

where E_{ox} is the onset of the oxidation potential. In Fig. 3-3-2, the oxidation onset is around 0.5 V. According to this equation, the IP calculated from the electrochemical measurement is therefore approximately 5.1 eV. This is within the range of IP values

obtained from UPS. This suggests that CV is a simple and moderately accurate method to estimate the ionization potential of the polymer and serves as an alternative technique to UPS.

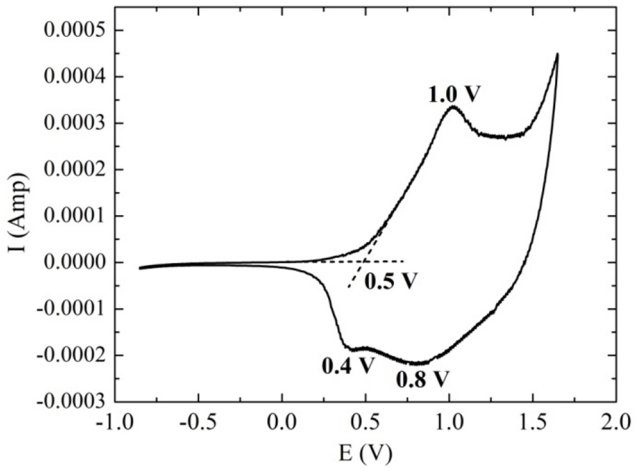

Fig. 3-3-2. CV of PT in a 0.1 M Bu_4NPF_6 DCM solution. The scan rate is 50 mV/s. The oxidation onset is determined by the intersection of the two tangent (dashed) lines.

Note that these are as-grown films and not subject to electrochemical reduction to obtain neutral state polymers. A visually obvious self-dedoping (reducing) phenomenon occurs after these films are removed from their original growth solution and placed in ambient conditions, as the film undergoes electrochromic color changes from blue (doped state) to red (neutral state). This self-dedoping is especially immediate for thinner films presumably due to the ease of anions buried close to the surface to escape the polymer matrix. The self-dedoping manifests itself as a color change from the original blue/black color to red color. For thicker films, the effect is less severe because the anions are buried deeper inside the bulk of the film and cannot readily escape; therefore the film remains effectively doped and blue/black in color. In summary, the anions present in thinner films

are more likely to escape the polymer while those in thicker films will remain highly doped after exposure to ambient conditions. This dopant level difference may be one of the reasons the IP values for thinner and thicker films are different in this case.

3.4 Dopant Effect on Ionization Potential

To examine the effect of dopants on the polymer film IP values, we produced two e-PT samples electrodeposited with a fixed charge of 25 mC onto the Au substrate. One sample was used as grown, while the other sample was reduced to completely remove the anions present in the film. In Fig. 3-4-1 samples 3 and 5 represents the fully undoped (reduced) and the doped sample, respectively. The doped sample has an IP of 5.1 eV, compared to a lower IP of 4.9 eV for the undoped sample. This increase in IP, as well as the exact amount of increase (0.2 eV), correspond with literature values for doped and undoped polymer samples.[20]

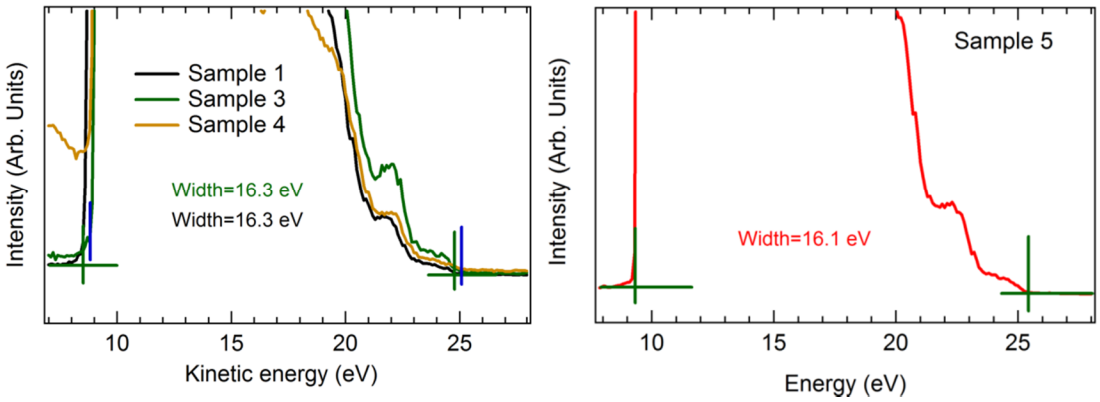

Fig. 3-4-1. UPS He I spectra with secondary electron cutoff (SEC) and valence band edge (VBE) extrapolated. The width represents the kinetic energy difference of SEC and VBE. IP is calculated by the following equation: IP = 21.2 eV - $|E_{VBE} - E_{SEC}|$.

3.5 Morphology Effect on Ionization Potential

Morphology effects must also be considered as a possible factor influencing the IP values of the polymer films, as it is known that the thicker films also exhibit higher roughness.[21] Using AFM, we examined the surface morphology of polymer films polymerized with an increasing amount of charge [2.6 mC (sample 1), 3.7 mC (sample 2), 25 mC (sample 3) and 125 mC (sample 4)]. Sample 5 is the polymerized film with the same charge as sample 3 for 25 mC, but left heavily doped (without an undoping procedure). Fig. 3-5-1 shows the morphology and the line profile of these samples, along with the Au substrate. Sample 4 is polymerized with the largest amount of charge and is considerably rougher than the other films polymerized with lower charges. However, there is no significant difference in the IP values between the sample 1, 3 and 4 (Fig. 3-4-1). Therefore, this is indicative that the morphology does not have a noticeable effect on the IP values.

Another conclusion that can be drawn from this AFM study is that there is no significant difference in surface morphology between the undoped and doped samples (sample 3 and 5). This indicates that the undoping process, realized by applying a negative potential of -1 V to remove the anions from the polymer matrix, has a very limited influence on the resultant polymer morphology, possibly due to the high robustness or rigidity of the system.

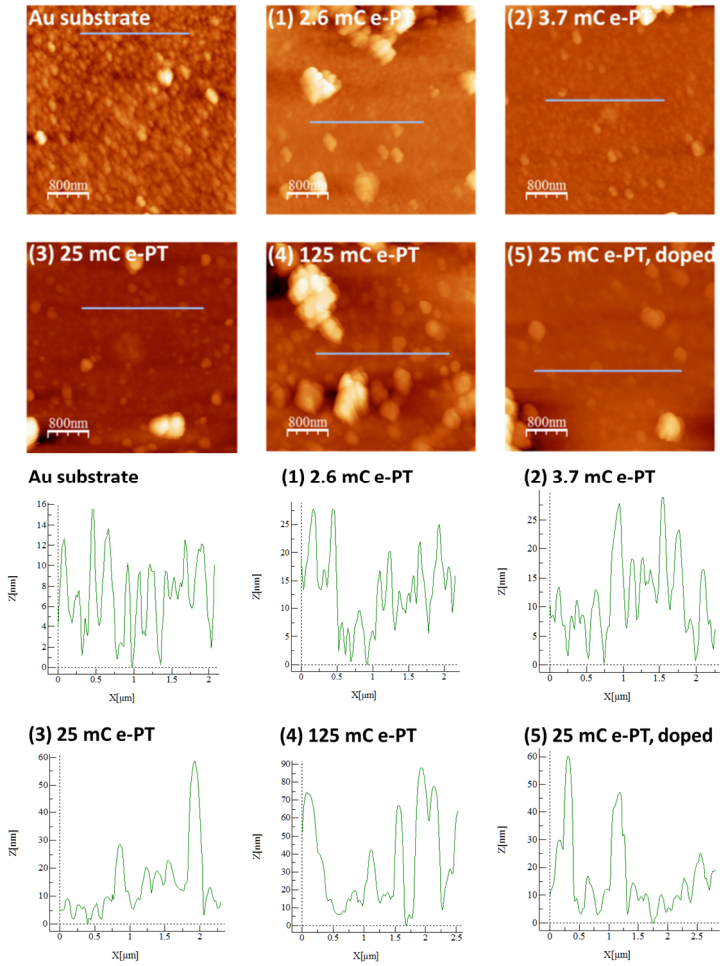

Fig. 3-5-1. AFM and line profile of the corresponding e-PT films on Au.

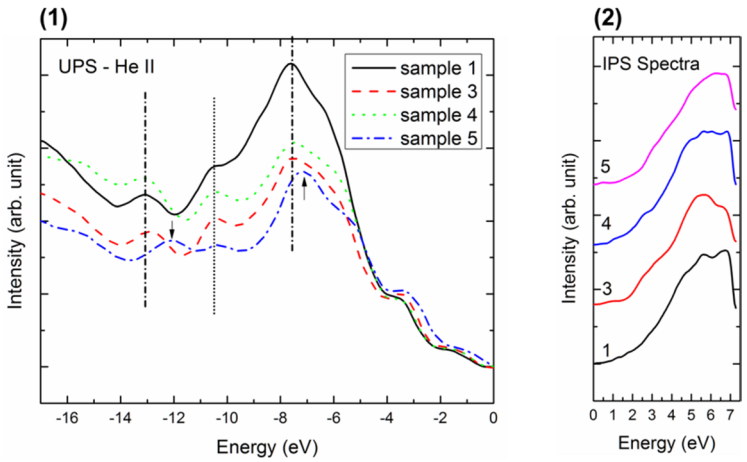

Fig. 3-5-2. (1) UPS-He II spectra and (2) IPS spectra of sample 1, 3, 4 and 5. Arrows are meant to point out the different peak positions for the doped sample (sample 5).

UPS He II spectra show typical fingerprint spectra for polythiophenes (Fig. 3-5-2), with notable differences in peak positions for sample 5 from the rest of the samples. The arrows point to two σ states where the sample 5 spectrum differs from the other samples. This feature can be used as another indicator to differentiate the doped and undoped samples in addition to careful examination of the IP values from the UPS He I spectra. Additionally, sample 5 shows a rigid shift in the π region, consistent with literature reports.[20]

Inverse photoemission (IPS) experiments were also carried out (Fig. 3-5-2). Due to the much lower resolution of the method itself compared to UPS, as well as the inherent lack of features for polythiophene in the simulated IPS spectrum, we are unable to extract useful information with IPS. There also appears to be beam damage in IPS which involves the appearance of additional peaks upon electron bombardment during the measurements, therefore the measurement has to be accomplished quickly which further limits the resolution of the spectra. Although IPS utilizes electrons of ~20 eV in energy, this small energy is sufficient to induce structural or chemical changes in the polymer. For example, as is evidenced by XPS measurements immediately after IPS, the ClO_4^- anions present in sample 5 have been partially reduced to ClO_3^-.

3.6 Probing the coverage of the PT films on Au substrate: RBS

RBS was carried out to measure the surface coverage of the PT films on Au. RBS measurements were carried out on PT films polymerized with 2, 25 and 125 mC charge, respectively and shown in Fig. 3-6-1. Fig. 3-6-1a shows a full RBS spectrum of the Au substrate, and we can clearly observe the Au peak and the Ti (used as an adhesive layer

between the mica and the Au) peak above the mica peaks (fitted with a target composition of Mg, Al, Si, K and O). Fig. 3-6-1b shows the Au peaks and comparing to earlier RBS data on PT1-3, these Au RBS spectra are considerably different, in particular the back edge of the Au peak. This is because the older samples (e.g. the one noted above) PT1-PT3, synthesized using potentiodynamic method, have a much larger roughness than these samples synthesized by potentiostatic method. The potentiostatic method we used employs a potential that is as low as possible to initiate polymerization, whilst the potentiodynamic produces samples experienced higher potentials at some time of the potential cycling and therefore experienced a higher growth rate and may lead to increasing disordere in the surface morphology. As the polymer thickness increases, the Au front edge shifts to lower energy. The lack of a shoulder, significant broadening, or additional peak on the front edge, indicates that within the RBS detection limit there are no pinholes and relatively conformal coverage of Au by the polymer. Fig. 3-6-1c shows that as the polymer thickness increases with charge, from 2 to 125 mC, the sulfur intensity correspondingly increases. Fig. 3-6-1d shows that there is no visible ion beam effect or radiation damage to the 25 mC polymer sample upon successive 3 μC beam exposure, as the spectra appear nearly identical to each other.

The measured RBS areal density values for the three samples were tabulated in Table 3-6-1, along with the charge used for electrodeposition for comparison purposes. As one can see, as the charge increased from 5 to 25 mC, the polymer thickness increased from 130 to 520 nm, however, the increase is not linear. The increase is even less proportional as the charge increased from 25 mC to 125 mC. In this latter case, the

polymer thickness only increased from 520 nm to 955 nm, indicating that the polymer growth increasingly suffers from loss processes during the electrodeposition.

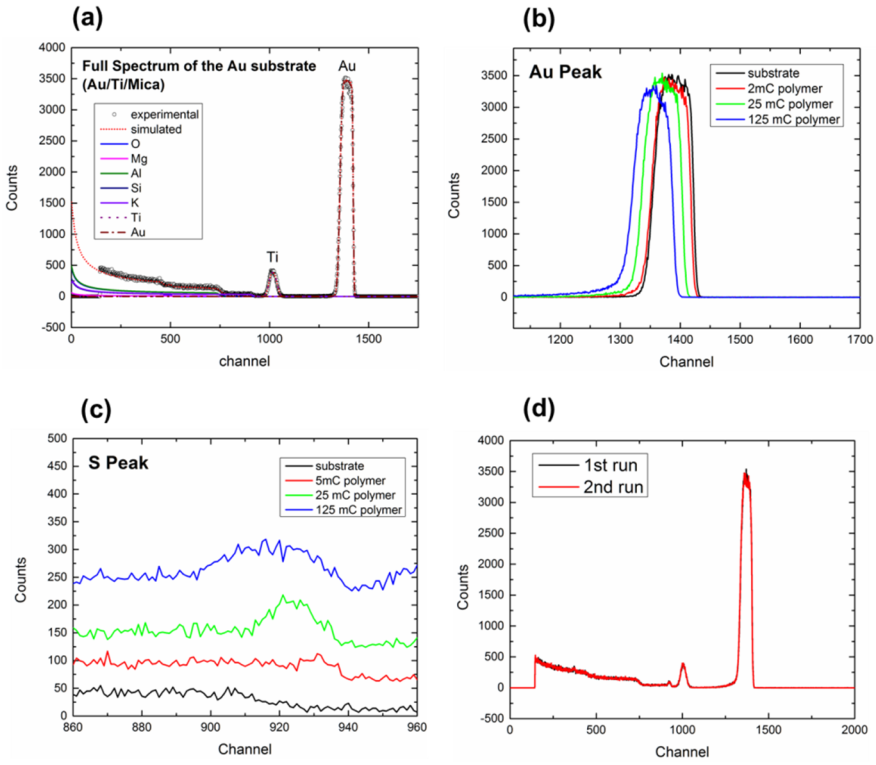

Fig. 3-6-1. RBS spectra: (a) Full Spectrum of Au/Ti/Mica; (b) Au peak spectra; (c) S peak spectra; (d) 25 mC polymer successive RBS measurements (1st and 2nd run)

Table 3-6-1. RBS Data Summary

Sample number	Electrochemical Charge (mC)	Areal Density (10^{15} atoms/cm^2)
5mC polymer	5	130
25 mC polymer	25	520
125 mC polymer	125	955

3.7 Chemical Composition of e-PT on Au: XPS

In order to gain a better insight into the doping process, how much dopant is incorporated into the polymer matrix, and how successful the polymer reduction process (or undoping process) is, we carried XPS (Fig. 3-7-1 and Fig. 3-7-2) to determine the chemical composition of polymer films by varying the thickness and varying the doping level (doped vs. undoped).

Survey Scan: survey scan shows a huge secondary electron background for the thinnest polymer sample deposited on Au. This observation is reproducible and may be due to charging.

C 1s: extra shoulder representing some oxidized C species for a doped sample.

S 2p: again, a shoulder is observed at the higher energy tail of S 2p and represents polaronic and multipolaronic state contributions, which are properly fitted in Fig. 3-7-2.[22]

O 1s: There is some O in the neutral polymer samples, particularly for thicker sample (125 mC sample). Doped samples shows a distinct O1s peak from ClO_4^-.

Cl 2p: Only the doped sample shows a significant Cl 2p doublet (Fig. 3-7-2), with the Cl $2p_{3/2}$ peak centering at 207.1 eV. This represents the binding energy of ClO_4^-.[23]

N 1s: some trapped solvent in the thickest sample (125 mC sample). In other samples, the nitrogen content cannot be observed within XPS limitation (1% atomically).

Au 4f: Only for the thinnest sample (3 mC sample) are we able to observe the underlying Au 4f, of which we reference the Au $4f_{7/2}$ to 84.0 eV. For the other samples, we cannot observe the Au substrate because the polymer layer has become thicker. In this circumstance, the neutral thiophene S $2p_{3/2}$ binding energy at 163.9 eV was used for energy referencing.

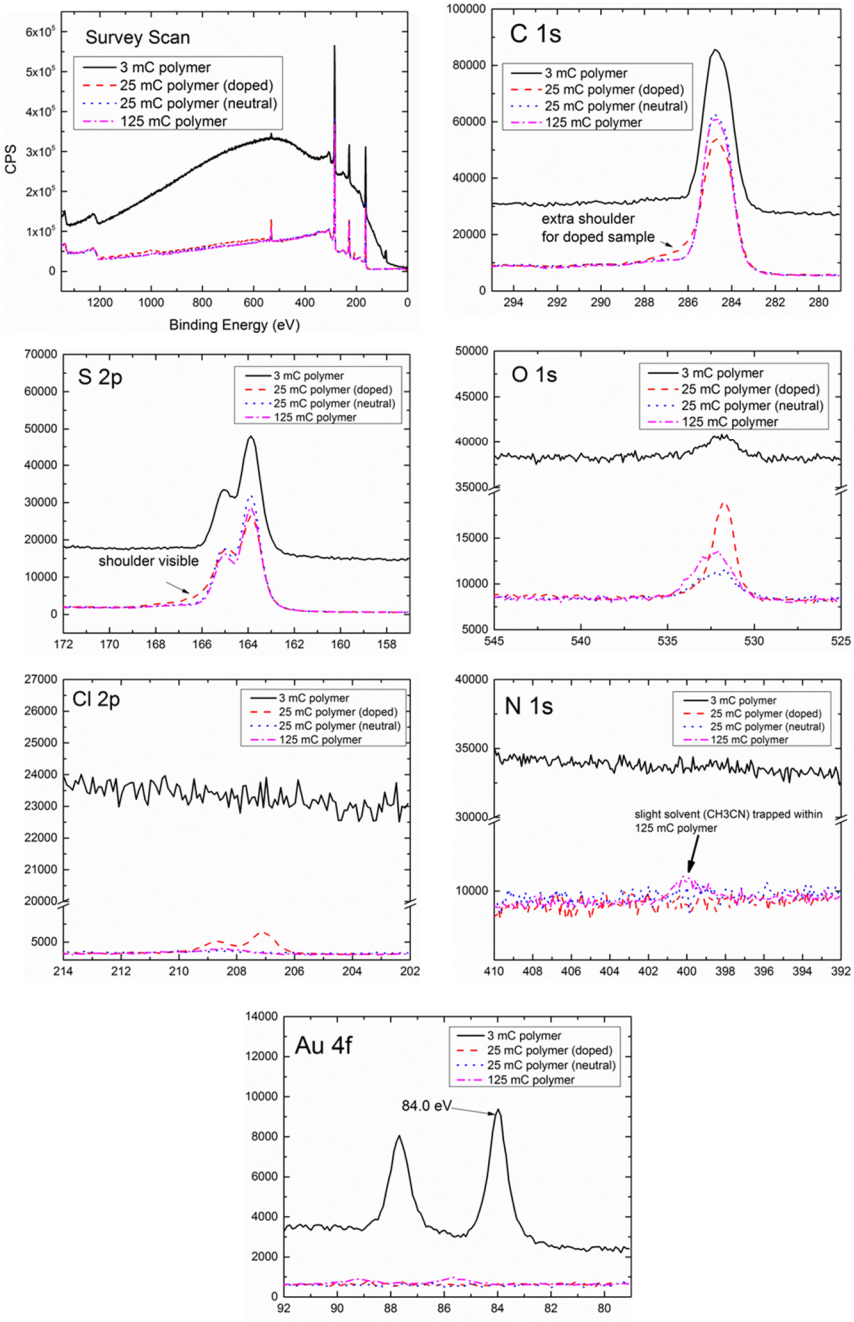

Fig. 3-7-1. XPS spectra of neutral polymer films polymerized with 3, 25 and 125 mC charge, with a doped polymer film polymerized with 25 mC charge. From left to right and top to bottom: survey spectra, C 1s, S 2p, O 1s, Cl 2p, N 1s and Au 4f.

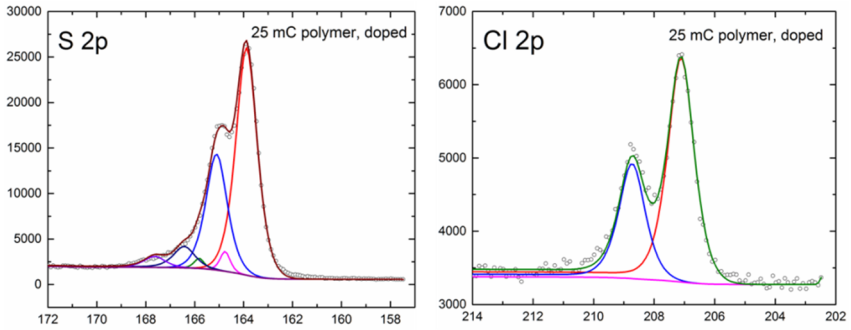

Fig. 3-7-2. Fitting of S 2p and Cl 2p of the doped 25 mC polymer sample

3.8 Optical Properties and Energy Diagram

Normalized UV-vis absorption and PL spectra of the polymer film are shown in Fig. 3-8-1. The UV-vis absorption is typical of a conjugated polymer which consists of an absorption band with several absorption maxima at around 524, 541 and 566 nm. These absorption peaks are due to the $\pi \rightarrow \pi^*$ transitions of PT. The optical bandgap (E_g) can be evaluated from an extrapolation to the x-axis from the linear portion of the plot α^2 vs. $h\nu$, where α, h, and ν are the absorption coefficient, Plank's constant, and the frequency of light, respectively. For PT grown on ITO in 2, 4, and 8 cycles of CV, E_g is found to be a direct band gap transition of approximately 2.0 eV, in excellent agreement with the literature.[24]

Complementary to UV-vis absorption, PL arises from interchain and intrachain excitons undergoing relaxation.[25] The PL band was observed at the absorption-edge energy (Fig. 9). The PL spectrum was taken at an excitation wavelength of 488 nm and the emission maxima are at 619 nm and 665 nm, which is in agreement with the literature.[26]

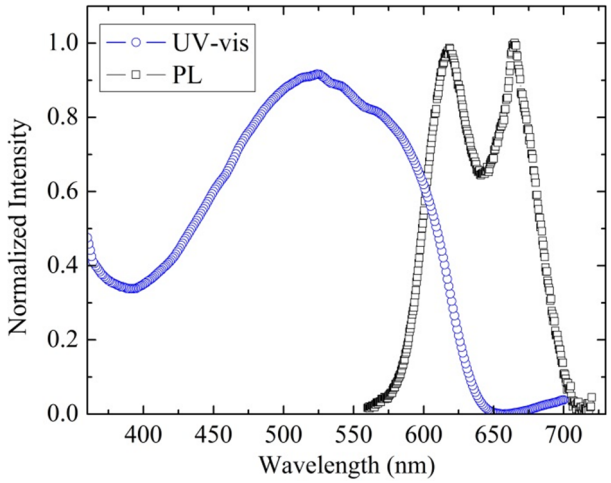

Fig. 3-8-1. Normalized UV-vis absorption and PL spectra of PT.

The energy diagram of the polymer based on E_g and IP is depicted in Fig. 3-8-2. The energy of LUMO to the vacuum level is a good approximation of electron affinity (EA). Accurate HOMO-LUMO level of the polymer will be crucial in understanding the fundamental energy transfer in solar cells and other applications.

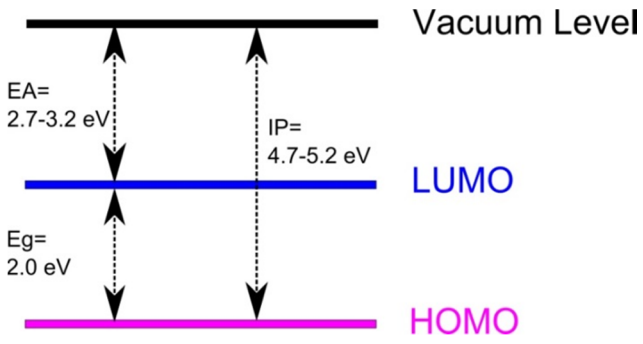

Fig. 3-8-2. Energy diagram of electrogenerated PT.

References:

1. J. Heinze, A. Rasche, M. Pagels and B. Geschke, *J. Phys. Chem. B*, 2007, **111**, 989-997.
2. B. L. Funt and S. V. Lowen, *Synth. Met.*, 1985, **11**, 129-137.
3. T. Tuken, B. Yazici and M. Erbil, *Appl. Surf. Sci.*, 2005, **239**, 398-409.
4. J. Roncali, *Chem. Rev.*, 1992, **92**, 711-738.
5. F. Garnier, G. Tourillon, J. Y. Barraud and H. Dexpert, *J. Mater. Sci.*, 1985, **20**, 2687-2694.
6. T.-C. Chuang, J. Kaufman, A. Heeger and F. Wudl, *Phys. Rev. B*, 1984, **30**, 702-710.
7. R. Schrebler, P. Grez, P. Cury, C. Veas, M. Merino, H. Gomez, R. Cordova and M. A. del Valle, *J. Electroanal. Chem.*, 1997, **430**, 77-90.
8. M. Innocenti, F. Loglio, L. Pigani, R. Seeber, F. Terzi and R. Udisti, *Electrochimica Acta*, 2005, **50**, 1497-1503.
9. R. J. Waltman and J. Bargon, *Can. J. Chem*, 1986, **64**, 76-95.
10. C. Wu, J. Nilsson, O. Inganas, W. Salaneck, J. E. Osterholm and J. Bredas, *Synth. Met.*, 1987, **21**, 197-202.
11. X. T. Hao, T. Hosokai, N. Mitsuo, S. Kera, K. K. Okudaira, K. Mase and N. Ueno, *J. Phys. Chem. B*, 2007, **111**, 10365-10372.
12. L. Scudiero, H. Wei and H. Eilers, *ACS Appl. Mater. & Interfaces*, 2009, **1**, 2721-2728.
13. H. Fujimoto, U. Nagashima, H. Inokuchi, K. Seki, Y. Cao, H. Nakahara, J. Nakayama, M. Hoshino and K. Fukuda, *J. Chem. Phys.*, 1990, **92**, 4077-4092.
14. A. Cascio, J. Lyon, M. Beerbom, R. Schlaf, Y. Zhu and S. Jenekhe, *Appl. Phys. Lett.*, 2006, **88**, 062104.
15. B. Hamadani, H. Ding, Y. Gao and D. Natelson, *Phys. Rev. B*, 2005, **72**, 235302.
16. W. Osikowicz, M. de Jong, S. Braun, C. Tengstedt, M. Fahlman and W. Salaneck, *Appl. Phys. Lett.*, 2006, **88**, 193504.
17. M. Al-Ibrahim, H.-K. Roth, U. Zhokhavets, G. Gobsch and S. Sensfuss, *Sol. Energy Mater. Sol. Cells*, 2005, **85**, 13-20.
18. J. Bredas, R. Silbey, D. Boudreaux and R. Chance, *J. Am. Chem. Soc.*, 1983, **105**, 6555-6559.
19. J. O. M. Bockris and S. U. M. Khan, *Surface Electrochemistry - A Molecular Level Approach*, Plenum Press, New York, 1983.
20. P. Ruankham, S. Yoshikawa and T. Sagawa, *Mater. Chem. Phys.* , 2013, **141**, 278-282.
21. J. R. Reynolds, S.-G. Hsu and H. J. Arnott, *J. Polym. Sci. Polym. Phys.*, 1989, **27**, 2081-2103.
22. J. H. Kaufman, C. K. Baker, A. I. Nazzal, M. Flickner, O. R. Melroy and A. Kapitulnik, *Phys. Rev. Lett.*, 1986, **56**, 1932-1935.
23. R. Younesi, M. Hahlin, F. Bjoerefors, P. Johansson and K. Edstoem, *Chem. Mater.*, 2013, **25**, 77-84.
24. M. Kobayashi, J. Chen, T.-C. Chung, F. Moraes, A. J. Heeger and F. Wudl, *Synth. Met.*, 1984, **9**, 77-86.
25. K. Kaneto, F. Uesugi and K. Yoshino, *J. Phys. Soc. Jpn.*, 1987, **56**, 3703-3709.

26. T. Sato, M. Fujistsuka, H. Segawa, T. Shimidzu and S. Tanaka, *Synth. Met.*, 1998, **95**, 107-112.

Chapter 4. Electropolymerization of Polythiophene on ZnO

4.1 Synthesis of ZnO Substrates: ZnO Film and Nanorod Growth

There are many means to deposit ZnO films: sputtering, evaporation, pulsed laser deposition, spray pyrolysis, molecular beam epitaxy (MBE), metal organic chemical vapor deposition (MOCVD) and sol-gel methods. Sputtering inevitably causes plasma damage to the resulting film and vacuum-based methods require expensive and low throughput equipment. The sol-gel method, on the other hand, is an inexpensive method that provides adequate film quality control and compatibility for high volume production. A variety of parameters control the deposition process: chemical species in the solution, solution concentration, spin coating conditions, and thermal annealing conditions. The sol-gel method is cost effective comparing to sputtering and MOCVD, and is therefore our choice for deposition of ZnO films.

ZnO nanorods (NRs) can be grown from a seed layer, such as the aforementioned ZnO film. ZnO NR growth is generally achieved by these three methods: vapor-liquid-solid (VLS) deposition, chemical vapor deposition (CVD) or hydrothermal synthesis.[1] In all fabrication methods, the anisotropic growth of the ZnO crystal is due to a faster rate of growth along the c-axis, often resulting in structures with the morphology of a rod or wire with the [0001] direction perpendicular to the substrate.

It is well known that vapor phase methods such as VLS deposition can produce high-quality aligned ZnO NR arrays, but this type of reaction generally requires high growth temperatures between 800-900°C and a catalyst.[2] Aligned growth of ZnO NR without a catalyst has also been achieved using low-temperature CVD and metal organic

chemical vapor deposition (MOCVD). [3] However, as we have mentioned before CVD and MOCVD methods require expensive instrumental set-up. Hydrothermal growth has enjoyed considerable attention in the ZnO community due to its simple inexpensive set up, mild growth temperature and potential for large scale production.

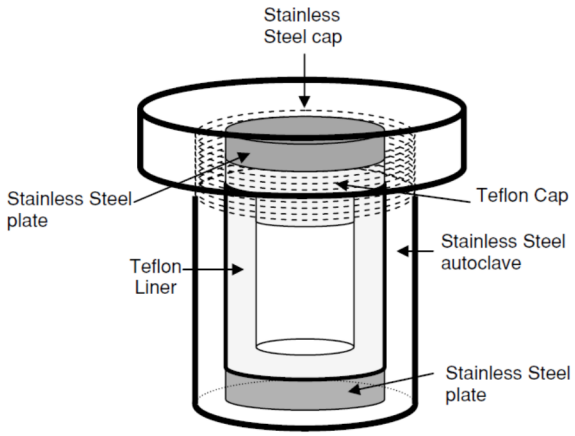

Fig. 4-1-1. Hydrothermal Teflon-lined stainless steel reactor. Reprinted from Ref (1), with kind permission from Springer Science+Business Media B.V.

In a typical hydrothermal reaction, a precursor providing the element of interest and a reagent capable of regulating the crystal growth are dissolved in aqueous solution in a certain ratio. This mixture is placed in a reactor to allow the reaction to proceed at elevated temperature and pressures.

Fig. 4-1-1 shows an example of the reactor employed in our experiments. The lid of the Teflon cup is meticulously machined to ensure that there will be significant tension applied to seal the cup when the metal cap is tightened. The separate Teflon liner fits into the autoclave without leaving any gap. The reason that Teflon is used as the reactor materials is due to its chemical inertness. The reaction time can range from a few hours to a few days. Standard hydrothermal experiments are conducted under isothermal and

isobar conditions without agitation. The major advantage of this approach is that most of the inorganic materials can be made soluble in water at elevated temperatures and pressures. When an ITO substrate coated with ZnO film is introduced into an autoclave, beside the homogeneous nucleation which produces insoluble inorganic materials precipitating out of the solution, there is additional heterogeneous nucleation that makes the reaction more complex. It is proposed that controlling the interfacial tension is critical in controlling the shape and orientation of crystallites growing on a substrate from aqueous precursors.[4] In aqueous solution, crystal nucleation will occur when the solution reaches supersaturation. Initial nucleation can occur either in solution (homogeneous) or on the surfaces of the solid phase (heterogeneous), depending on the relative energetics of the system. If the interaction between the growing nucleus and the substrate surface represents a lower net energy, heterogeneous nucleation will be favored over homogeneous nucleation. The adhesion energy between the crystallite and the substrate (due to interfacial bond formation minus interfacial strain) can be dominant contributors to the net free energy for heterogeneous nucleation.[5] These and additional factors determine the density of nuclei and the tendency for two versus three dimensional growth.

The method to grow nanorods on ZnO films is as follows: ZnO films were made by a sol-gel method. A 750 mM zinc acetate solution in 2-methoxyethanol of equal molar ratio of zinc acetate and ethanolamine, was spin-coated at 2000 rpm for 30 seconds. Then the sol-gel film was annealed on a hot plate in air at 200 or 300 °C for 10 min. Afterwards, for the synthesis of ZnO nanorods, the sol-gel prepared ZnO film was used as a seed layer. ZnO nanorods were grown from the ZnO planar substrate by a hydrothermal method in a sealed reactor. The substrate was suspended and facing down

in 12 mL solution of equal molar ratio of 6.25, 12.5, 25 or 50 mM zinc nitrate hexahydrate and hexamethylenetetramine at various temperature (70, 92.5 or 115 °C) for various times (60-180 minutes). The nanorod substrate was subsequently rinsed with DI water and dried in air.

ZnO nanorods grown on a ZnO seed layer are epitaxial, showing preferential growth in a direction normal to the surface as evidenced by the very large intensity of the (002) diffraction peak in XRD (Fig. 4-1-2). ZnO nanorods exhibit a polar Zn-terminated (0001) or O-terminated $(000\bar{1})$ tip and non-polar mixed-terminated $(10\bar{1}0)$ sidewalls. The polar Zn-(0001) or O-$(000\bar{1})$ tip have higher energy than the non-polar sidewalls, and thus either form complex surface structures or undergo reconstruction to reduce their electrostatic energy.[6] ZnO growth occurs favorably on the higher energy (0001) and $(000\bar{1})$ surfaces to reduce the overall free energy of the system, forming one-dimensional ZnO nanostructures.

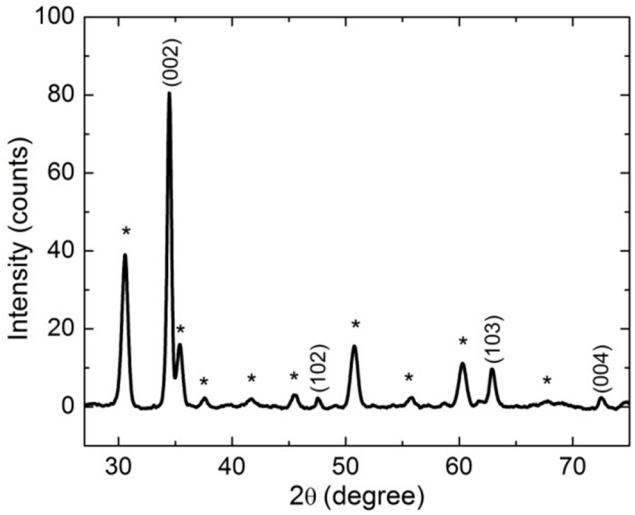

Fig. 4-1-2. XRD graph of ZnO nanorods. The peaks with an asterisk are diffraction peaks from the ITO substrate.

4.1.1 Processing Parameter Control of ZnO Nanorods Growth Morphology

The Effect of ZnO Film Annealing Temperature.

Different processing conditions of the ZnO film will inevitably affect the resulting ZnO nanorod morphology as the film serves as the seed layer for nucleation and growth of the nanorods (Fig. 4-1-3). The 200 °C annealed ZnO film yielded a more tapered nanorod tip and a longer nanorod of ~1300 nm, compared to that of 600 nm tall nanorods for a ZnO film annealed at 300 °C, most likely due to the larger and better oriented starting ZnO crystallites.

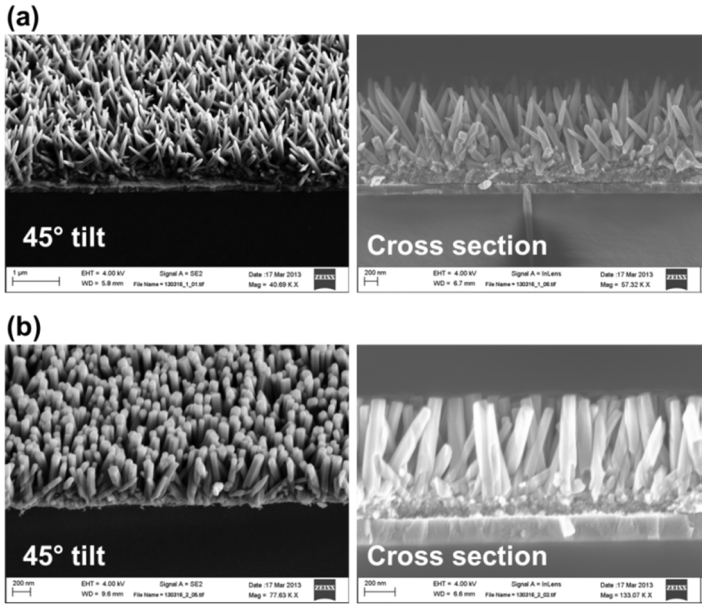

Fig. 4-1-3. SEM images (45° tilt angle and cross sectional) of ZnO nanorods grown from (a) ZnO films annealed at 200 °C, (b) ZnO films annealed at 300 °C.

The Effect of Growth Time.

For a given concentration of solution (25 mM), the growth time was allowed to increase from 60 minutes, to 90 minutes and to 180 minutes (Fig. 4-1-4). At 60 minutes,

the nanorods seem to relatively short in height (~50 nm). As the growth time increased from 60 minutes to 90 minutes to 180 minutes, the nanorods height grew rapidly from 50 nm, to 500 nm, to 875 nm. This indicates that we can control the nanorod height by varying the growth time. Our interpretation of this is that there is an initial time associated with temperature equilibration, than addition time associated with nucleation of the nanorods, after which they grow at a rapid pace. Eventually, the growth rate slows as the reactant concentration is continuously lowered (due to deposition).

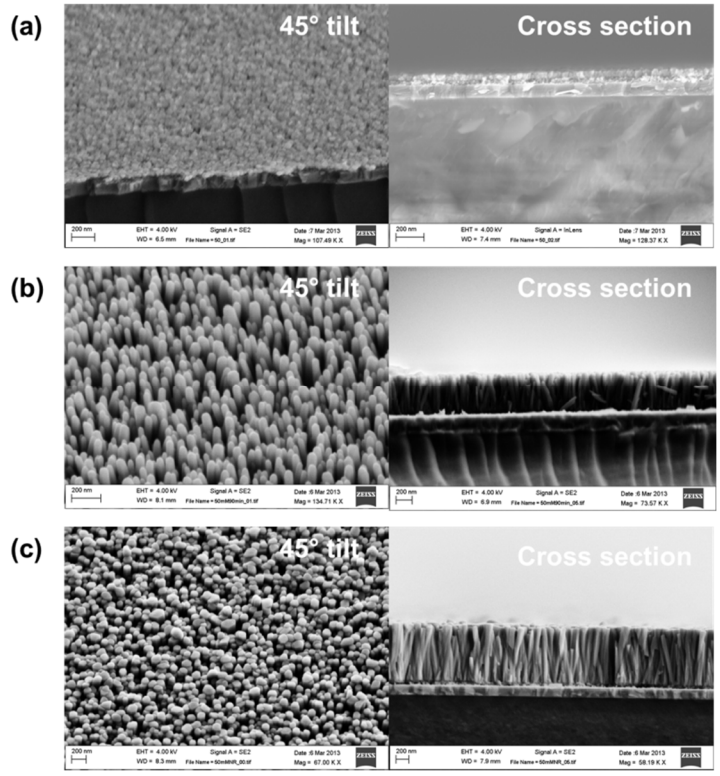

Fig. 4-1-4. SEM images (45° tilt angle and cross sectional) of ZnO nanorods hydrothermally grown at 92.5 °C for (a) 60, (b) 90 and (c) 120 minutes.

The Effect of Solution Concentration.

For a relatively long growth time of 180 minutes, varying the concentration of the solutions also affects the growth tremendously (Fig. 4-1-5). At lower concentrations at 6.25 and 12.5 mM, the height of the majority of the nanorods are similar at 500 and 560 nm respectively, though there is more evident nanorod height variation for the lowest concentration sample at 6.25 mM. As expected, the height of the nanorods is higher (875 nm) at a higher concentration of 25 mM.

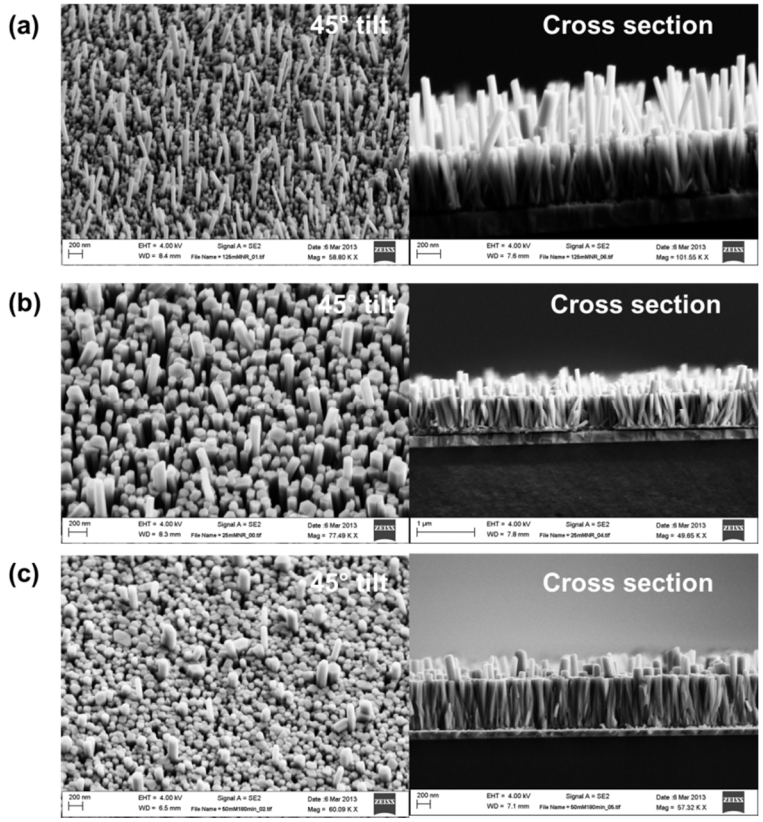

Fig. 4-1-5. SEM images (45° tilt angle and cross sectional) of ZnO nanorods hydrothermally grown at 92.5 °C for 180 minutes at an equal molar concentration of the two reactants at (a) 6.25 mM, (b) 12.5 mM and (c) 25 mM.

At a shorter (relative) growth time of 60 minutes, there appears to be a threshold concentration that needs to overcome in order for the nanorods to grow on the substrate (Fig. 4-1-6). For 6.25 and 12.5 mM, there are barely any nanorods visible. For 25 mM, we see some nanorods growing to a very short height (50 nm). For 50 mM, we can clearly see nanorods growing from the substrate at a substantially higher height (240 nm). This indicates that a higher concentration of reactants will yield a faster nucleating (and growth) nanorod environment.

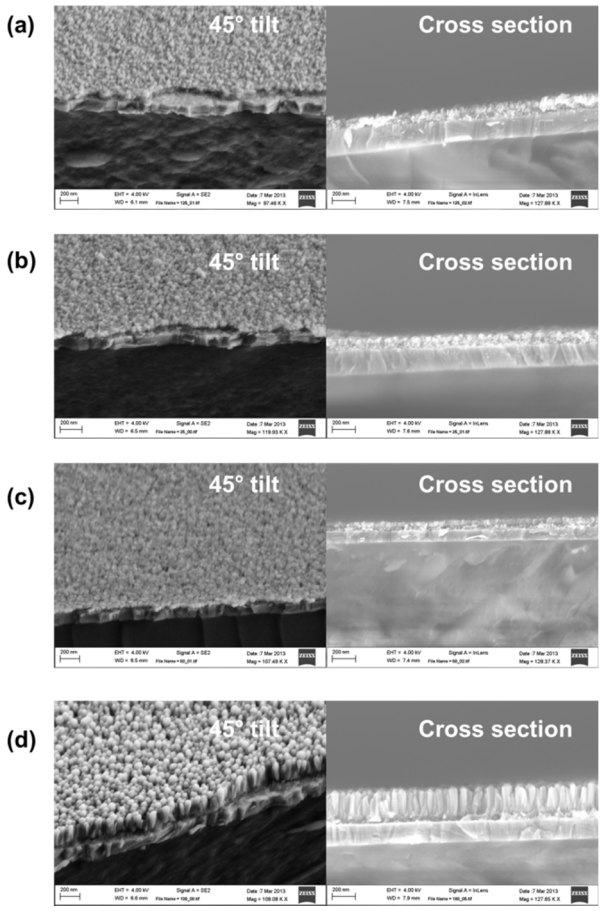

Fig. 4-1-6. SEM images (45° tilt angle and cross sectional) of ZnO nanorods hydrothermally grown at 92.5 °C for 60 minutes at an equal molar concentration of the two reactants at (a) 6.25 mM, (b) 12.5 mM, (c) 25 mM and (d) 50 mM.

The Effect of Different Reactor Design.

Although all the reactors have the same inner volume for the hydrothermal solution, there is a difference between the two reactors in terms of their exposed surface material (mostly Teflon) and relative surface areas (Fig. 4-1-7). Reactor 1 has a thicker stainless steel wall (~4 cm)and a thinner Teflon wall (~2.5 cm), while Reactor 2 has a thinner stainless steel wall (~2 cm) and a thicker Teflon wall (~5 cm). The height of the nanorods turned out to be comparable at around 850-900 nm, but the morphology is slightly different, with more high-low nanorods for the Reactor 1 than Reactor 2. My conclusion is that the reactor design and materials do effect growth and should be kept consistent to obtain reproducible nanorod growth.

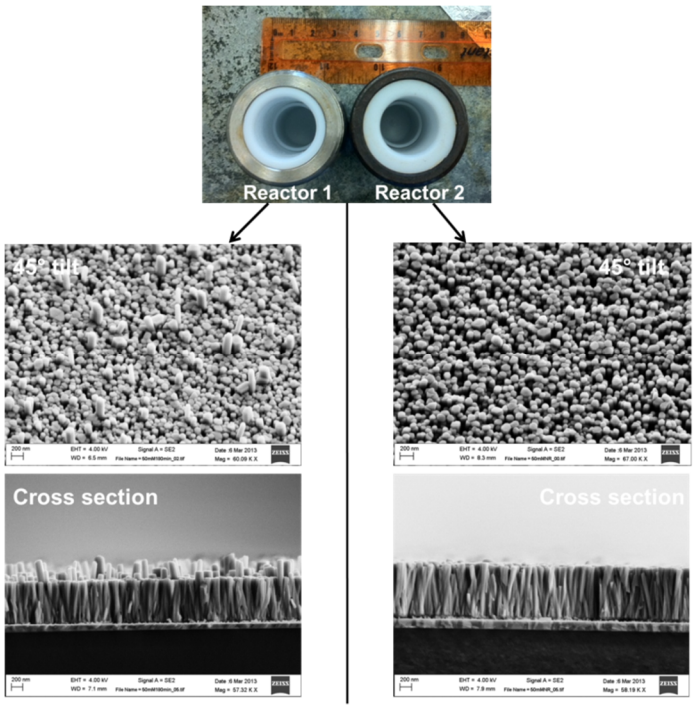

Fig. 4-1-7. SEM images (45° tilt angle and cross sectional) of ZnO nanorods hydrothermally grown at 92.5 °C for 180 minutes with an equal molar concentration of the two reactants at 25 mM, in Reactor 1 and 2, respectively.

The Effect of Growth Temperature.

It was found that the nanorods grown at 115 °C and 92.5 °C have a relatively similar density on the substrate, while at a lower temperature of 70 °C the nanorod density is significantly decreased. Therefore a relatively high temperature is necessary to sustain high density nanostructures to be synthesized (Fig. 4-1-8).

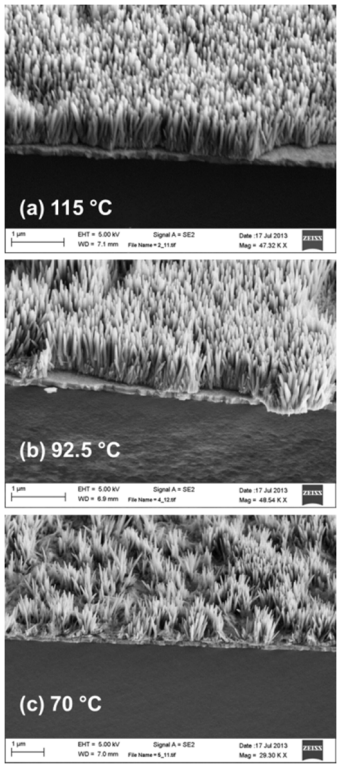

Fig. 4-1-8. SEM images (45° tilt angle and cross sectional) of ZnO nanorods hydrothermally grown for 120 minutes at an equal molar concentration of the two reactants at 25 mM, at a temperature of (a) 115 °C, (b) 92.5 °C and (c) 70 °C.

4.1.2 TEM Studies

The ZnO nanorods were also examined by TEM, and show typical lattice fringes of 0.26 nm (Fig. 4-1-9). In the e-PT/ZnO nanorod system, one can clearly distinguish the amorphous polymer layer around the ZnO nanorods (Fig. 4-1-10).

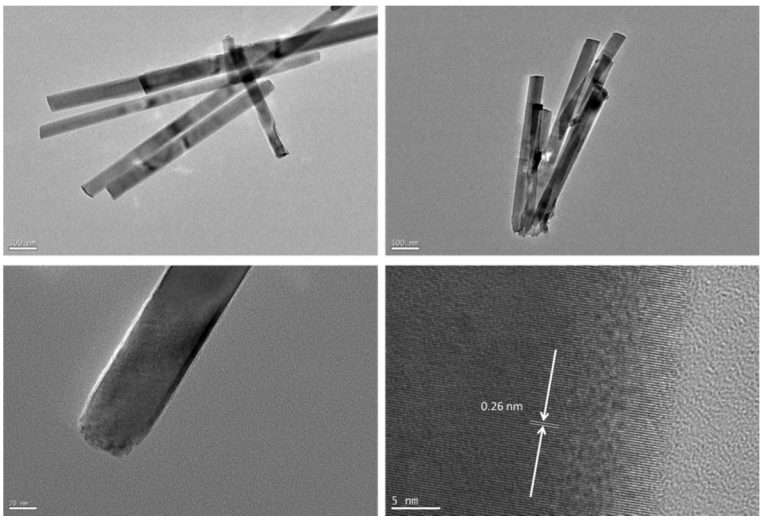

Fig. 4-1-9. TEM images of ZnO nanorods without e-PT

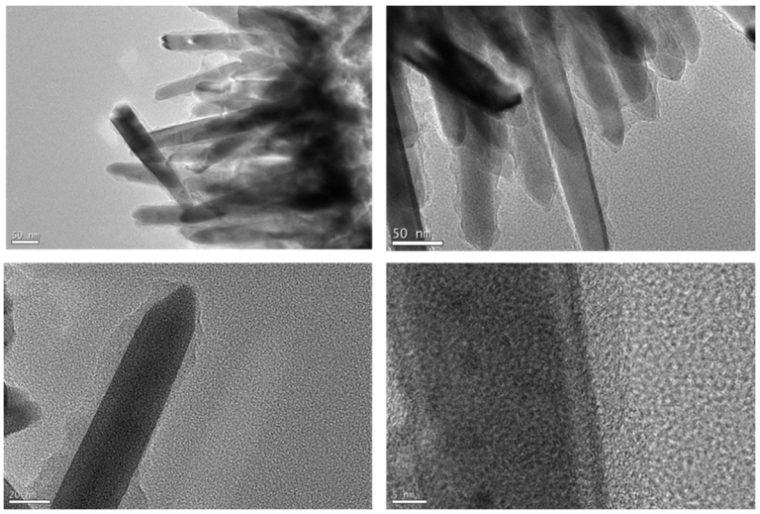

Fig. 4-1-10. TEM images of ZnO nanorods with e-PT

4.2 Interfacial Bonding

Electropolymerization has recently been applied to the fabrication of efficient hybrid solar cells. Exemplary reports include e-P3HT/CdS nanorods[7], e-P3HT/CdS/ZnO nanorods[8], e-PEDOT [Poly(3,4-ethylenedioxythiophene)]/ZnO nanorods[9] and e-P3HT[10] or e-PEDOT[11] on GaAs nanowires. However, fundamental and in-depth studies of the electropolymerized polymer/inorganic interface, most critical for the charge separation process, have been limited. Our X-ray photoelectron spectroscopy (XPS) studies shed light on the bonding nature, chemical structure and molecular orientation of e-PT on ZnO planar and nanostructure substrates. These studies, in turn, serve as an important basis in helping develop a fundamental understanding of the charge separation that occurs at the organic-inorganic interface. We compare our results to adsorption studies of sulfur-containing molecules (alkylthiol[12-15], thiophene[16, 17] and sexithiophene[18-20]) on ZnO surfaces.

Electropolymerization is controlled by a variety of parameters, among which we found the polarity of the solvent exerting a strong influence on the e-PT film morphology along ZnO nanorods. Versatile manipulation of e-PT film morphology on ZnO nanorods can be achieved by tuning the polarity of the solvent, producing either a core-shell or bulk heterojunction (BHJ) structure. For the BHJ structure, XPS depth profiling shows that the polymer has completely infiltrated to the bottom of the nanorods upon thermal annealing.

Photovoltaic *J-V* characterization was performed on e-PT/ZnO bilayer and BHJ devices. The BHJ devices incorporate a polymer overlayer on top of the nanorods, intended as an electron blocking layer for device improvement. However, as the

electropolymerization produces thicker films (such as this overlayer), the polymer structure becomes increasingly regiorandom which results in poor electronic properties such as lower carrier mobilities. Replacing this BHJ structure with a core-shell structure with thin e-PT films along ZnO nanorods, should result in higher quality devices and is the focus of ongoing research.

4.2.1. Experimental Methods

Materials. Zinc acetate dihydrate (99%, Aldrich), zinc nitrate hexahydrate (99%, Aldrich), ethanolamine (99%, Aldrich), hexamethylenetetramine (HMTA, 99%, TCI America), 2,2'-bithiophene (98%, TCI America), tetrabutylammonium hexafluorophosphate (Bu_4NPF_6, 98%, TCI America), 2-methoxyethanol (99%, Acros), dichloromethane (DCM, 99.8%, Acros) and acetonitrile (ACN, 99.8%, Aldrich) were used without further purification. Clevios^{TM} HTL Solar PEDOT:PSS, poly(3,4-ethylenedioxythiophene):poly(styrenesulfonate), was purchased from Heraeus. ITO-coated glass slides (Delta Technologies and MTI Corporation) were subjected to successive 10-minute ultrasonication in dichloromethane and acetone before being blown dried in a stream of nitrogen.

Synthesis of ZnO Planar and Nanorod Substrates. ZnO films were made by a sol-gel method. A 750 mM zinc acetate solution in 2-methoxyethanol of equal molar ratio of zinc acetate and ethanolamine, was spin-coated at 2000 rpm for 30 seconds. Then the sol-gel films were annealed on a hot plate in air at 300 °C for 10 min. This sol-gel method afforded ZnO films that are ~30 nm thick. For the synthesis of ZnO nanorods, the sol-gel prepared ZnO film was used as a seed layer. ZnO nanorods were grown from

the ZnO planar substrate by a hydrothermal method in a Teflon-lined stainless steel reactor. The substrate was suspended and facing down in 12 mL solution of 25 mM zinc nitrate hexahydrate and 25 mM hexamethylenetetramine (HMTA) at 92.5 °C. The mechanism for the hydrothermal growth of ZnO nanorods is illustrated in the equations below:[21]

$$(CH_2)_6N_4 + 6H_2O \leftrightarrow 6HCHO + 4NH_3 \quad (1)$$

$$NH_3 + H_2O \leftrightarrow NH_4^+ + OH^- \quad (2)$$

$$Zn^{2+} + 2OH^- \leftrightarrow Zn(OH)_2 \leftrightarrow ZnO + H_2O \quad (3)$$

The as-grown ZnO nanorods were thoroughly rinsed with distilled water and dried in air.

Electropolymerization. Electrochemical experiments were carried out with a Princeton Applied Research VersaSTAT potentiostat. A three-electrode system was used. The working electrode was the ZnO substrate. The counter electrode was Pt gauze. The reference electrode was a Ag/Ag^+ non-aqueous reference electrode consisting of 0.01 M $AgNO_3$ and 0.1 M Bu_4NPF_6 in acetonitrile (ACN). All potentials reported in this paper were referenced to this Ag/Ag^+ reference electrode. The electrochemical cell contains ~12 mL solution of 0.01-0.05 M 2,2'-bithiophene and 0.1 M Bu_4NPF_6 in dichloromethane (DCM) or acetonitrile (ACN). Before electropolymerization, the solutions were deoxygenated by bubbling nitrogen through the solution for 10 minutes; a nitrogen overpressure was maintained throughout the experiment. PT can be electropolymerized onto the working electrode potentiodynamically (cycling potentials) or by potentiostatic methods (keeping the potential constant). The sample was then

removed from the solution and rinsed with copious amount of solvent. The sample was reduced by a standby potential of -1 V (vs. Ag/Ag^+ reference electrode) in a monomer-free electrolyte solution until the current was stable. The sample was again removed from solution and rinsed thoroughly.

Device Fabrication and Testing. The e-PT/ZnO samples were annealed at 300 °C in argon for 30 minutes. PEDOT:PSS was deposited from a solution which was spin-coated at 1000 rpm/s for 30 seconds and annealed in air on a hot plate at 120 °C for 3 minutes. This produced a PEDOT:PSS layer of ~50 nm thickness. The top electrodes, 80 nm Ag with an electrode area of 0.03 cm^2, were thermally evaporated in vacuum with a base pressure $\leq 1\times10^{-6}$ Torr. Photovoltaic J-V characterization was carried out using a HP 4140B pA Meter/DC Voltage Source under AM 1.5 illumination of 100 mW/cm^2 with a 300 W xenon solar simulator. A Labview program was used on the solar simulator as well as the electrical characterization equipment through which voltages between -1V and 1V were delivered to the solar cell with a step size of 10 mV.

Characterization Methods. A Thermo Scientific K-Alpha X-ray photoelectron spectroscopy system was used for XPS measurements. The photoelectron take-off angle was typically 90° and the X-ray source was monochromated Al Kα radiation (1486.3eV). The binding energy was referenced to the adventitious C 1s peak at 285.0 eV. Shirley background subtraction was performed and the spectra were fit with Gaussian/Lorentzian peaks using a minimum deviation curve fitting method (part of the Avantage software package). The surface composition of each species was determined by the integrated peak areas and the Scofield sensitivity factor provided by the Avantage software. Argon sputter depth profiling was performed using a 2 keV Ar^+ beam at high

current density on an area of 2 mm ×2 mm. Under this condition, the estimated sputter rate (calibrated for Ta_2O_5) is 0.50 nm/s.

UPS data were collected with a He discharge source which produces resonant lines by capillary discharge at 21.2 eV (He I) and 40.8 eV (He II). The analyzer was a cylindrical mirror analyzer and the pass energy was set at 10 eV. The energy resolution was determined to be ~150 meV by the width of the Fermi step measured on clean Au. A negative bias of 4.8 V was applied to the sample to overcome the detector work function limitations when measuring the onset of secondary electron energy cutoffs (the vacuum level).

UV-visible absorption spectra were recorded on a Shimadzu UV-3101PC UV-vis spectrophotometer. PL spectra were obtained on a Horiba Jobin Yvon Fluorolog-3 spectrofluorometer.

The morphology of the ZnO nanorods and e-PT was visualized by scanning electron microscopy (Zeiss Sigma Field Emission SEM).

4.2.2. Results and Discussion

4.2.2.1 Overview of Synthesis Methods

The syntheses involved in this paper are of ZnO films, nanorods and electropolymerization on various ZnO substrates (Scheme 4-2-1). ZnO films were prepared by a sol-gel technique. Compared to other synthesis methods, sol-gel has many advantages such as low material and equipment cost and ease of large-area fabrication.

Subsequently, the as-prepared ZnO thin films serve as a seed layer for the hydrothermal synthesis of ZnO nanorods.

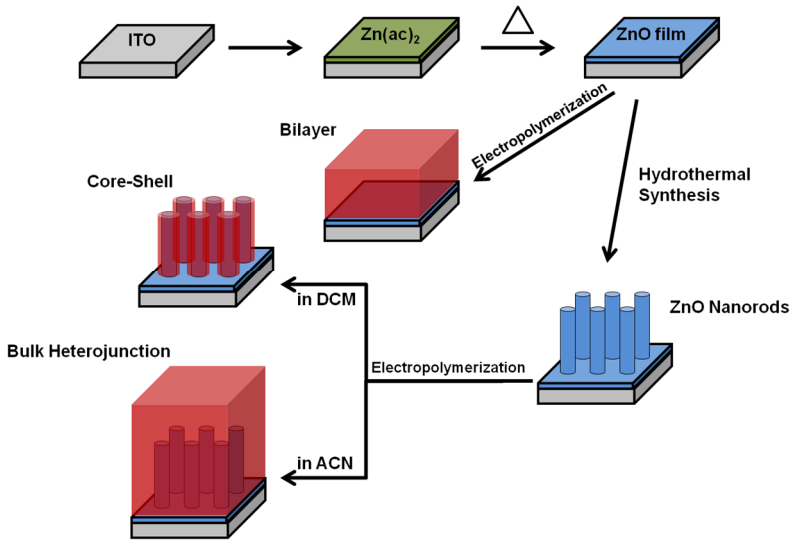

Scheme 4-2-1. Synthesis of ZnO planar and nanorod substrates and electropolymerization. DCM: dichloromethane; ACN: acetonitrile.

In our case, the as-grown ZnO nanorods adopt a vertical alignment to the substrate if the nanorods and the substrate are lattice matched.[22] ZnO nanorods grown on a ZnO seed layer are epitaxial and show preferential growth in a direction normal to the surface as evidenced by the very large intensity of the (002) diffraction peak in XRD as noted in the previous section (Fig. 4-1-2). The high nanorod density observed meets the desired high surface area structure that was initially proposed. Such a structure is needed for efficient charge separation in a hybrid organic-inorganic PV. ZnO nanorods have a polar Zn-terminated (0001) or O-terminated ($000\bar{1}$) tip and non-polar mixed-terminated ($10\bar{1}0$) sidewalls. The polar Zn-(0001) or O-($000\bar{1}$) tip have higher energy than the non-polar sidewalls, and thus either form complex surface structures or undergo

reconstruction to reduce their electrostatic energy.[6] ZnO growth occurs favorably on the higher energy (0001) and $(000\bar{1})$ surfaces to reduce the overall free energy of the system, forming one-dimensional ZnO nanostructures.

Electropolymerization of PT was carried out on both ZnO planar substrates and on nanorods. For electropolymerization on ZnO nanorods, we observe thin conformal core-shell structures or thicker but less conformal structures depending on the solvent used in the electrochemical solution. The mechanism for electropolymerization of conjugated polymers on ZnO substrates is as follows: the monomers diffuse to and adsorb on ZnO surfaces. As electropolymerization begins, the monomers are electro-oxidized and produce radical cations. This is followed by the coupling of two radical cations, expulsion of H^+, and a repetition of this process, forming oligomers and eventually polymers.[23]

The high oxidation potential of unsubstituted thiophene is close to the degradation potential of e-PT. This results in the formation of many side products, cross-linking and shortened conjugation length which is detrimental to charge transport. The usage of 2,2'-bithiophene decreases the polymerization potential by a significant 0.7 V; this helped guide our choice of monomer.[24] The required minimal oxidation potential for 2,2'-bithiophene, is experimentally determined to be 0.80 V in acetonitrile and 0.90 V in dichloromethane (vs. Ag/Ag^+ reference electrode). The 0.1 V difference in minimal oxidation potential, is likely due to the different liquid junction potentials at the reference electrode in two different solvents. With a given solvent, the required minimal oxidation potential of e-PT formation on ZnO planar or nanorod substrates is the same. This is presumably because the unintentional doping (note that both zinc nitrate and HTMA are

only of 99% purity) during hydrothermal synthesis is significant enough to produce highly doped ZnO nanorods with small electrical resistance.

4.2.3 Interfacial Bonding of e-PT/ZnO: XPS

The organic-inorganic interface is considered to be critical for charge separation and device performance. We performed XPS studies on the interfacial bonding between e-PT and ZnO, which include both the ZnO planar substrates (section 3.2.1) and ZnO nanorod substrates (section 3.2.2).

4.2.3.1 e-PT/ZnO Planar Substrate

The XPS analysis depth from which meaningful information can be derived is less than 10 nm, thus the electrodeposited polymer film should be as thin as possible so that information about the interface can be discerned. To maximize the signal-to-noise ratio of various elements (carbon and sulfur from e-PT, zinc and oxygen from ZnO) at the interface, it would be best to have only one monolayer adsorbed across the entire substrate because further growth would attenuate the intensity of these interface species. In reality, the very beginning of electropolymerization is characterized by nucleation and growth into island-like deposits.[25] Therefore, it is highly unlikely that one monolayer adsorption with perfect coverage will occur. We have found that the best interface signal is achieved by electropolymerizing a very thin layer of e-PT on ZnO planar substrate at 1.0 V (0.2 V higher than the minimal oxidation potential) for only 0.4 second in a dilute 0.01 M monomer solution in acetonitrile. The mild potential combined with short polymerization time in dilute solution, is successful in obtaining polymer films that give

satisfactory XPS intensity without being too thick and obscuring information at the interface.

Theoretical cluster calculations[17] on thiophene adsorption shows that there are two lower energy bonding configurations of adsorbed thiophene on ZnO: S-Zn and C-Zn. The interaction between thiophene and O is considered to be energetically much less favorable. Our XPS study also focuses on the two possible bonding structures, S-Zn and C-Zn, at the interface.

The wide energy XPS spectrum of the electrodeposited PT film on a planar ZnO substrate (Fig. 4-2-1a), confirms the chemical composition of the pure ZnO film. A detailed scan of the S 2p peak energy region from a PT/ZnO structure is shown in Fig. 4-2-1b. Curve fitting suggests that there are two S 2p spin-orbit doublets, with the $2p_{3/2}$ peaks centered at 163.8 (dashed line) and 161.9 eV (solid line), respectively. Both of the doublets have a splitting of 1.2 eV and the ratio of $2p_{3/2}$ to $2p_{1/2}$ peak areas can be fit to the expected 2:1. The higher binding energy peak at 163.8 eV is attributed to sulfur in thiophene. The lower binding energy peak at 161.9 eV is typical of sulfide,[26] which is presumably ZnS. By contrast, there is no sulfide peak present in the bulk PT film spectrum (Fig. 4-2-2), indicating that the sulfide peak originates from the interface. Sulfur in the sulfide form represents 31% of the total amount. Additionally, the lack of an oxidized S 2p peak normally appearing at higher binding energy ~168 eV,[27] indicates that the polymer film is not over-oxidized under our mild oxidation conditions and there is no sulfur-oxygen bonding (which is deemed unfavorable by calculation).[17] The resolution and intensity of the 161.9 eV peak demonstrates the existence of sulfide bonding at the interface. It should be noted that the slope on which the S 2p peaks rest is

part of a plasmon loss feature from the Zn 3s transition and is unrelated to the S 2p signal.

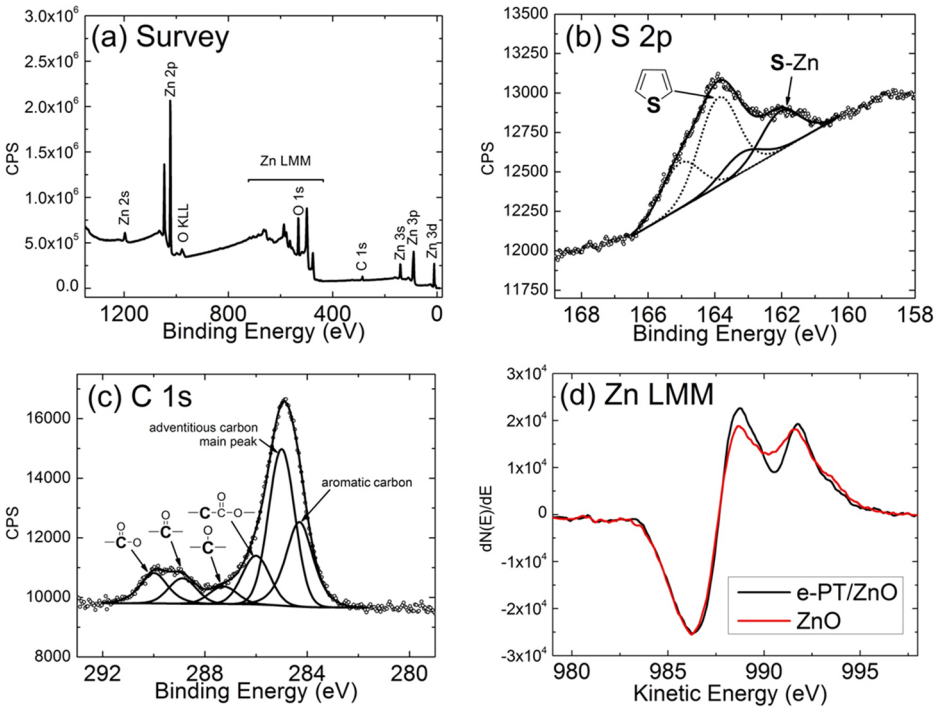

Fig. 4-2-1. (a) Wide energy, (b) S 2p, and (c) C 1s XPS spectra of e-PT on ZnO planar substrate. (d) First-derivative Zn $L_3M_{4,5}M_{4,5}$ Auger spectrum of ZnO planar substrate with e-PT coverage (black line) and without e-PT coverage (red line).

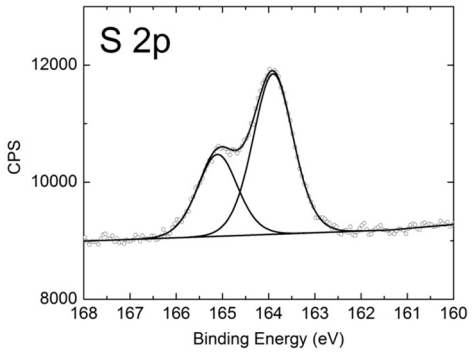

Fig. 4-2-2. S 2p XPS spectrum of a bulk (thick) e-PT film. The shoulder present in ultrathin films corresponding to e-PT/ZnO binding, is no longer visible.

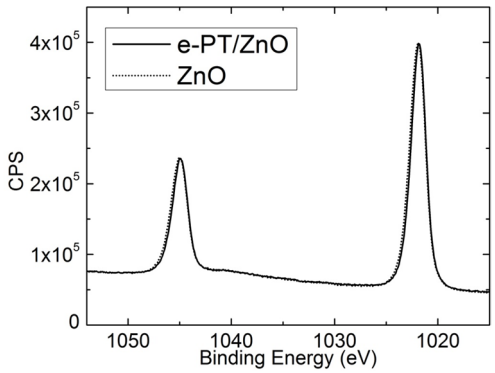

Fig. 4-2-3. Zn 2p XPS spectra from a planar ZnO substrate with e-PT coverage (solid line) and without e-PT coverage (dotted line).

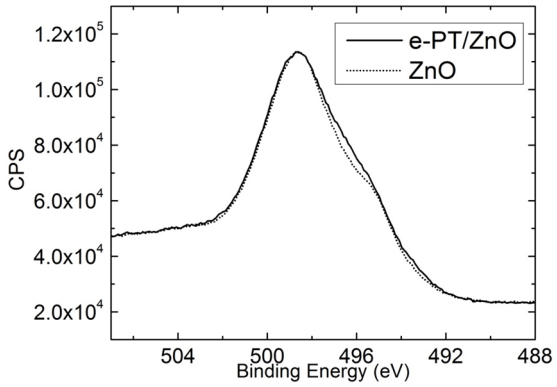

Fig. 4-2-4. Zn $L_3M_{4,5}M_{4,5}$ Auger spectra of ZnO planar substrate with e-PT coverage (solid line) and without e-PT coverage (dotted line).

The C 1s (Fig. 4-2-1c) can be interpreted as arising from aromatic α and β carbons from e-PT, as well as adventitious carbon. The main peak of adventitious carbon was referenced to 285.0 eV. Four higher binding energy peaks (286.0, 287.3, 288.9 and 290.0 eV) are attributed to various oxidation states. Conjugated aromatic polymers such

as PT, may have a weak satellite with a binding energy that is 6-7 eV higher than the primary peak due to a π-π^* shake-up transition. The complex region around 291-292 eV makes peak fitting with a shake-up satellite very difficult and therefore this weak shake-up feature was not included in the fitting. The lower binding energy peak at 284.3 eV is attributed to the aromatic carbons (in α and β position) of e-PT.[28] There is no discernible lower energy shoulder below 283 eV, which should be the peak position for the metal-carbon bond (carbide).[29, 30] Therefore, the aromatic carbon ring was found to have no direct chemical bonding with Zn in the substrate. The atomic ratio of C:S is approximately 4.06:1, which is in agreement with the theoretical ratio of 4.00 for the monomer bithiophene used in electropolymerization. This indicates that the monomer largely maintains its molecular composition and does not experience structural damage such as ring-opening during electropolymerization.

The electron inelastic mean free path (IMFP) of the Zn 2p photoelectron is ~1 nm.[31] Hence, ~95% of the Zn 2p photoemission intensity originates from the top 3 nm layer of the sample. The outermost monolayer of ZnO was reported to be ~0.26 nm thick.[32] Assuming that the interfacial bonding occurs within this ZnO monolayer at 100% coverage (the active Zn sites should be much fewer in reality), the Zn available to bond to e-PT only represents a small fraction ($\leq$ 0.26 nm/3 nm = 9 %) of the observable Zn and the majority of the Zn signal originates from the bulk ZnO film. In order to extract additional information for this study, the Zn $L_3M_{4,5}M_{4,5}$ Auger lines were analyzed. They are the Zn features that are most sensitive to changes in oxidation states, with a relatively big shift of ~5 eV from Zn to ZnO, compared to a shift of only 0.1-0.2 eV in the Zn 2p XPS lines (Fig. 4-2-3).[33] The original spectrum of the Zn $L_3M_{4,5}M_{4,5}$ Auger peak is a

broad feature with a shoulder (Fig. 4-2-4). Differentiation of the Auger spectrum can remove the background and enhance the features hidden in overlapping peaks. The first-derivative Zn $L_3M_{4,5}M_{4,5}$ Auger spectra of ZnO substrate (red line) and e-PT/ZnO (black line) are shown in Fig. 4-2-1d.[34] Both spectra have two positive peaks at ~991.7 eV and ~988.7 eV and one negative peak at ~986.3 eV. The differentiation of the original Auger peak produces a curve with a positive swing/excursion and a negative swing/excursion. The positive peak at 991.7 eV represents the positive excursion of the differentiated Zn peak, while the negative peak at 986.3 eV comes from the negative excursion of the differentiated ZnO peak. Both of these peaks showed little change in intensity before and after electropolymerization. The positive peak at 988.7 eV in the ZnO substrate spectrum, results from overlapping of the negative excursion of Zn and positive excursion of ZnO. This peak height has increased in the region with e-PT coverage compared to the substrate with no coverage. With the peak height of Zn and ZnO unchanged, the most probable scenario would be that there is a third component arising within this region which leads to the peak height increase. The peak separation between ZnS and Zn in the Auger spectrum is ~3 eV.[16, 35] With the Zn positive peak at 991.7 eV, the ZnS peak should appear at 988.7 eV if it exists. This kinetic energy coincides with the position where the peak intensity increases, implying that the third component is ZnS. Previous S 2p XPS analysis, supported by this Zn LMM Auger study, firmly proves the existence of direct Zn-S bonding at the interface.

Thiophene can be oriented parallel to or upright from the ZnO surface, via its aromatic carbon ring π electrons or the S lone pair of electrons, respectively. The change in thiophene bonding geometry from lying flat on the surface to standing upright from the surface (or any angle in between), is dependent on the coverage of the adsorbed thiophene.[16] Experimental and theoretical studies on sexithiophene (an oligomer that closely resembles short polymeric chains in e-PT) adsorption on TiO_2[18], SiO_2[19] and ZnO[20] all point to two predominant binding geometries as shown in Scheme 2: (i) standing up with its long axis normal to the surface and (ii) lying flat on the surface. One interesting observation about sexithiophene adsorption on SiO_2, demonstrated that for submonolayer coverages, molecules standing up along their molecular axis coexist with those who are lying down on the substrate. When the first monolayer is completed, all sexithiophene molecules stand up on the surface and flat-lying molecules cannot be detected.[36] At low coverages, the flat-flying orientation is more energetically stable owing to a stronger orbital overlap between the thiophene π electrons and the substrate surface. For a monolayer or higher coverage, the total system energy (polymer-polymer intermolecular plus polymer-surface interactions) results in an upright orientation being favored.[20] This is most likely our case with more than one monolayer coverage of e-PT on ZnO, therefore the upright molecular orientation is expected. The S-end of the molecule and Zn forms chemical bonds, while the aromatic carbon ring has minimal interaction with the surface due to this specific geometry.

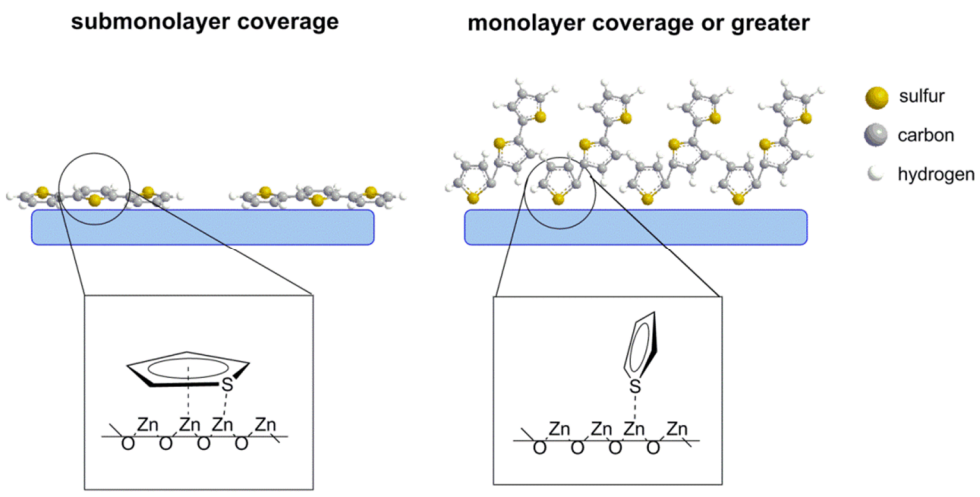

Scheme 3-2-2. Molecular geometry and bonding structure for e-PT on ZnO planar substrates at different coverages.

We also performed solution phase immersion of ZnO planar substrate in 2,2'-bithiophene (BT) ACN solution and we also observed indication of S bonding to Zn: From Fig. 4-2-5, we can see that the S 2p shows a shoulder that is as prominent as the polythiophene on ZnO case. Solution-immersion also makes Zn-S bond. No visible Zn-C interaction seen here.

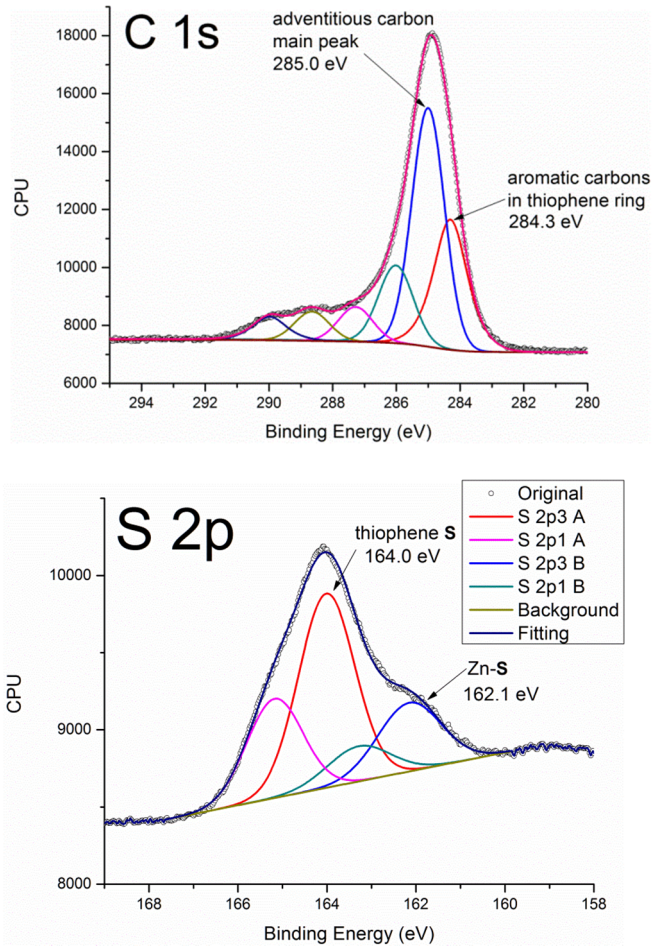

Fig. 4-2-5 Solution immersion experiment: XPS C 1s and S 2p.

4.2.3.2 e-PT/ZnO Nanorod Substrate

In order to investigate the e-PT/ZnO nanorod interface, thin films of e-PT were electropolymerized onto ZnO nanorods at a low potential 0.95 V (barely over the 0.90 V minimal oxidation potential) for ~77 seconds in a dilute 0.01 M monomer solution in dichloromethane.

The XPS wide energy scan is similar to the one observed for e-PT on ZnO films, thus it is omitted here. The S 2p spectrum (Fig. 4-2-6a) shows a single doublet with the $2p_{3/2}$ peak centered at 163.8 eV, which is in excellent agreement with our previous measurement of the S 2p binding energy at the interface of e-PT/ZnO films. The doublet, with its S $2p_{3/2}$ peak centered at 163.8 eV, is in agreement with previous measurement on e-PT/ZnO films. There is no discernible ZnS shoulder in the S 2p spectrum of the e-PT/ZnO nanorod sample at lower binding energy, indicating a lack of chemical bonding between S and Zn. This is quite different from the e-PT/ZnO film interface, where a major peak was observed at 161.9 eV and attributed to Zn-S bonding.

In the C 1s spectrum (Fig. 4-2-6b), the aromatic carbon peak shows up at the same binding energy as our above-noted results at 143.7 eV. There are four carbon peaks at higher binding energy (286.6, 287.5, 289.0 and 290.2 eV) with similar assignments as the above-mentioned e-PT/ZnO film samples. A broad feature centered at 291.8 eV can be clearly modeled and is designated as the π-π^* shake-up satellite. The lack of lower binding energy shoulder at around 281-282 eV, demonstrate that a strong covalent interaction between aromatic C and Zn is non-existent.

The Zn $L_3M_{4,5}M_{4,5}$ first-derivative Auger spectrum (Fig. 4-2-6c) shows virtually no intensity change for the three peaks (986.3 eV, 988.9 eV and 992.0 eV) with or without e-PT coverage, further verification that there is no ZnS bond at the interface. The kinetic energy of all three peaks is in agreement with the previous assignment on the e-PT/ZnO film.

The amine used during the hydrothermal synthesis, HMTA, may still be present on the surface of the nanorods and interfere with the adsorption of e-PT onto ZnO

nanorods. In one report, HMTA is suspected to adsorb on the non-polar facets of ZnO nanorods and mediate their aspect ratio during hydrothermal growth.[36] However, such a hypothesis is contradicted by other studies which argue that HTMA is likely to decompose rapidly at elevated temperatures during the synthesis to yield formaldehyde and ammonia.[21, 37] Even if there is amine present on the sidewalls of the as-grown nanorods, the adsorption is weak enough that rinsing with water should eliminate its presence, as is evidenced in a report about ethyelenediamine adsorption on ZnO nanorods.[18] In order to confirm that no HMTA adsorption on ZnO nanorods survives rinsing with water, a N 1s XPS scan (Fig. 4-2-6d) was performed and revealed no detectable peak intensity. This points to the lack of HMTA adhesion to the non-polar facets of ZnO nanorods after rinsing with water, hence we rule out the possibility of HMTA interference with the adsorption of e-PT on ZnO nanorods. In summary, there is no indication of sulfide or carbide bonding of e-PT on ZnO nanorods from XPS and Auger analyses. In addition, there is no HMTA present on the nanorods to interfere with our interpretation.

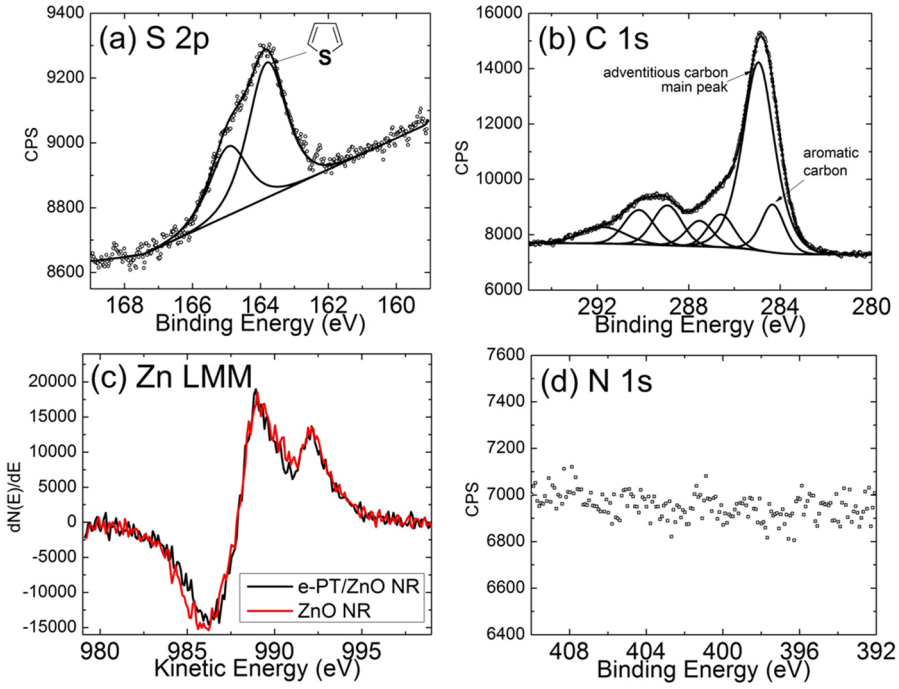

Fig. 4-2-6**.** (a) S 2p, (b) C 1s XPS spectra of e-PT on ZnO nanorod substrate. (c) First-derivative spectra of Zn $L_3M_{4,5}M_{4,5}$ Auger spectrum of ZnO nanorod (NR) substrate with e-PT coverage (black line) and without e-PT coverage (red line). (d) N 1s XPS spectrum of ZnO nanorod substrate.

4.2.3.3 Polarity and Defects of ZnO Surfaces

Our XPS results show that the as-deposited e-PT interacts strongly with the ZnO planar substrate. It is chemisorbed to the ZnO substrate via sulfur in the thiophene unit. The carbon ring, by contrast, does not appear to have significant direct bonding with the ZnO substrate. By contrast, e-PT does not bond chemically with the ZnO nanorod surface and their interaction is probably limited to pure physisorption (e-PT films can still be grown conformally along the ZnO nanorods, see morphological control section below).

ZnO exhibits strongly anisotropic morphology with a variety of polar and non-polar surfaces. ZnO planar substrates were found to be c-axis aligned with a polar (0001) surface.[38] ZnO nanorods, on the other hand, are mostly comprised of sidewalls that are non-polar mixed-terminated $(10\ \bar{1}\ 0)$ surfaces. Both theoretical calculations and experimental results suggest the non-polar $(10\bar{1}0)$ surface as the most stable face, hence it can be expected to have a lower reactivity relative to the polar Zn-(0001) face.[39] Adsorption studies of various alcohol molecules on single crystal ZnO surfaces also demonstrate the Zn-(0001) face is the most reactive.[40] Selective adsorption of certain moieties on polar and non-polar surface was recently reported, with citric acid selectively adsorbing on ZnO polar surfaces and ethylenediamine on ZnO non-polar surfaces.[18] Alkylthiols were found to adsorb on ZnO films[12, 14, 15] which have polar surfaces, but not on MOCVD-grown ZnO nanorods which consist mostly of non-polar surfaces.[13] We believe the different bonding nature of e-PT to ZnO film and nanorod substrates that we observe is strongly influenced by the different polarity of ZnO surfaces.

The surface chemistry of ZnO can be rather complex. One should consider that surface defect chemistry may also play an important role in mediating the interaction between e-PT and ZnO. Surface defects on ZnO crystals are dominated by oxygen vacancies (V_O).[41] To this end, XPS can be used to quantify the amount of V_O by careful studies of the O 1s and Zn 2p spectra. For ZnO films with e-PT adsorbed, the O 1s peak (Fig. 4-2-7a) can be fit with two peaks centered at 530.4 and 531.9 eV. For e-PT covered ZnO nanorods, the O 1s peak (Fig. 4-2-7b) can be fit with three peaks at 530.0, 531.8 and 533.4 eV. The low binding energy component at 530.2±0.2 eV (denoted as O_A), is

attributed to the O^{2-} ions in the normal wurtzite structure of ZnO.[42] The medium binding energy component at 531.8-531.9 eV (denoted as O_B), has been assigned to two different contributions in the literature: O^{2-} ions in oxygen deficient regions of ZnO,[43] or adsorbed OH groups on the surface (Scheme 3-2-3).[44] Further analysis is needed to delineate the real contribution of O_B. We use the O 1s spectrum of e-PT/ZnO films as an example. If O_B is solely assigned to O^{2-} ions in oxygen deficient regions, then the total oxygen to Zn ratio (O_A+O_B):Zn would be 0.96, which indicates that there are only 4% oxygen vacancies and that ZnO is nearly stoichiometric. This calculation contradicts the observation that there is a prominent O_B component which implies a significant oxygen deficiency (~34% of the total oxygen content at the surface). Therefore, a reasonable explanation is that O_B is the combination of two inseparable peaks of both O^{2-} ions in oxygen deficient regions and OH groups on the surface. The high binding energy O_C peak, which only appears on the ZnO nanorod sample at 533.4 eV, is attributed to loosely bound oxygen species such as H_2O on the ZnO surface.[44] Interestingly, there appears to be an additional Zn $2p_{3/2}$ peak for ZnO nanorod samples: the higher binding energy edge of Zn $2p_{3/2}$ peak is less sharp in the nanorod sample (Fig. 4-2-7d) than in film sample (Fig. 4-2-7c) and this peak must be fit with two components Zn_A and Zn_B at 1021.5 and 1023.3 eV, respectively. We think that Zn_B represents the Zn species bound to oxygen species such as H_2O, similar to the origin of O_C component. The appearance of O_C and Zn_B only in ZnO nanorods, probably stems from the specific synthetic routes. The sol-gel ZnO film was synthesized with thermal annealing in air. The hydrothermal synthesis of ZnO nanorods, on the other hand, was performed in an aqueous solution.[44, 45]

Due to the overlap of the two contributions to the O_B peak which complicates quantification, O_A (normal wurtzite structure) is used to determine the oxygen deficiency in ZnO films and nanorods. The ratio of O_A/Zn is 0.63 and 0.54 for the ZnO film and nanorods, respectively. This indicates that the ZnO film surface has fewer defects (V_O) than the nanorod surface. Studies have shown that the introduction of V_O will reduce the positive charge of the adjacent Zn^{2+} species and increase its probability to chemisorb molecules.[16, 46] If the surface defects played a significant role, the ZnO film surface should have exhibited less chemisorption than ZnO nanorods. However, this is not the case, thus we believe that surface defects are not significant in determining the adsorption behavior of e-PT on ZnO.

To summarize, the different adsorption behavior of e-PT on ZnO planar and nanorod substrates is mainly attributed to different polarity of ZnO surfaces while the influence of surface defects was found to be minor.

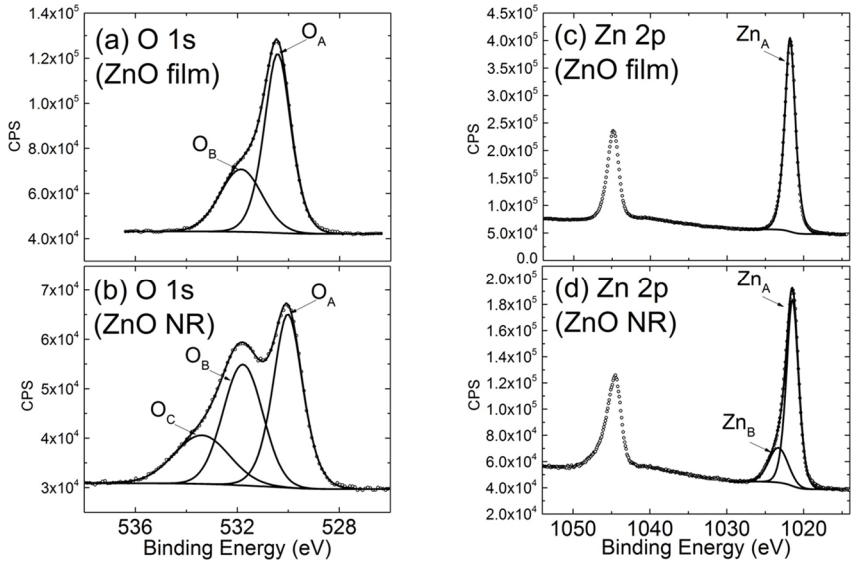

Fig. 4-2-7. O 1s XPS spectra of e-PT covered (a) ZnO film and (b) ZnO nanorod; Zn 2p XPS spectra of e-PT covered (c) ZnO film and (d) ZnO nanorod.

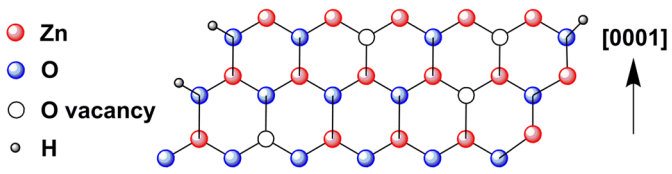

Scheme 3-2-3. Surface structure model of (0001) plane ZnO with oxygen vacancies and OH groups.

4.2.4 FTIR-ATR Studies

We also performed FTIR-ATR experiments, attempting to confirm that we have polythiophene bonding to the surface (Fig. 4-2-8). However, although FTIR-ATR technique is more sensitive to the surface layer comparing to conventional FTIR technique, it is still not surface sensitive enough for our purposes.

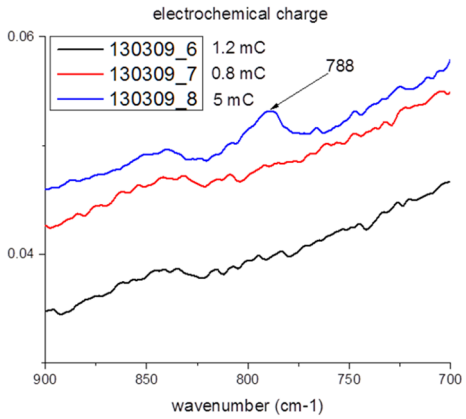

Fig. 4-2-8 FTIR-ATR on e-PT/ZnO planar substrates

FTIR-ATR, though more surface specific than conventional FTIR technique, still is lacking the surface sensitivity we would like. For thinner samples (130309_6 and

130309_7), IR is not sensitive enough to pick up information about the interface: no peak around 788 cm^{-1} intensity that is characteristic of the out-of-plane C-H bending of 2,5-substituted rings (such as polythiophene). Thicker sample (130309_8) we are able to see this intensity. From these observations, we can conclude that FTIR-ATR in this case is not sufficiently surface sensitive and the signal we observe can be considered as mainly from the bulk. However, on the other hand, the existence of the signature vibration of the 2,5-subsituted ring proved again that we have obtained polythiophene.

4.3 Morphological Control

As previously mentioned in section 4.1, e-PT film thickness can be regulated by the total electrochemical charge used during electropolymerization. In an ideal situation, the charge applied to the electrochemical system will be completely used to electro-oxidize the monomers and oligomers in the solution to form polymeric layers on the ZnO surface. The polymerization of each bithiophene monomer unit involves the removal of about 2.25 electrons.[48] Therefore, the film thickness *d* can be estimated by the total charge in the monomer oxidation process, Q, using the following equation

$$\left[\frac{Q}{2.25eN_0}\right] M_w = \rho S d$$

where e is the electron charge, N_0 is Avogadro's constant, M_w is the molecular weight of bithiophene (166 g/mol), S is the area of the film (~1 cm^2), and ρ is the density of the film and assumed to be 1.5 g/cm^3.[49] This equation implies a direct proportional relationship between the total charge and the film thickness. In an actual setting, there is always a relatively small portion of the charge being used to form oligomeric species that are soluble in the electrochemical solution yet do not attach to the surface. Nonetheless, qualitatively speaking, the electrochemical charge remains an effective real-time monitor for film thickness during electropolymerization. It is automatically calculated by integrating the area under the I-t curve with the progression of time on our instrument. In the following sections, we vary the electrochemical charge to study the evolution of film morphology in two solvents, dichloromethane (DCM) and acetonitrile (ACN).

4.3.1 Electropolymerization in Dichloromethane: Core-Shell Structure

Electropolymerization of PT on ZnO nanorods in dichloromethane (DCM) was investigated by SEM. Fig. 4-3-1a shows the ZnO nanorod morphology before electropolymerization. After a small charge of ~4 mC was delivered to the electrochemical cell, we observe a core-shell structure with a thin polymer layer of ~30 nm electrodeposited along the ZnO nanorods (Fig. 4-3-1b). The e-PT film is highly conformal and smooth, and there is excellent contact and wetting between e-PT and ZnO. This morphology is particularly encouraging for OPVs as the interfacial surface area is maximized relative to what we observe by spin coating or drop casting. After the polymerization charge is increased to 9 mC, a thicker e-PT shell of ~60 nm was produced over the nanorods (Fig. 4-3-1c). The thicker e-PT film fully coats the area between the rods with polymer and adopts a ripple-like morphology over the tips of the nanorods. These morphology observations indicate that the polymer growth strictly follows the surface of the nanorods and converges between adjacent nanorods at a longer growth time, leaving only the nanorod tips visible to our SEM observation.

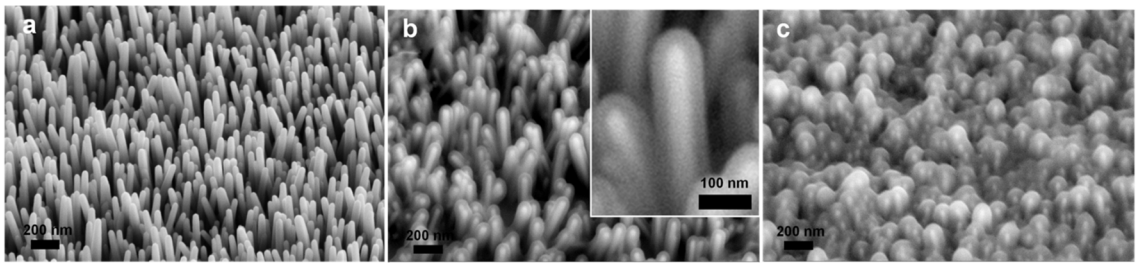

Fig. 4-3-1. 45° tilt angle SEM images of (a) ZnO nanorods before electropolymerization, (b) e-PT/ZnO nanorods at an electrochemical charge of 4 mC and (c) e-PT/ZnO nanorods at a polymerization charge of 9 mC. The solvent used in electropolymerization is dichloromethane (DCM). Inset in (b) shows the magnified view of e-PT/ZnO nanorods.

4.3.1.1 Thermal Annealing on the ZnO Nanorods

ZnO nanorod samples grown with high purity chemicals and rigorous control of the synthetic environment, appear to be more difficult to initiate electrodeposition and are less conductive. This is likely due to the decrease of unintentional doping from impurities in the starting chemicals/solution. We are able to utilize thermal annealing to increase the conductivity of these nanorods and successfully carried out subsequent electrodeposition experiments on them. I believe that In diffusion from the ITO substrate up to the nanorods may be the reason for a higher conductivity and easier electrodeposition reaction to occur. XPS studies were carried out on the thermally treated ZnO nanorods (400 and 600 °C for various times, in argon) and we found no evidence of In present (Fig. 4-3-2). It should be noted that the XPS atomic detection limit is ~1% and any concentration lower than that will not be detected. Given the low concentration of dopants needed to increase the conductivity of the nanorod, XPS studies merely showed that there is not a huge amount of In present.

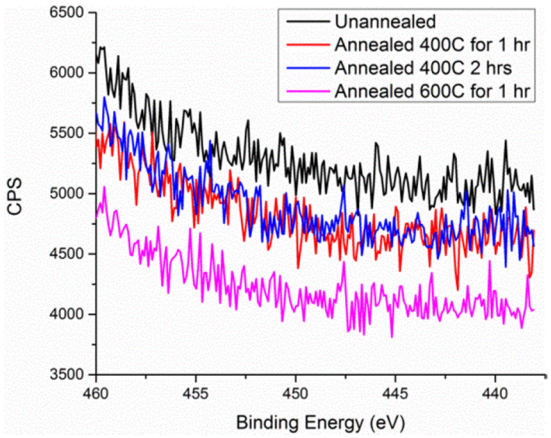

Fig. 4-3-2. XPS In 3d detailed scan of unannealed and annealed ZnO nanorod samples in various conditions.

For ZnO nanorods thermally annealed at 400 °C for 1 hour, electrodeposition can occur, however, the potential applied (1.5 V) is significantly higher than what is normally needed to polymerize (~1.0 V) (see Fig. 4-3-3). The higher potential needed for initiating electropolymerization is probably due to the insufficient doping (most likely In from the ITO substrate) of the nanorods at a lower annealing temperature such as 400 °C for 1 hour.

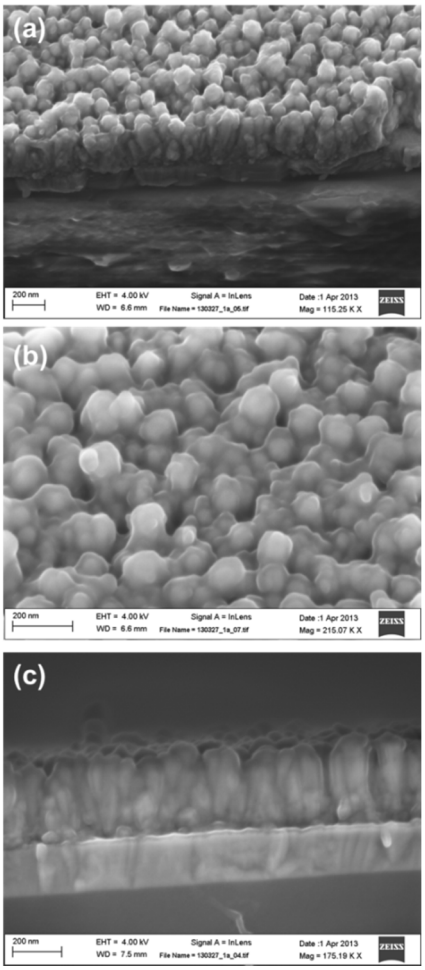

Fig. 4-3-3. SEM images of electrodepositon at 1.5 V for 10 mC (PF_6^- as the electrolyte anion). (a) 45° tilt angle, (b) magnified view of 45° tilt angle and (c) cross sectional.

For ZnO nanorods annealed at 600 °C for 1 hour, electrodeposition can occur on the ZnO nanorods at a much lower potential of 1.0 V. This shows that, not surprisingly, the conductivity of the ZnO nanorods annealed at 600 °C is higher than those annealed at 400 °C. The polymer showed a similarly conformal growth as the 400 °C annealed ZnO nanorod samples (Fig. 4-3-4). It is evident that the polymer infiltration is excellent because we can observe from the bottom of the nanorods to the top that there is continuous polymer coverage (most obvious in the 45 ° tilt angle image, Fig. 4-3-4). The nanorods have a circular curvature on the side walls as they line up forming arrays and we can observe this same circular curvature on the polymer, indicating conformal polymer coverage.

We do observe a certain roughness on these polymer coatings on ZnO nanorods. However, we discovered that by changing the electrolyte, a smoother surface may be attained. In this case, when we used $LiClO_4$ as the electrolyte (as opposed to the Bu_4NPF_6 as was used for the previous trials) we observe a roughness reduction (Fig. 4-3-5).

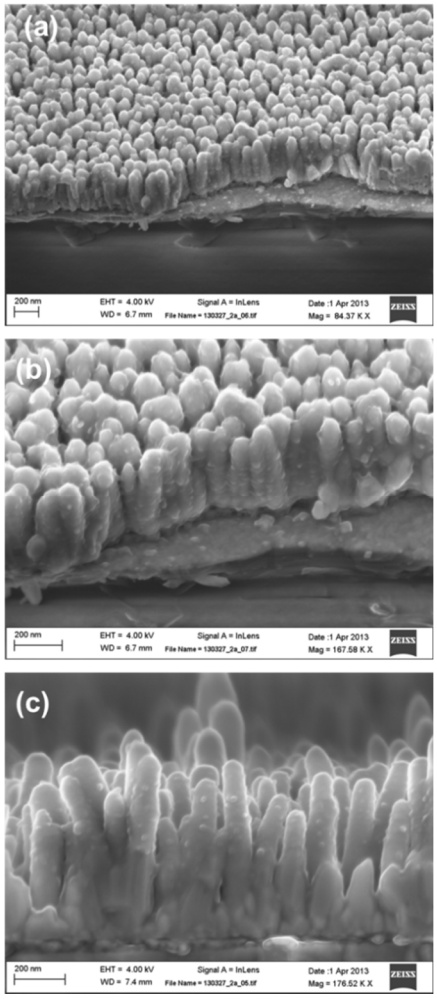

Fig. 4-3-4. SEM images of electrodepositon at 1.0 V for 10 mC (PF_6^- as the electrolyte anion). (a) 45 ° tilt angle, (b) magnified view of 45 ° tilt angle and (c) cross sectional image.

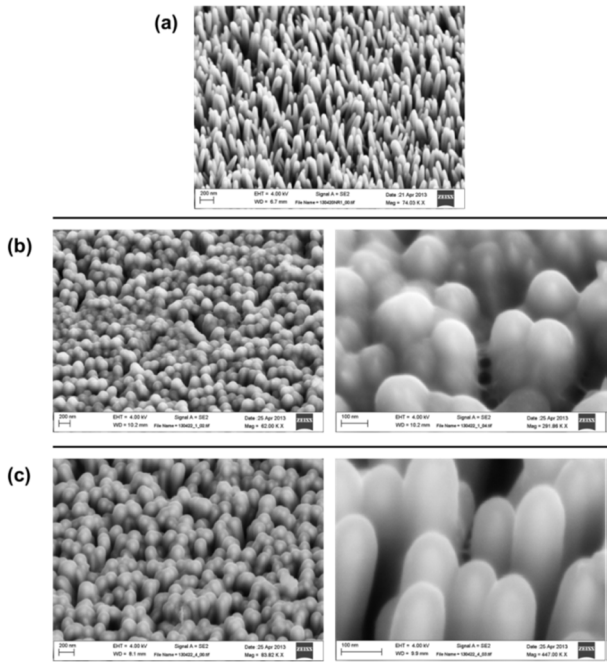

Fig. 4-3-5. 45 ° tilt angle SEM images of (a) ZnO nanorods, (b) electrodepositon at 1.2 V for 50 mC (ClO_4^- as the electrolyte anion), with the 400 °C annealed sample for 1 hour; (c) Electrodepositon at 1.1 V for 50 mC (ClO_4^- as the electrolyte anion), with the 600 °C annealed sample for 1 hour.

Comparing the two electrolytes, one can see that different anions again gave different polymer morphologies with the ClO_4^- produced polymer appearing to be smoother than the PF_6^- one. This again illustrates the strong influence of different anions exert on the final polymer structure and properties. Before it is attached to the surface, it forms oligomers in the solution that are coupled with the anions. The solubility of such oligomers are most likely determined by the anions present in the solution, provided that the solvent is the same. Oligomers that have a lower solubility should deposit onto the substrate faster than more soluble ones. Additionally, solubility will help determine the structure of the polymer and subsequently its morphology.

4.3.2 Electropolymerization in Acetonitrile: Bulk Heterojunction Structure

Polymer films of increasing thickness were deposited in acetonitrile (ACN) as the electrochemical charge was varied from 8 mC to 75 mC. The film morphology in ACN was markedly different than that in DCM. At 8 mC, the charge dispensed through the electrochemical cell afforded a thin polymeric along the ZnO nanorods, though the film growth appears less conformal and more nodular than that in DCM (Fig. 4-3-6a). After a charge of 25 mC was consumed, the polymer forms a thicker overlayer of ~50 nm with substantial roughness on top of the nanorods (Fig. 4-3-6b). For a higher charge of 75 mC, the polymer overlayer grew to ~200 nm (Fig. 4-3-6c). At higher electrochemical charges such as 25 mC or 75 mC, bulk heterojunction (BHJ) structures of interdigitated polymer and ZnO nanorods with a polymer overlayer on top of the nanorods were produced. The polymer overlayer may function as an electron blocking layer and increase the device performance.[50] Therefore, these BHJ structures were used to fabricate solar cells (see section 4.5 for more details about device testing).

Fig. 4-3-6**.** Cross-sectional SEM images of e-PT on ZnO nanorods at an electrochemical charge of (a) 8 mC, (b) 25 mC and (c) 75 mC. The solvent used in electropolymerization is acetonitrile (ACN)

4.3.3 Solvent Polarity

Similar to the influence of surface polarity on interfacial bonding, the polarity of the solvent molecule is a key factor determining film morphology. The higher polarity solvent (ACN) is considered to interact more strongly with the surface than the less polar solvent (DCM), competing with monomer/oligomer adsorption on the surface and in effect reducing the density of polymer nucleation sites.[25] This results in more conformal and intimate contact with the nanorods in DCM than in ACN. The morphologically rougher polymeric overlayer formed in ACN than in DCM may be due to the different solubilities of oligomers in the two solvents.[51] Oligomers are less soluble in ACN than in DCM, thus super-saturation above the electrode is more rapidly attained in ACN, enabling polymeric clusters to deposit onto the electrode and create growing nuclei that promote three-dimensional growth.[52] To summarize, core-shell and BHJ structures can be obtained by altering the solvent used in electropolymerization. Our results demonstrate the surface-initiating nature of electropolymerization and contribute to further understanding of electropolymerization growth kinetics in different solvents.

4.3.4 Complete Polymer Infiltration: XPS Depth Profiling

The polymer filling rate in a BHJ structure can be further improved by thermal annealing. An e-PT/ZnO nanorod sample was electrodeposited potentiodynamically (-0.5 to 1.4 V, 2 cycles, 100 mV/s, in ACN), followed by thermal annealing at 300 °C for 30 minutes in argon. From the SEM image (Fig. 4-3-7a), it is difficult to accurately observe the depth and completeness of polymer infiltration. XPS depth profiling with Ar^+ sputtering (Fig. 4-3-7b) was used as a supplemental technique to probe if the polymer

fully infiltrated the nanorods. The sputtering depth is quantified by the etch time. The most intense and the most suitable XPS peak of each element (C 1s, S 2p, Zn 2p, O 1s and In 3d) was used to determine the atomic percentage at any given etch time. Before the etching time of 500 seconds, the sputtered material consists solely of the polymer overlayer on top of the nanorods as only C and S signals are observed. Then the C and S signals from e-PT gradually decrease as the sputtering penetrates the e-PT/ZnO nanorod network. Meanwhile, the Zn and O photoemission intensities from the ZnO nanorods slowly increase. At 1000 seconds, In (from the ITO substrate beneath the ZnO film) appears in the elemental composition, indicating that the ITO film has been exposed to sputtering. The bombardment of Ar^+ on surfaces not covered by the nanorods should occur earlier than those covered with the nanorods. This results in an overlap of In and Zn signal from 1000 seconds. The C and S signals, with their ratio constant at ~4:1 throughout the etching, coexist with the Zn signal until Zn is completely depleted at 1700 seconds. This suggests that e-PT has infiltrated to the bottom of the dense ZnO nanorod arrays, which leads to higher interfacial area beneficial for PV applications. Also, at the top of the Zn signal, where it is hitting the tip of the ZnO nanorods, the polymer content has approximately dropped to half, that means that the ZnO nanorods approximately cover half of the surface area of the entire substrate. The etching rate of the depth profiling experiment, estimated from the start and the end of the Zn signal (1700 – 500 = 1200 seconds) and the nanorod height measured from SEM (400 nm), is ~0.33 nm/s.

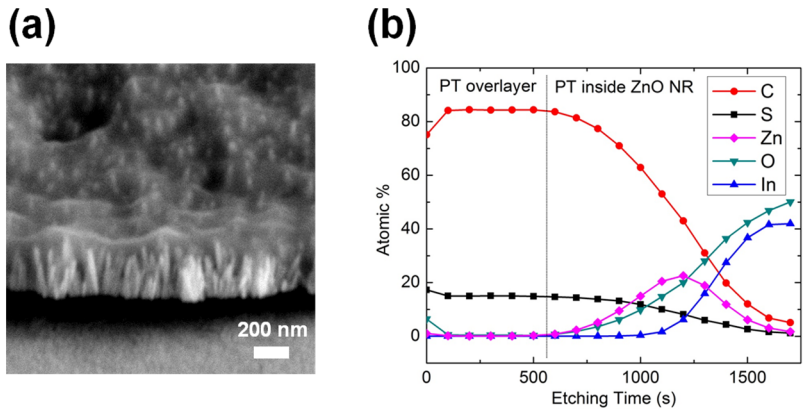

Fig. 4-3-7**.** (a) SEM image (taken at 45° tilt angle) of e-PT on ZnO nanorods after thermal annealing. (b) Plot of atomic percentage and etching time for various elements in XPS depth profiling experiment.

4.3.8 Template Synthesis of Nanoscale e-PT Testtubes

We have ZnO nanorods that are hydrothermally grown at 92.5 C for 120 minutes. Then this nanorod sample is subject to 1.1 V potential for 160 seconds, totaling 106 mC electrochemical charge. This sample shows a relatively uniformly e-PT coated nanorod morphology (Fig. 4-3-8). Although the resolution is not good, the polymer coating is ~40 nm thick in these pictures.

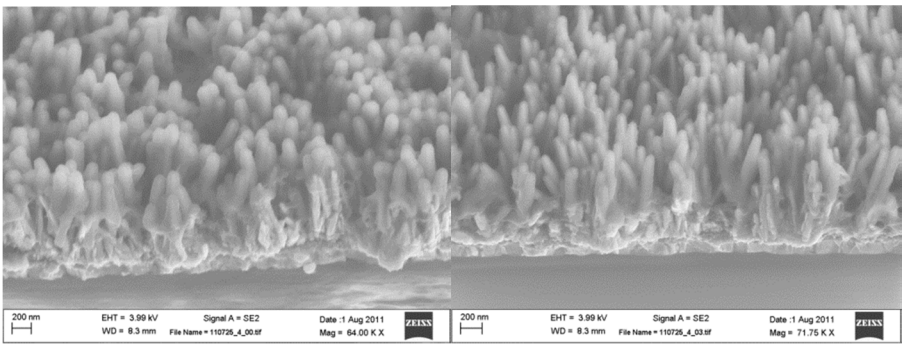

Fig. 4-3-8 45° tilt angle SEM image of e-PT layer coating along the ZnO nanorods (prior to HCl etching)

Template synthesis of nanoscale e-PT testtubes can be achieved by using the ZnO nanorods as the template. The nanorods were then etched away after electrodeposition of a layer of e-PT films along the nanorods. 1M HCl was added to a glass vial containing this sample of e-PT coated nanorods. Vigorous shaking will produce flakes of red/brown color suspended within this solution. We carefully pipette out an aliquot of material and drop cast it on a silicon shard and performed thermal annealing at 110 °C for 30 minutes to remove the water. We see that the ZnO nanorods were completely etched away by HCl and we are left with nanoscale testtube-like structures, with the hollow part closely resembling the morphology of the original ZnO nanorods (some with apparent hexagonal faceting, Fig. 4-3-9). The thickness of e-PT coating here is ~50 nm, close to the estimation of ~40 nm from unetched sample. These nano testtubes can be used as a micro-reactors for certain applications.

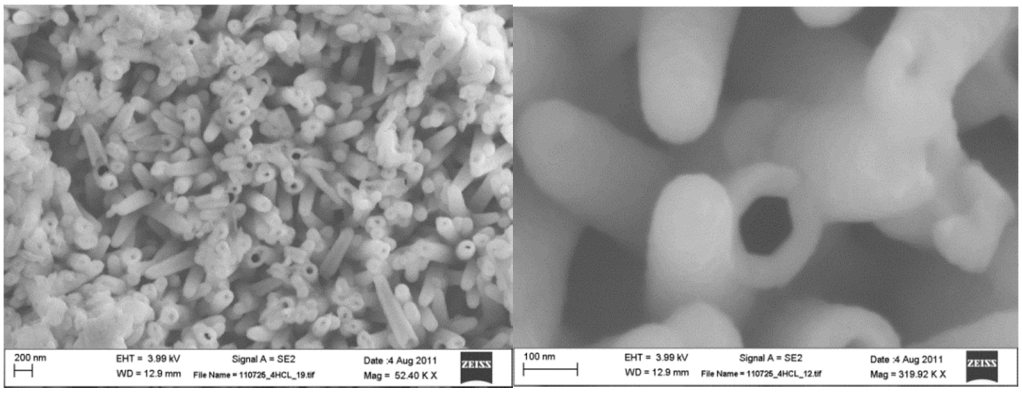

Fig. 4-3-9 Plane view SEM image of e-PT “nano testtubes”

This method was reproducible, with another sample being made at the same potential (Fig. 4-3-10). In Fig. 4-3-10b, the closed end of the nano testtube can be observed in the middle of the image.

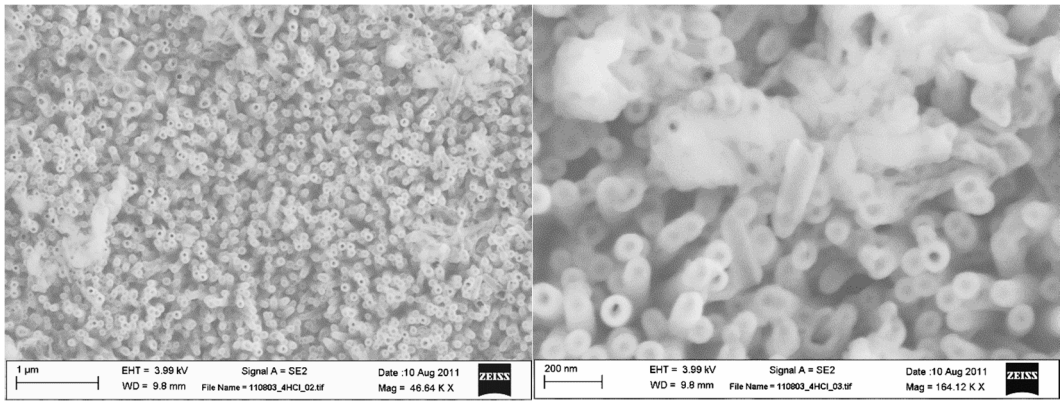

Fig. 4-3-10 Plane view SEM image of e-PT "nano testtubes"

[Portion of this section is adapted with permission from Ref (47). Copyright (2013) American Chemical Society.]

4.4 Energy Level Alignment

In order to optimize hybrid solar cells that incorporate electrodeposited polymers, it is critical to develop a fundamental understanding of energy level alignment at the interface as it has been found to affect organic photovoltaics (OPV) performance.[53] Recent literature studies of the interface between an organic phase (P3HT or PCBM) and an inorganic phase (ZnO) reveal charge transfer phenomena which result in an interface dipole and further establish the dependence of device parameters on the energy level alignment at the interface.[54-56] However, there has been limited study on the energy level alignment at the interface between electrodeposited polymers and inorganic materials. In this work, we use electrodeposited polythiophene (e-PT) and ZnO planar substrates as a model system to study the band offset at the interface and to determine its correlation with model device performance. Although this e-PT/ZnO model device does not represent an efficient OPV, it does serve as an excellent photovoltaic system to help develop a fundamental understanding of energy level alignment and its influence on device parameters.

Electrodeposition is controlled by a variety of factors including temperature, applied potential, total charge, electrolyte, monomer, solvent, the relative position of the electrodes, etc.[57, 58] Previously, we studied the effects of solvent and total charge on the resulting film morphology.[47] In this paper, we examine the effect of the electrolyte on the structural and electronic properties of e-PT films and the energy level alignment at the interface between e-PT and ZnO. In particular, we focus on the electrolyte anion as it was shown to play a determining role on the polymer structure (the electrolyte cation only affects the behavior of polymer films during charge-discharge processes).[59, 60]

The importance of the electrolyte anions is highlighted in the proposed mechanism of electropolymerization (Fig. 4-4-1). Polymerization is initiated by the formation of radical cations from monomers (2,2'-bithiophene), followed by the coupling of two radical cations to form a dimer. The dimer then reacts further and produces the polymer.[23] The anions in the electrolyte solution participate in the reaction by coordinating to the positively charged radical cations forming a so-called "ion pair", reducing the repulsive force experienced between the two radical cations when they approach and thereby facilitating the coupling reaction.[61, 62] This "anion-assisted" polymerization mechanism shows the critical role of anions in determining the extent of polymer conjugation, which prompted our studies of the anion effect on the resulting polymer structural and electronic properties.

The electrolyte anions we chose to study are BF_4^-, PF_6^-, ClO_4^- and $CF_3SO_3^-$ (Fig. 4-4-1). These four anions were selected because they have different sizes, different extent of charge delocalization, and different basicity/electronegativity at the periphery of the anion.[63]

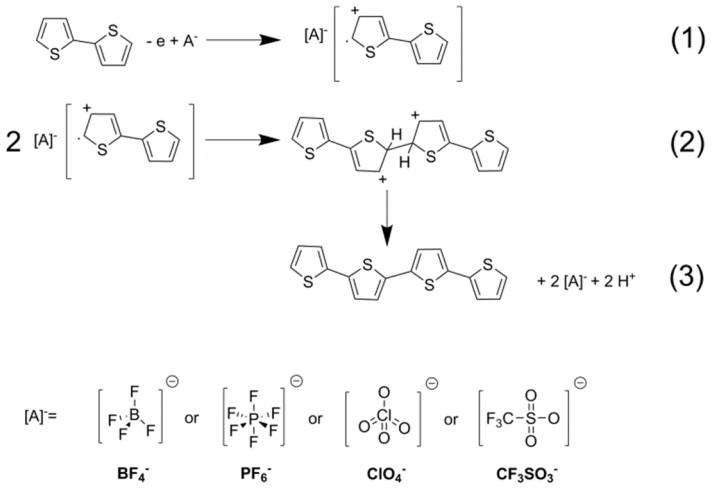

Fig. 4-4-1 Anion-Assisted Electrodeposition Mechanism

Many studies have been carried out to examine the anion effect on the nucleation and growth processes[64], electrochemical[59] and electronic properties[65], electrical conductivity[66], and morphology[67] of the deposited polymer films. However, most of these studies focused on heavily doped "metallic" polymer films, which are not suitable as semiconductive materials in OPV. In our study, semiconducting polymer films with little or no dopant anions were produced to ensure that the dopant effects on the electronic properties were eliminated and that the observed electronic properties were primarily dependent on the polymer structure. We found that the electrolyte anions have a strong influence on the resulting film morphology and energy level alignment at the e-PT/ZnO interface. These effects, in turn, modulate the photovoltaic properties of the system. Such a correlated morphology/electronic/photovoltaic relationship provides an improved understanding for polythiophene/ZnO hybrid solar cells and could serve as a general model for other electropolymerized polymer/inorganic systems.

The chemical composition, optical properties, structural regioregularity and morphology of the electrodeposited neutral polymer films were characterized by X-ray photoemission spectroscopy (XPS), UV-vis absorption, FTIR-ATR and SEM, respectively. Ultraviolet photoemission spectroscopy (UPS) was employed to study the energy level alignment at the interface of e-PT and ZnO, aided by *ab-initio* density of states (DOS) calculations. An interface dipole, defined in this paper as the vacuum level offset between e-PT and ZnO, was observed for certain e-PT/ZnO systems and was found to be largely responsible for improved open circuit voltage (V_{oc}) in model device testing. Cyclic voltammetry (CV) was used as a complementary method for estimation of the ionization potential (IP) values of the e-PT films and compared with results from

UPS measurements. This multi-technique approach enables us to correlate the model device performance (in particular, V_{oc}) with the observed energy level alignment by UPS.

4.4.1 Experimental Methods

Materials. Zinc acetate dihydrate (99%, Aldrich), ethanolamine (99%, Aldrich), 2,2'-bithiophene (98%, TCI America), tetra-n-butylammonium tetrafluoroborate (Bu_4NBF_4, 98%, Oakwood Chemical), tetrabutylammonium hexafluorophosphate (Bu_4NPF_6, 98%, Aldrich), lithium perchlorate ($LiClO_4$, 99%, Alfa Aesar), tetra-n-butylammonium trifluoromethanesulfonate ($Bu_4NCF_3SO_3$, 98%, Alfa Aesar), 2-methoxyethanol (99%, Acros), acetonitrile (anhydrous, 99.8%, Alfa Aesar) were used without further purification. ITO-coated glass slides (MTI Corporation) were subjected to successive 10-minute ultrasonication in dichloromethane and acetone before being blown dried in a stream of nitrogen.

Synthesis of ZnO planar substrates. ZnO films were made by a sol-gel method.[68] A 750 mM zinc acetate solution in 2-methoxyethanol of equal molar ratio of zinc acetate and ethanolamine, was spin-coated at 2500 rpm for 30 seconds. The sol-gel films were annealed on a hot plate in air at 300 °C for 10 min. This sol-gel method afforded ZnO films ~30-40 nm thick.

Electrodeposition and electrochemical analysis. Electrodeposition experiments were carried out with a Princeton Applied Research potentiostat VersaSTAT 3. A three-electrode system was used. The working electrode was the ZnO planar substrate with a surface area of ~1 cm^2 immersed in the solution. The counter electrode was Pt gauze. The

reference electrode was a Ag/Ag^+ non-aqueous reference electrode consisting of a Ag wire immersed in acetonitrile (ACN) solution of 0.01 M $AgNO_3$ and 0.1 M Bu_4NPF_6. All potentials reported in this paper were referenced to this Ag/Ag^+ reference electrode. The electrochemical cell contained ~12 mL solution of 7.5 mM 2,2'-bithiophene and 0.1 M supporting electrolyte in ACN. Before electrodeposition, the solutions were de-oxygenated by bubbling nitrogen through the solution for 10 minutes; a nitrogen overpressure was maintained throughout the experiment. The e-PT films were electrodeposited using the potentiostatic method, which is to keep the potential constant and record the current-time (*I-t*) curves during film growth. The sample was then removed from the solution and rinsed with ACN. The sample was reduced by a standby potential of -1 V (vs. Ag/Ag^+ reference electrode) in a monomer-free electrolyte solution until the current was stable. The sample was again removed from solution and rinsed thoroughly.

For electrochemical analysis, cyclic voltammetry was carried out in a monomer-free electrolyte solution by sweeping the potential from -1 V to 1.3 V, at a rate of 0.05 V/s. The oxidation onset (E_{ox}) was converted to an ionization potential (IP) for the polymer based on the following considerations. Following the IUPAC recommendation of using a ferrocene/ferrocinium (Fc/Fc^+) redox couple in non-aqueous solutions for an internal standard, redox waves of Fc/Fc^+ were measured with 3 mM ferrocene in ACN.[69] The half-wave potential ($E_{1/2}$) was measured to be 0.1 V against Ag/Ag^+ reference electrode. The absolute potential value for Fc/Fc^+ must be established to reference our measured potential values to the vacuum level. Recent experimental and theoretical studies on the absolute potential of Fc/Fc^+ in ACN have determined it to be at 5.0 eV.[70, 71]

Such a value also agrees with earlier results on Fc/Fc^+ in aqueous solution and referencing it to the absolute potential of a standard hydrogen electrode (SHE).[70, 72] Therefore, all E_{ox} values can be converted to the corresponding IP values: IP = e(E_{ox} − 0.1 V + 5.0 V) = e(E_{ox} + 4.9 V).

Model device fabrication and testing. Electrodeposition using 50 mC electrochemical charge produced e-PT films of ~100 nm on ZnO substrates. The top Ag electrode with an electrode area of 0.03 cm^2, was thermally evaporated in vacuum with a base pressure ≤ 1×10^{-6} Torr. Photovoltaic *J-V* characterization was carried out using a HP 4140B pA meter/DC voltage source under AM 1.5 irradiation (100 mW/cm^2) with a 300 W xenon solar simulator. A Labview program was used with the solar simulator and the electrical characterization equipment through which voltages between -1 V and 1 V were delivered to the solar cell with a step size of 10 mV.

Characterization methods. X-ray photoemission spectroscopy (XPS) and ultraviolet photoemission spectroscopy (UPS) measurements were performed on as-loaded samples using a Thermo Scientific ESCALAB 250Xi with a base pressure ≤ 1×10^{-9} Torr. The core level spectra were obtained with an Al-K_α monochromated X-ray source, resulting in a total instrumental broadening of 0.5 eV. The binding energy of the core levels was referenced to the adventitious C 1s peak set at 285.0 eV. UPS valence band spectra were obtained using a helium discharge source resulting in lines at 21.2 eV (He I) and 40.8 eV (He II), with a total instrumental broadening of 0.1 eV. The energy scale of the He II valence band spectra was referenced to the Fermi level of the system and set at 0 eV, measured on a sputter-cleaned Au sample in contact with the films. Work function

measurements were performed using the He I line, with a negative bias of 5 V to the sample to help isolate the secondary electron cutoff of the films.

XPS depth profile by Ar^+ sputtering was performed on a Thermo Scientific K-Alpha system. Beam energy was set to 500 eV at low current, with a raster size of 1.2 mm. Under this condition, the estimated sputter rate (calibrated for Ta_2O_5) is 0.15 nm/s. The etching time per cycle is 100 seconds.

Band edges measurements were performed on ZnO in a separate UHV chamber housing both UPS and inverse photoemission spectroscopy (IPS) with a respective resolution of 0.3 eV and 0.6 eV, with details described elsewhere.[73] Both the valence band and conduction band spectra were referenced to the Fermi level of a sputter-cleaned Au sample in contact with the ZnO sample, and set as 0 eV.

DFT electronic structure calculations of the gas phase molecules were performed with the GAMESS(US) software package[74] using Becke3-Lee-Yang-Parr (B3LYP) hybrid functional.[75-77] Geometries of local minima on the potential energy surface were calculated with a 6-31G basis set either in the C_i or C_{2v} symmetry.[78] The density of states (DOS) was calculated by summing the individual electronic states convoluted with a 0.4 eV full width half maximum Gaussian function.

UV-visible absorption spectra were recorded on a Shimadzu UV-3600 UV-Vis-NIR spectrophotometer. The morphology of e-PT films was visualized by scanning electron microscope (Zeiss Sigma Field Emission SEM, 4 kV acceleration voltage) and helium ion microscope (HIM, Zeiss Orion Plus, 30 kV acceleration voltage, 0.2-0.4 pA beam current). Single attenuated total reflectance infrared (FTIR-ATR) experiments were

performed on a Thermo Electron Corporation Nicolet 6700 FT-IR (ZnSe crystal, the number of spectra averaged is 1024 with a resolution of 4 cm^{-1}).

4.4.2. Results

Electrodeposition of polythiophene and dedoping

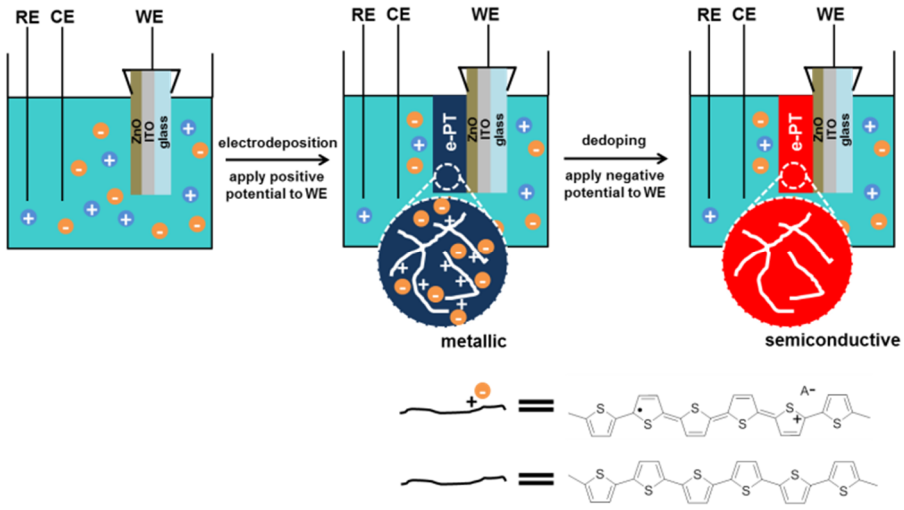

Scheme 4-4-1 Electrodeposition and Dedoping (A^-: Electrolyte Anion).

The general experimental scheme for the paper is illustrated in Scheme 4-4-1. Starting from a working electrode (WE) consisting of a ZnO film deposited on an ITO/glass substrate, electrodeposition was carried out by applying a sufficiently large potential to the WE relative to the reference electrode (RE) in the monomer solution. The as-deposited e-PT polymer chains are positively charged and heavily doped with the electrolyte anions (approximately 1 anion per 5 thiophene units according to our XPS study). Subsequently, this as-grown e-PT film was placed into a monomer-free solution for "dedoping", by applying a negative potential (-1 V) to the WE. This dedoping process removes the electrolyte anions from the as-deposited e-PT films and the resulting

polymer chains are neutral. An electrochromic effect (film color change from dark blue to red, illustrated in Scheme 4-4-1) is associated with this dedoping process. The final polymer material after dedoping is a p-type semiconductor material[79-81], making it suitable for integration into the active layer of our OPV devices.

Electrodeposition of polythiophene was carried out under potentiostatic conditions using 2,2'-bithiophene as the monomer. The potentiostatic method enables real-time electrochemical charge monitoring and thereby accurate control over e-PT film growth. In ideal conditions, the electrochemical charge is directly proportional to the resulting film thickness. The oxidation potential for 2,2'-bithiophene is 0.85-0.90 V, which is 0.7 V lower than that of thiophene,[24] preventing polymer over-oxidation and chain mislinkages at a higher applied potential. To verify polymer structural regularity, FTIR-ATR studies (Fig. 4-4-2) were carried out. The results show that, within instrumental resolution, all films were free of mislinkage (i.e. β-linkages) that may lead to a disruption of polymer conjugation and chain packing.

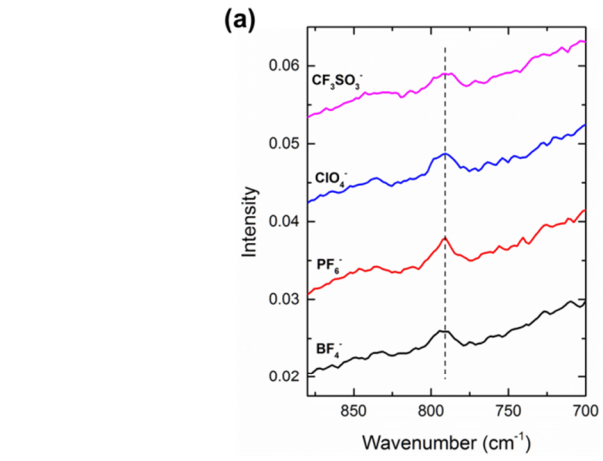

(b)

linkage	structure	wavenumber (cm^{-1})	presence in e-PT films
α-linkage	2,5-disubstituted thiophene	791	Yes
β-linkage	2,4-disubstituted thiophene	730, 820	No

Fig. 4-4-2 (a) FTIR-ATR spectra for on the four undoped polymer films grown on ZnO for a fixed polymerization charge of 50 mC. (b) The corresponding structure, wavenumber and presence in e-PT films of α- and β-linkages.[82]

Four different electrolyte anions were used: BF_4^-, PF_6^-, ClO_4^- and $CF_3SO_3^-$. The minimum potential required to initiate electrodeposition was found to be 0.90 V for all electrolyte solutions, except for ClO_4^- solution in which polymerization could be initiated at a slightly lower potential of 0.85 V. The lowest potential necessary for deposition was applied because higher applied potentials lead to unwanted crosslinking or other side reactions[83] that may degrade the polymer's electronic properties and device performance. *I-t* curves obtained during the polymer growth are shown in Fig. 4-4-3. The electrochemical growth behavior can be generally described as "nucleation and growth":

after a brief initial decrease in current (the induction period), polymeric nuclei begin to form and grow on the ZnO surface, corresponding to a slow continuous increase in current. This is then followed by a more rapid current increase (presumably as the nuclei cover the surface), which eventually slows down during steady state growth. Substantial current variations are measured from polymers produced in solutions containing different anions. Using BF_4^- and $CF_3SO_3^-$ resulted in significantly higher currents than PF_6^-. Growth with ClO_4^- gave rise to the lowest measured current, which is likely due to the slightly lower potential applied.

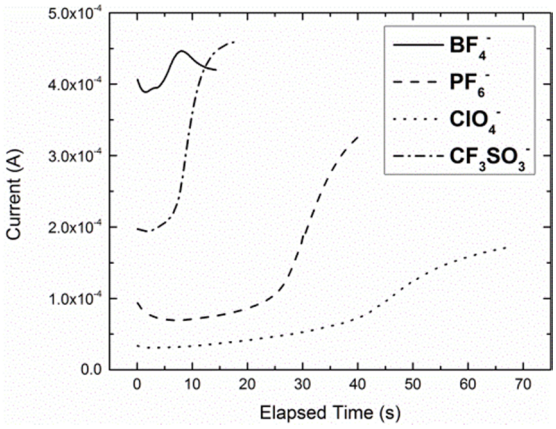

Fig. 4-4-3 *I-t* curves for the potentiostatic electrodeposition of polythiophene onto ZnO films in electrolyte solutions containing various anions: BF_4^-, PF_6^-, ClO_4^- and $CF_3SO_3^-$. The electrochemical charge is fixed at ~5 mC for all samples.

For simplicity and clarity in description, the final state of electrodeposited neutral polymer is referred as the "X^- polymer" (X^- represents the specific electrolyte anion used during electropolymerization). For example, for e-PT film grown in BF_4^- electrolyte solution and then electrochemically reduced to remove the BF_4^- anions, it would be called "BF_4^- polymer".

Chemical composition

XPS studies were carried out to analyze the chemical composition of the neutral polymer films and to examine whether the anion dopants were completely removed.

The C 1s and S 2p core level spectra of the neutral polymers grown with various electrolyte anions are shown in Fig. 4-4-4. A careful comparison of the lineshapes of these core levels can help in characterizing the C and S local environment. The C 1s lineshape can be decomposed into 6 components (binding energy values listed in Table 4-4-1) as indicated in Fig. 3a. The component found around 284.2 eV was assigned to the aromatic α carbon in the thiophene ring,[28] whereas the one at 285.0 eV was assigned to the aromatic β carbon in the thiophene ring with a partial contribution from the adventitious carbon (resulting in an apparent higher intensity for the β carbon peak than the α carbon peak). At higher binding energy, carbon peaks of increasing binding energy at 286.1-286.5, 287.6-287.9, 288.9-289.6 and 290.4-290.7 eV were assigned to environments of increasing oxidation states. The intensities for these oxidized carbon peaks are small, therefore peak fitting (intensity and energy) can only achieve moderate accuracy, and consequently the information content is somewhat limited. Additionally, for conjugated carbon-based structures, a shake-up satellite is anticipated at ~6-7 eV higher binding energy relative to the main carbon peaks,[34] which places the satellite at ~290-292 eV. This region overlaps with that of the highest oxidized carbon states. The polymer synthesized using ClO_4^- displays a higher shake-up intensity, indicating that this specific polymer is likely to have a higher conjugation length than the other polymers.

The S 2p core level spectra measured on the four polymer films are displayed in Fig. 3b. The characteristic lineshape is described by a single spin-orbit doublet, with the

S $2p_{3/2}$ peak centered at 163.9-164.0 eV and assigned to sulfur in neutral thiophene.[84] For comparison purposes, the S 2p core level spectra of heavily anion-doped polythiophene samples typically have two more spin-orbit doublets corresponding to polaronic and multipolaronic states, with the multipolaron state being more significantly manifested as a higher energy tail 2.2 eV away from the neutral thiophene S peak (Supplementary Information Fig. 4-4-5).

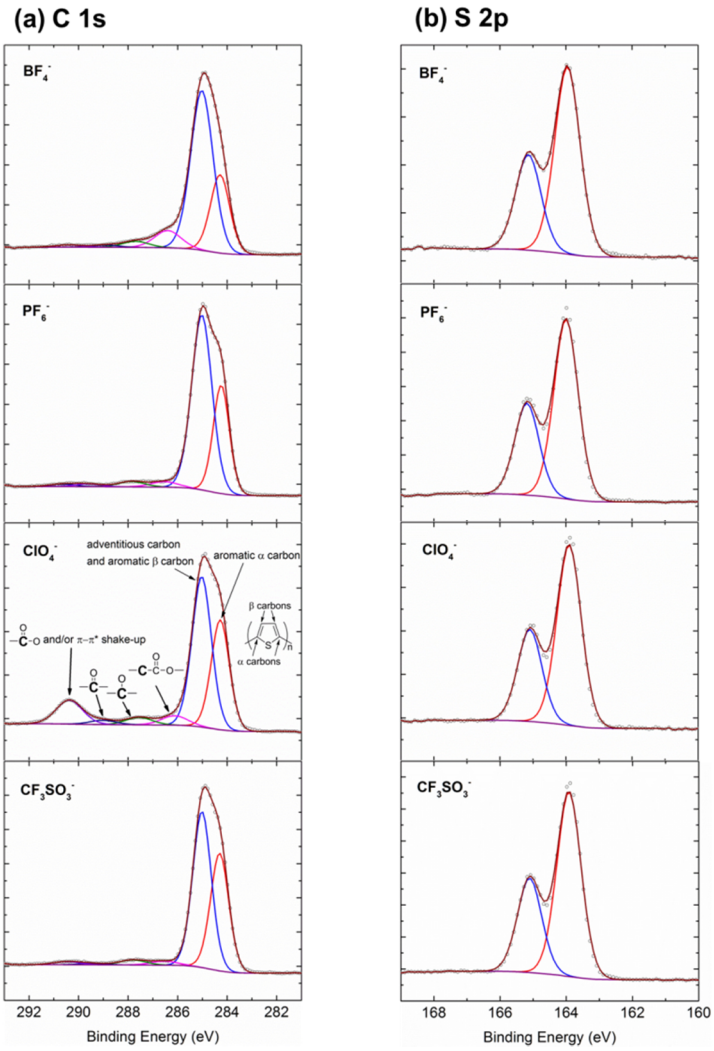

Fig. 4-4-4 (a) C 1s and (b) S 2p core level spectra of neutral polymers grown in the electrolyte solution containing the following anions: BF_4^-, PF_6^-, ClO_4^- and $CF_3SO_3^-$.

Table 4-4-1. XPS C 1s peak energy (in eV) table for neutral polymers grown in the electrolyte solution containing the following anions: BF_4^-, PF_6^-, ClO_4^- and $CF_3SO_3^-$.

	BF_4^-	PF_6^-	ClO_4^-	$CF_3SO_3^-$
α carbon	284.3	284.2	284.3	284.3
β carbon	285.0	285.0	285.0	285.0
C-COO	286.4	286.5	286.1	286.5
C-O	287.7	287.9	287.6	287.8
C=O	288.9	289.6	289.0	289.5
O-**C**=O	290.4	290.7	290.4	290.5

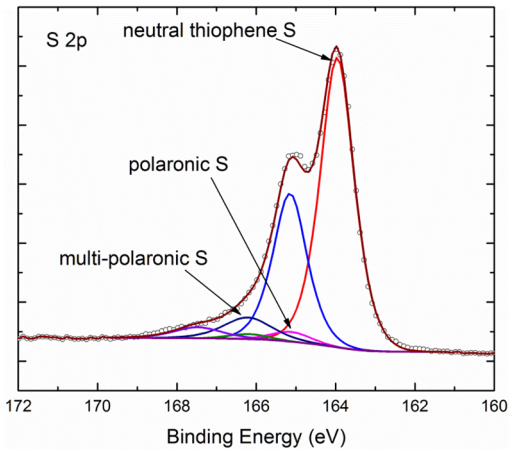

Fig. 4-4-5 XPS S 2p core level spectra of a heavily anion (ClO_4^-)-doped polythiophene on Au, with three spin-orbit doublets corresponding to sulfur from neutral thiophene, polaronic and multi-polaronic state.

For the polymers synthesized in BF_4^-, PF_6^- and $CF_3SO_3^-$, F 1s spectra (Fig. 4-4-6 a-c) are used to quantify the dopant anion concentration within the polymer matrix. Both the polymers synthesized in BF_4^- and PF_6^- contain a signature of F^-, with F 1s peaks centered at 685.0 and 685.1 eV, respectively.[85] An additional F 1s peak is also visible at 687.1 eV for the polymer synthesized using PF_6^-, attributed to PF_6^- or PF_5.[85] For the polymer films synthesized using $CF_3SO_3^-$, no fluorine signal was measured within the detection limit of the XPS system. The unexpected presence of F^- in the polymers synthesized using BF_4^- or PF_6^- indicates that the BF_4^- and PF_6^- anions underwent a dissociation reaction and yielded F^- anions during the electrochemical deposition:[63]

$$BF_4^- \rightarrow BF_3 + F^-$$

$$PF_6^- \rightarrow PF_5 + F^-$$

As such, large and weakly coordinating BF_4^- and PF_6^- anions decomposed and yielded smaller and more strongly coordinating F^- anions. This reaction is present for BF_4^- and PF_6^- anions (but not for $CF_3SO_3^-$) and this must be taken into account when considering the anion effect on polymerization, as will be further explored in the discussion section.

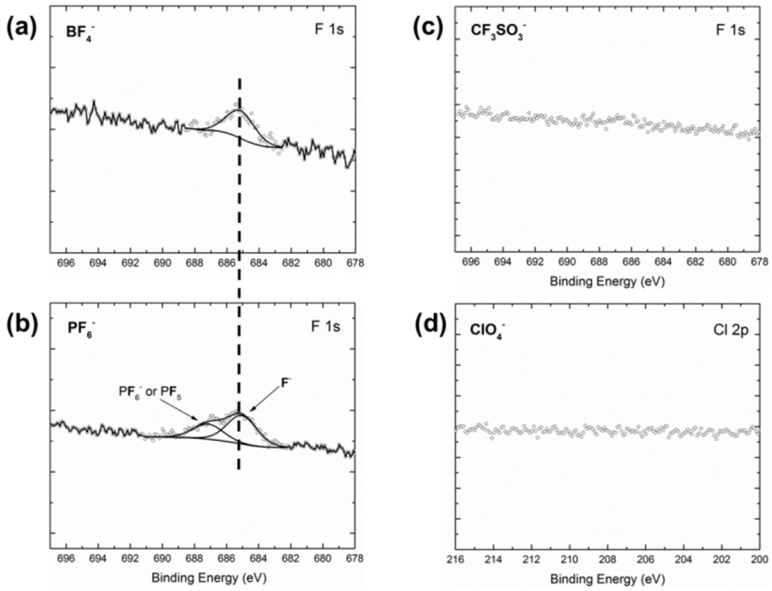

Fig. 4-4-6 F 1s core level spectra of neutral polymers grown in the electrolyte solution containing the following anions: (a) BF_4^-, (b) PF_6^- and (c) $CF_3SO_3^-$. (d) Cl 2p core level spectra of neutral polymers grown in the electrolyte solution containing ClO_4^-.

As sulfur is present in each thiophene unit of the backbone of the polymer, the concentration of dopant anions can be estimated using the atomic ratio of fluorine to sulfur (F:S). The F:S ratio obtained for the polymers is as follows: 2.8% for the BF_4^- polymer and 2.6% at most (considering that the higher binding energy peak is solely of PF_5) for the PF_6^- polymer. These ratio values reflect that in some of the polymers the dopant anion is difficult to be completely removed even upon reduction for a prolonged period of time. However, the extremely low concentration of dopant anion levels will not cause observable changes in the polymer electronic properties such as ionization potential (IP) as measured by UPS (Supplementary Information, Fig. 4-4-7): This is evidenced by the polymer sample with a dopant concentration slightly higher at 3.2%, showing no

significant change in IP compared to a dopant-free sample. Only at a much higher dopant anion level of 17% does the IP show an increase of 0.2 eV.

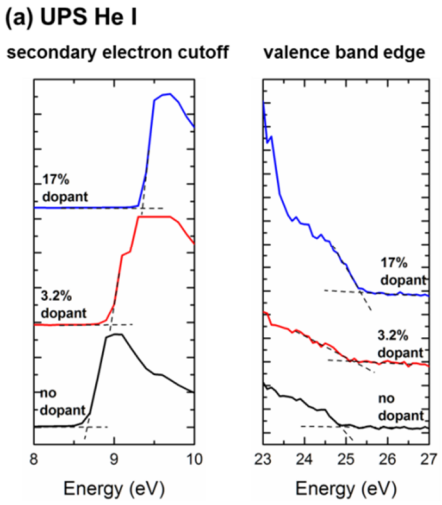

(b) Summary of UPS He I Data

	He I		
	E_{SEC}	E_{VBE}	IP
no dopant	8.7	24.9	5.0
3.2% dopant	9.0	25.2	5.0
17% dopant	9.4	25.4	5.2

Fig. 4-4-7 (a) UPS He I spectra of the secondary electron cutoff and valence band edge of various ClO_4^- dopant level polythiophene films on Au. (b) Summarized Table for E_{SEC}, E_{VBE} and IP (in eV).

Finally, for the ClO_4^- polymer, there is no detectable dopant Cl 2p signal (Fig. 4-4-5d).

To summarize, the four polymer films obtained have no dopant anions left (ClO_4^- and $CF_3SO_3^-$) or have a very low concentration of dopant anions (BF_4^- and PF_6^-) that were found to exert no observable effect on the electronic properties measured by UPS.

Optical properties

UV-visible absorption spectra measured on a clean ZnO film and on the four polymers (in this case with a fixed polymerization charge of 50 mC) are shown in Fig. 4-

4-8. In all spectra, the change in slope observed below ~400 nm leads to a high intensity background; this is attributed to the absorption of glass. Consequently, the ZnO absorption is small relative to the substrate background,[86] but can still be extracted using a proper spline background subtraction. The resulting absorption feature is shown in the inset of Fig. 4-4-8, and an extrapolation of the high-wavelength edge to the background of the spectrum leads to an optical gap of 376 nm (or 3.3 eV), in agreement with the typical value found for sol-gel produced ZnO films.[87] Given the high intensity of the polymers absorption edges, a simple extrapolation of the high-wavelength edge to the background of the spectra leads to an optical band gap of 2.0 eV for all polymers, independent of the anion used during electrodeposition. A similar behavior was previously reported for electrodeposited poly(3,4-ethylenedioxythiophene) (PEDOT) films using various anions in the electrolyte solution.[88]

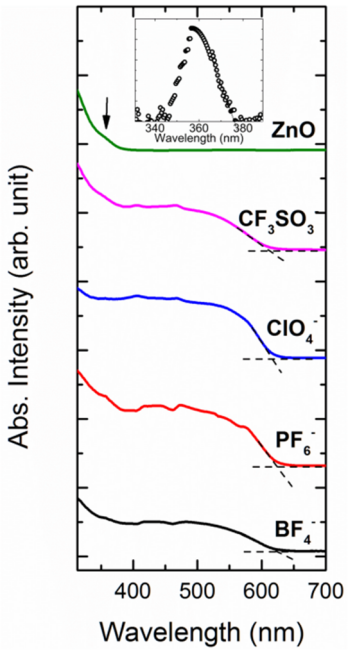

Fig. 4-4-8 UV-vis absorption spectra measured on a clean ZnO film and on the four undoped polymer films grown on ZnO for a fixed polymerization charge of 50 mC. The

arrow points to a small shoulder on the ZnO/ITO/glass sample that is attributed to the absorption from ZnO. After proper background subtraction, a ZnO absorption feature can be extracted and shown in the inset.

Film morphology

In order to better understand the growth mechanism during electrodeposition, a clean ZnO surface and dedoped thin (polymerization charge of 5 mC) and thick (polymerization charge of 50 mC) polymer films were observed using SEM. It should be noted that there was no observable change in surface morphology or thickness before and after the dedoping process (Fig. 4-4-9). This indicates that, when the polymer film is removed from the solution and allowed to dry in air, it undergoes structural relaxation to relieve the stress that it experienced in the volume-expanding solvated state during electropolymerization. Dedoping does not induce noticeable further structural change in these samples.

The starting ZnO film (Fig. 4-4-10 a and b) adopts a relatively porous structure typical of sol-gel produced ZnO films and exhibits wavy surface roughness. The thin films, polymerized with a charge of 5 mC (see Fig. 4-4-11 for cross section), adopt various morphologies on the substrate (as shown in Fig. 4-4-10 c-f), highlighting the effect of anions on polymer growth. There are several distinguishable features: (1) films: relatively continuous conformal layers of polymer; (2) fibers: extended irregular polymer structures resembling ridges or rings; (3) nodular deposits: clusters of loose polymer deposits on top of the thin film. Nodular deposits are present in all films. These features appear brighter in the SEM images because their protrusion causes more severe charge

accumulation than other areas when exposed to the electron beam. They are likely diffusion-limited polymer aggregates.[89] It is thought that increased interactions among the anions, the solvent-swollen polymer and the oligomers, resulted in these insoluble aggregates on the polymer film.[67] They extend away from the polymer film as they grow and are scattered across the entire surface with what appear to be high surface area structures. Fiber deposits (appearing bright in SEM images for the same reason mentioned above for the nodular deposits) were found for the BF_4^- and $CF_3SO_3^-$ polymers, but not the PF_6^- or ClO_4^- ones. The overall surface of the thin BF_4^- and $CF_3SO_3^-$ polymers appear to be continuous, with morphology closely resembling that of the underlying ZnO substrate, and bearing a similar wavy appearance. However, the PF_6^- polymer film is relatively smooth and does not appear to share the same undulating roughness of the underlying ZnO substrate as it does in the other two films. Finally, the ClO_4^- polymer displays a rather open structure (Fig. 4-4-10 e), with noticeably less film compactness than the other three polymers.

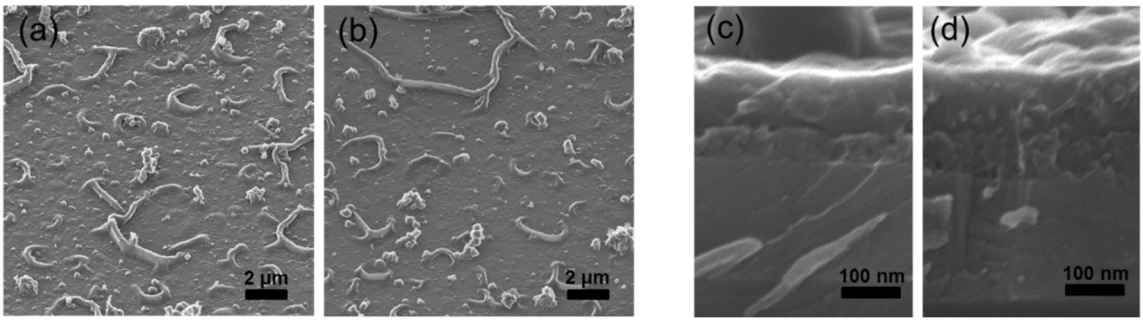

Fig. 4-4-9 45° tilt angle HIM image of (a) doped e-PT film and (b) dedoped e-PT film; cross sectional HIM image of (c) doped e-PT film and (d) dedoped e-PT film. All e-PT films were deposited on ZnO film substrate with ClO_4^- as electrolyte anion. Both films are ~80 nm thick.

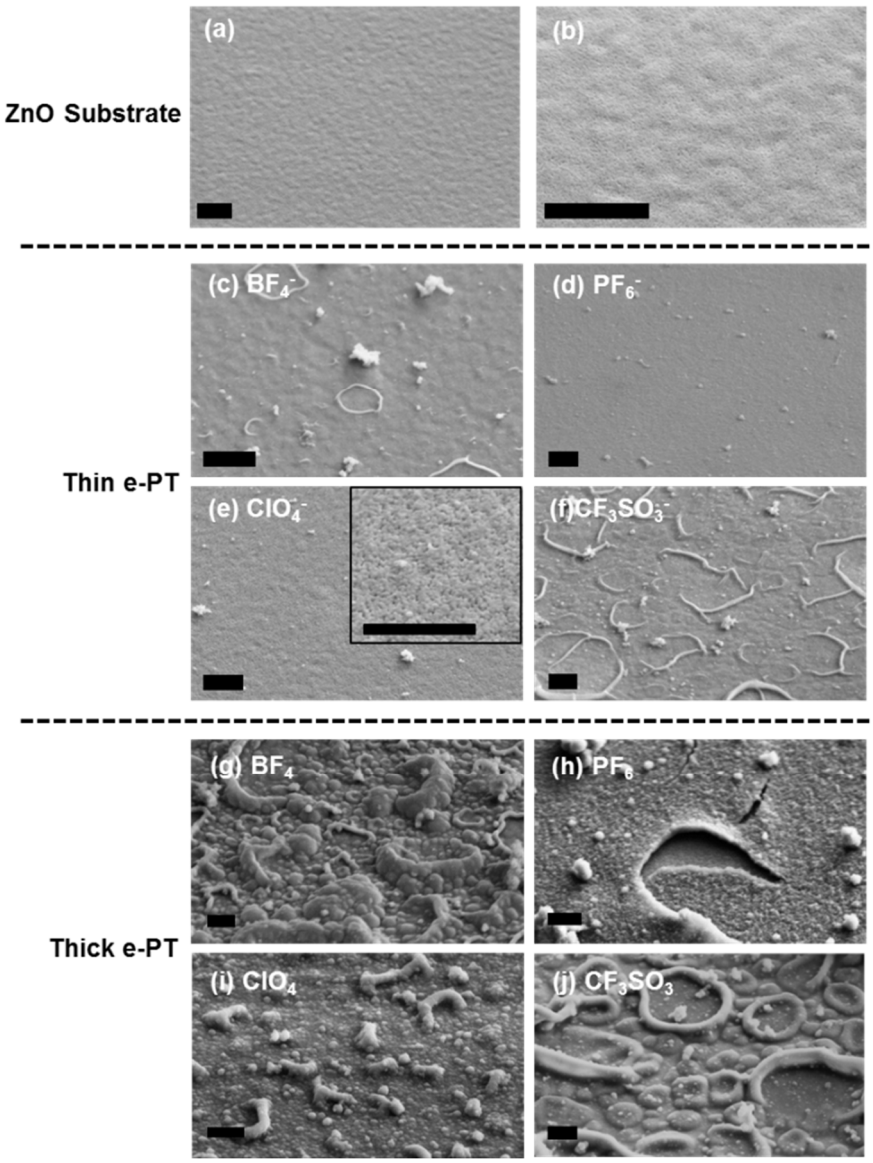

Fig. 4-4-10 Summary of SEM images. (a) ZnO film, (b) Magnified view of ZnO film; thin e-PT films synthesized with 5 mC polymerization charge using the following electrolyte anions: (c) BF_4^-, (e) PF_6^-, (e) ClO_4^- and (f) $CF_3SO_3^-$; thick e-PT films synthesized with 50 mC polymerization charge using the following electrolyte anions: (g) BF_4^-, (h) PF_6^-, (i) ClO_4^- and (j) $CF_3SO_3^-$. All SEM images are taken from a 45° tilt angle. Scale bar = 1 μm.

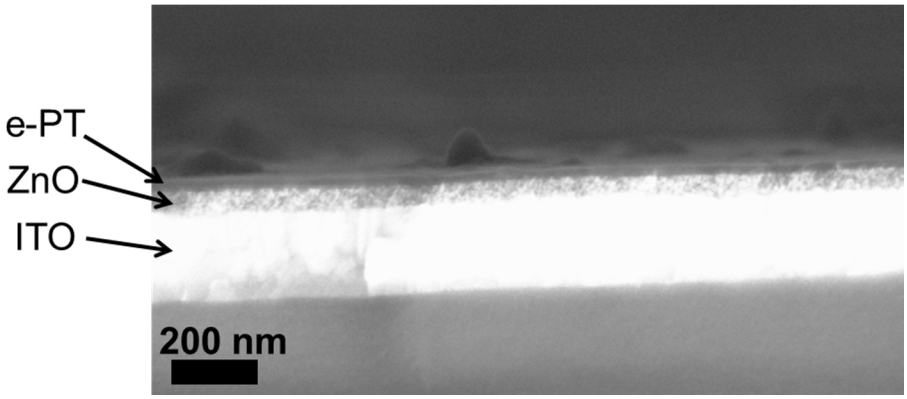

Fig. 4-4-11 Cross sectional SEM image of a thin polymer film (BF_4^-) deposited on ZnO film with a fixed charge of 5 mC. The thin e-PT film is ~10-20 nm.

By increasing the electrochemical charge from 5 mC to 50 mC, much thicker films were produced (~80 nm, see Fig. 4-4-12 for cross section). These thicker films generally show a trend of more pronounced morphological features (Fig. 4-4-10 g-j) as compared to their thinner counterparts. The BF_4^- and $CF_3SO_3^-$ polymers follow a similar growth pathway, where the relatively small number of fiber deposits originally seen in the thin films changed to larger size and greater numbers of fibers or circularly shaped deposits. This translates into higher roughness overall compared to their thinner counterparts. The ClO_4^- polymers become more dense and compact compared to what is observed at the early stage of growth, with similarly fiber-shaped polymer deposits on the film surface but comparatively less rough than the BF_4^- and $CF_3SO_3^-$ polymers. A unique aspect of the PF_6^- polymer is the appearance of morphological defects in the form of extensive cracks on the film surface, presumably because the film cannot withstand the large surface tension experienced from the solvent-swollen state in solution to the dried

state when taken out of the solution and allowed to dry in air. This also demonstrates poor film adhesion of PF_6^- produced polymer films to the ZnO substrate, which has also been observed for the thinner film.

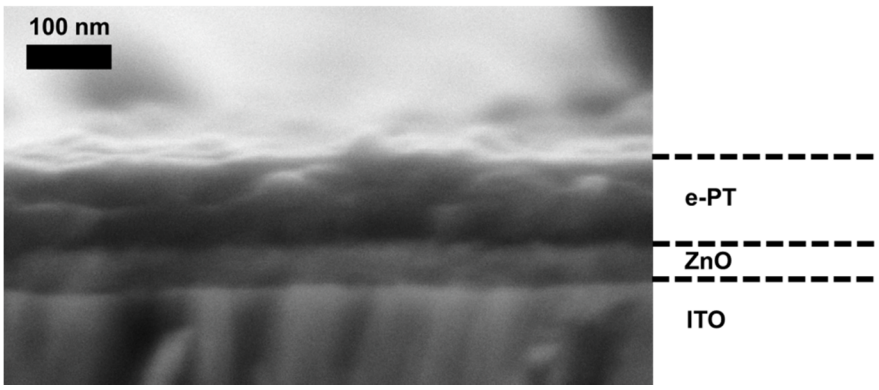

Fig. 4-4-12 Cross sectional SEM image of a thick polymer film ($CF_3SO_3^-$) deposited on ZnO film with a fixed charge of 50 mC. The thick e-PT film is ~80 nm.

Electronic structure at the e-PT/ZnO interface

UPS/IPS studies of ZnO films

The valence bands (VB) and conduction bands (CB) of pristine ZnO films have been probed using UPS and IPS. It should be noted that our UPS measurements have an error bar of ±0.1 eV due to instrumental broadening. Typical VB and CB spectra are shown in Fig. 4-4-13 a. The He II VB spectrum is characterized by a strong signal from the shallow Zn 3d core levels at 11.3 eV, and by well-defined O 2p states ranging from ~4-9 eV. The conduction band of ZnO is typically featureless, due to the low inverse photoemission cross section of the Zn 4s-4p states. As both occupied and unoccupied states are referenced with respect to a common Fermi level, and analyzed in the same

UHV system, an energy gap can be directly extracted from the valence and conduction band edges. Using a linear extrapolation of the leading edge to the background of the spectra, a valence band edge of 3.5 eV and a conduction band edge of -0.1 eV are obtained, defining a 3.6 eV transport gap for the ZnO film.

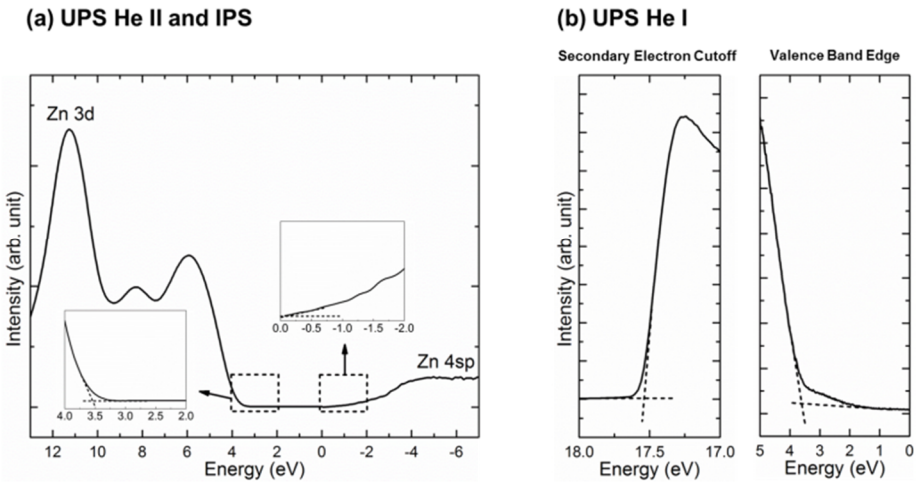

Fig. 4-4-13 (a) Valence (E > 0) and conduction (E < 0) band edge spectra measured on a pristine ZnO film using UPS and IPS, respectively. The spectra are both referenced to the Fermi level of the system (E = 0). The band edges onsets are indicated in the inset. (b) Details of the secondary electron cutoff and valence band edge obtained on the pristine ZnO film.

The UPS He I spectrum of the pristine ZnO surface is shown in Fig. 4-4-13 b. The secondary electron cutoff energy (E_{SEC}) as well as the valence band edge energy (E_{VBE}) are extracted using the same linear extrapolation method mentioned above. From these values, the ionization potential (denoted as IP and defined as the distance from the VBE to the vacuum level) can be calculated using the following equation:

$$IP = h\nu - |E_{SEC} - E_{VBE}| \quad (1)$$

where hν is the incident He I line energy at 21.2 eV, E_{SEC} at 17.5 eV and E_{VBE} at 3.6 eV. Therefore the calculated IP for ZnO is 7.3 eV, similar to literature values.[90]

UPS studies of e-PT films

Before examining the experimental electronic structure obtained from the four polymer films, it is useful to consider the calculated DOS of thiophene and oligothiophenes (restricted to head-to-tail molecular geometries), shown in Fig. 4-4-14 a. As expected, the increasing delocalization of the π system with increasing polymer unit length leads to a progressive reduction of the HOMO-LUMO gap (indicated with dashed lines), along with the development of well-defined molecular band structures. Details of the DOS of a sexithiophene unit (6T) as well as the main orbital character constituting the electronic structure are presented in Fig. 4-4-14 b. In agreement with previous theoretical UPS work,[91] the HOMO found at 4.8 eV is of π(C2p) character, while the HOMO-1 state at 5.5 eV is of π(C2p+S3p) character. Multiple π states are found at higher binding energies, followed by a large band of σ (C2p+S3p) states starting above 8.5 eV. In the unoccupied states, the first four individual molecular orbitals are π*(C2p+S3p), followed by σ*(C2p+S3p).

The experimental UPS He II valence band spectra of the four polymers (grown with a low electrochemical charge of 5 mC to obtain a very thin film such that interface electronic structure information can be extracted, see Fig. 4-4-11) are displayed in Fig. 4-4-15. Although the average chain length of the polymer is unknown, a comparison of the

experimental valence band spectra to the density of states (DOS) of a 6T unit proves to be insightful. The calculated DOS for a 6T unit has thus been added below the experimental valence band spectra, rigidly shifted in energy so as to align obvious experimental and theoretical features. The valence band features measured on the BF_4^-, PF_6^- and $CF_3SO_3^-$ synthesized polymers resemble the calculated DOS, modulated by the appearance of states characteristic of ZnO around 5 and 11 eV. In the case of the ClO_4^- polymer, the contribution of the underlying ZnO is more prominent, consistent with SEM observations (Fig. 4-4-10 e). Thus the experimental VB of the four polymers can be described as follow: at energies below 5 eV we found strong π(S3p+C2p) states, followed by σ(C2p+S3p) states at energies greater than 5 eV. The feature around 2 eV, corresponding to the HOMO/HOMO-1 region in the simulated DOS, appears experimentally as either a broad or a double-peaked structure. The peak separation is particularly clear on the VB spectrum of the PF_6^- polymer where the peaks are clearly visible at 2.1 eV and 2.8 eV. The separation of the HOMO and HOMO-1 levels, as indicated in Fig. 8b, could be a useful metric in understanding the electronic structure of the polythiophene films.

Careful examination of the features at 1-4 eV in the theoretical simulation of thiophene (T) to decathiophene (10T), shows that the double peak first arises for tetrathiophene (4T) with a separation of a relatively large 1.0 eV. The separation narrows gradually to 0.7 eV for sexithiophene (6T). This double peak feature broadens and effectively disappears after 6T. Correlating experimental intensities at this region with theoretical simulations, we can gain insight on an important polymer physics property - the mean conjugation length (MCL), for select polymer films which have a well-resolved double peak feature, such as the one observed in the PF_6^- polymer spectrum. The MCL of

electrodeposited polymers was found to be difficult to extract due to the insolubility of these polymers. Earlier indirect evidence based on conductivity values for short chain oligomers or Raman and IR studies points to an MCL of 6-12 thiophene units for electrodeposited polythiophene with thiophene as the monomer.[57] Using the dimer 2,2'-bithiophene as the monomer is known to lead to a decrease in MCL compared to using thiophene, due to the lower reactivity of the dimer and the decreased stereoselectivity of the polymerization.[57] This should lower the MCL for our polymers films to fewer than 6-12 thiophene units. For the PF_6^- polymer, the double-peak feature is actually visible and therefore we can infer that the MCL is ~6 thiophene units for this particular polymer. This MCL value is reasonable considering the estimation of MCL to be fewer than 6-12 thiophene units based on the discussion above. For the other polymers which lack this double peak feature and appear relatively broad at this region, the identification can be challenging because this feature could be either related to the polymeric structure itself or possible broadening effects. In summary, UPS He II spectra can be applied to identify the MCL which is otherwise difficult to directly extract with other techniques.

Having established the nature of the valence band states for the polymer films, the HOMO onset can be extracted from the He II VB spectra of Fig. 4-4-16. The E_{VBE}, defined as the energy separation between the HOMO edge and the Fermi level, is reported in Table 4-4-2 for each polymer. The IP values for the polymers can also be extracted from the He I VB spectra measured on films biased at -5 V. The IP, defined as the energy difference between the vacuum level and the HOMO onset, is obtained analogous to how it was obtained for ZnO, using the E_{SEC} and E_{VBE} values from UPS He I and Equation (1). The extrapolation procedure for the relevant energy edges was

displayed in Fig. 4-4-16 and the calculated IP values for the polymers prepared in various electrolyte solutions are tabulated in Table 4-4-2. The range of IP values (5.1-5.4 eV) was found to be similar to that obtained by a complementary technique, cyclic voltammetry (4.9-5.2 eV, Fig. 4-4-17). From the IP and E_{VBE} values, we have also calculated the energy separation between the Fermi level and the vacuum level (E_F to E_v) by subtracting E_{VBE} from IP.

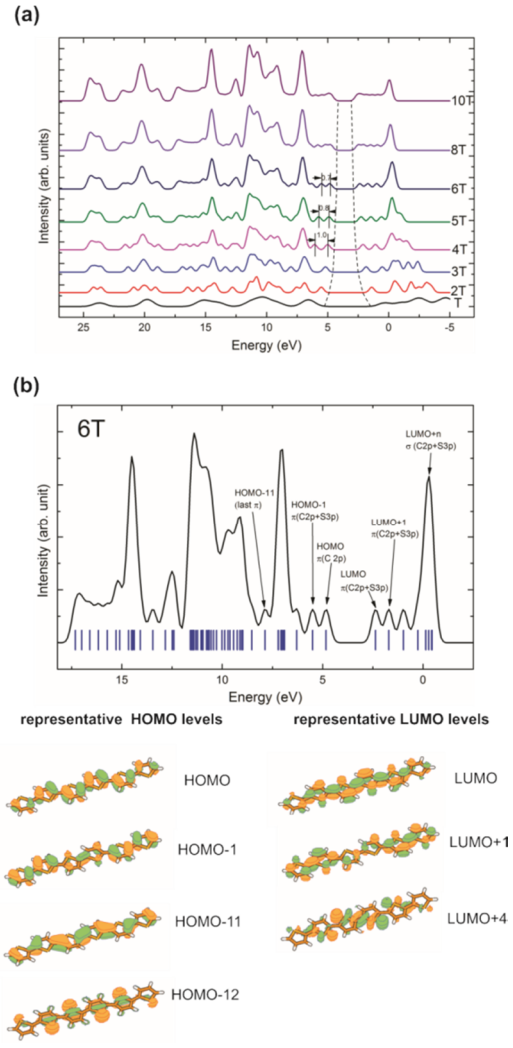

Fig. 4-4-14 (a) Calculated DOS spectra of thiophene (T) and oligothiophenes (2T-10T). (b) Assignment and contour plots of representative HOMO and LUMO levels for sexithiophene (6T).

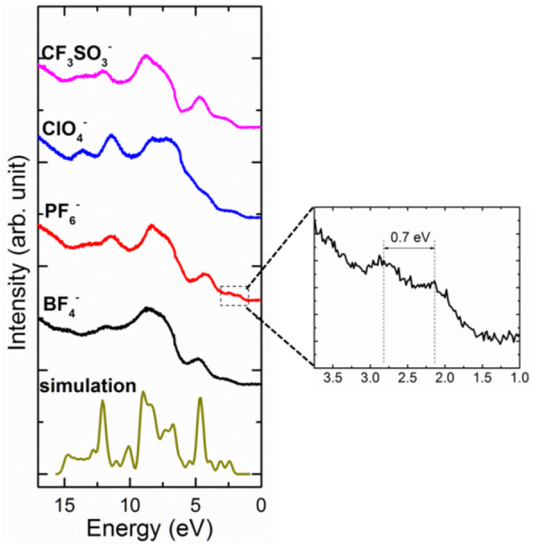

Fig. 4-4-15 Experimental UPS spectra of neutral polymer films synthesized using the following electrolyte anions: BF_4^-, PF_6^-, ClO_4^- and $CF_3SO_3^-$. The calculated DOS spectrum for sexithiophene (6T) is presented for comparison.

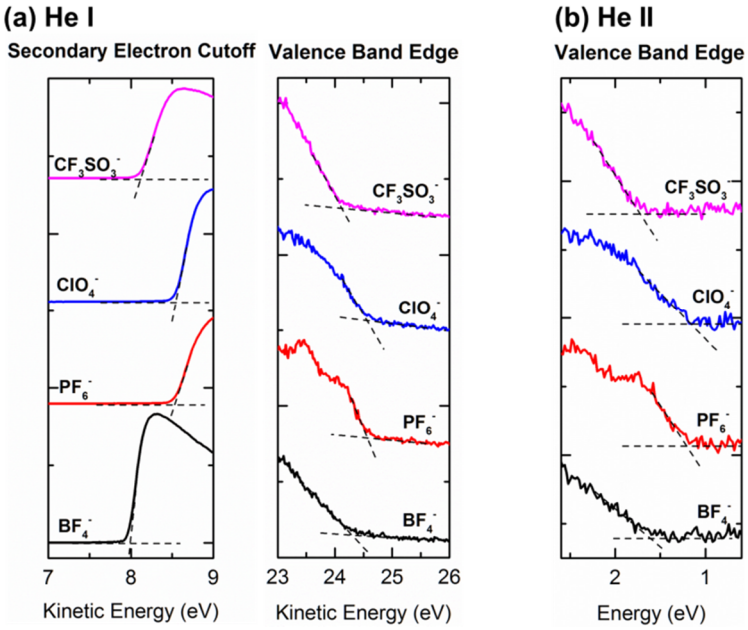

Fig. 4-4-16 Experimental UPS (a) He I spectra of the secondary electron cutoff and valence band edges; (b) He II spectra of the valence band edge.

TABLE 4-4-2. Summary of UPS Data

	He I			He II	
	E_{SEC} (KE)	E_{VBE} (KE)	IP	E_{VBE}	E_F to E_v
BF_4^- Polymer	8.0	24.3	4.9	1.6	3.3
PF_6^- Polymer	8.5	24.6	5.1	1.2	3.9
ClO_4^- Polymer	8.5	24.6	5.1	1.2	3.9
$CF_3SO_3^-$ Polymer	8.1	24.1	5.2	1.7	3.5

SEC: secondary electron cutoff; VBE: valence band edge; IP: ionization potential; E_F: Fermi level; E_v: vacuum level. KE: kinetic energy

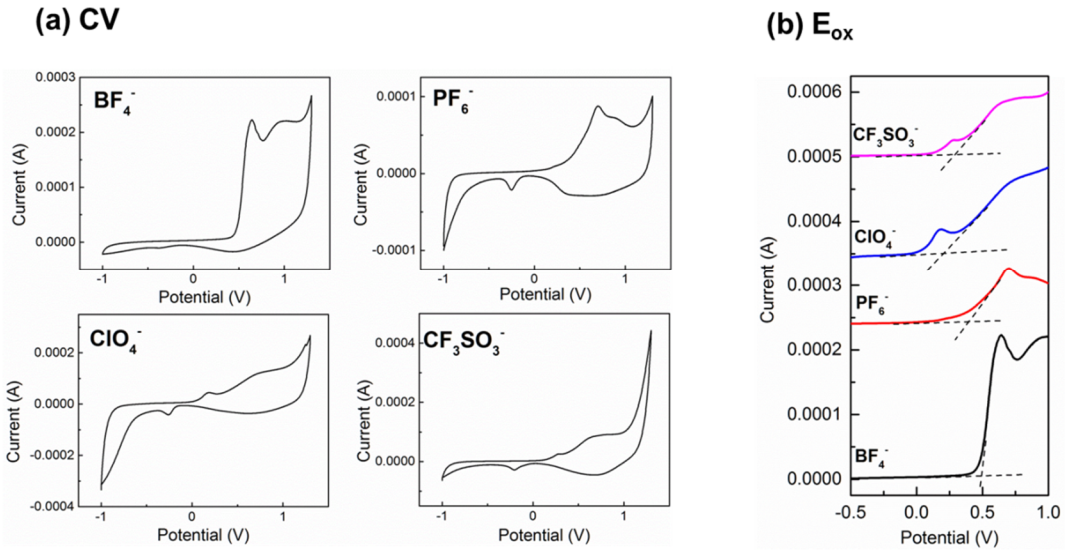

Fig. 4-4-17 (a) Cyclic voltammograms for polymers grown in electrolyte solutions containing the following anions: BF_4^-, PF_6^-, ClO_4^- and $CF_3SO_3^-$. (b) Magnified view of the potential region between -0.5 V to 1.0 V and corresponding E_{ox} values (0.5, 0.4, 0.2, 0.3 V) by extrapolation of leading edges. From IP = e(E_{ox} + 4.9 V), E_{ox} is thus converted to corresponding IP values of 5.4, 5.3, 5.1, 5.2 eV for BF_4^-, PF_6^-, ClO_4^-, $CF_3SO_3^-$ polymers, respectively. Note: The 0.19 V peak has been attributed to the presence of more regioregular polymer domains.[92] The ClO_4^- polymer, with the most prominent 0.19

V peak, appears to have the highest fraction of regioregular domains and exhibits higher order within the polymer chains. This finding was also reflected in our XPS studies in the paper.

Photovoltaic testing of model device

Photovoltaic devices (Ag/e-PT/ZnO/ITO) were fabricated with without thermal annealing (Fig. 4-4-18). The e-PT films were electrodeposited for a fixed charge of 50 mC to obtain a polymer layer of ~80 nm thick with a complete coverage over the ZnO substrate to prevent device shorting. Due to the PF_6^- polymer film exhibiting stress failure cracks across the substrate (Fig. 4-4-10h), the PF_6^- devices often shorted, as the underlying ZnO is partially exposed during Ag electrode deposition. The other three polymer films (BF_4^-, ClO_4^- and $CF_3SO_3^-$), however, had no such morphological defects and were successfully fabricated into solar cell devices. The resultant device parameters (J_{sc}, V_{oc}, FF and η) are displayed in Table 4-4-3.

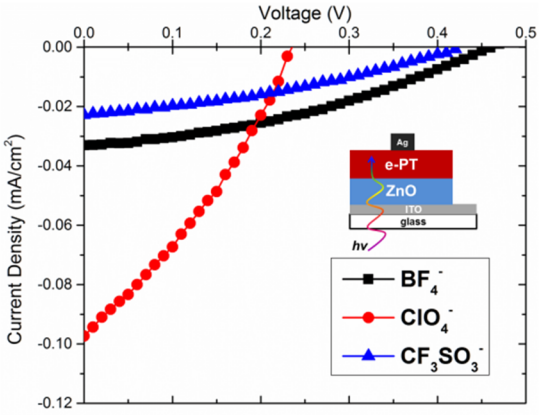

Fig. 4-4-18 Photovoltaic testing of e-PT/ZnO hybrid solar cells, of which the e-PT was synthesized using BF_4^-, ClO_4^- and $CF_3SO_3^-$ anions.

TABLE 4-4-3. Summary of Photovoltaic Properties

Device	J_{sc} (mA/cm^2)	**V_{oc} (V)**	FF	η
BF_4^-	0.033	**0.47**	0.36	0.0057%
ClO_4^-	0.097	**0.24**	0.31	0.0073%
$CF_3SO_3^-$	0.023	**0.43**	0.34	0.0033%

For comparison, planar bilayer photovoltaic device which incorporates a commonly used and chemically synthesized conductive polymer, regioregular-P3HT (rr-P3HT) spin coated onto ZnO film, yielded J_{sc} of 0.25 mA/cm^2, V_{oc} of 0.30 V, FF of 0.38 and η of 0.029%. The main difference between rr-P3HT/ZnO and e-PT/ZnO devices is J_{sc}, which could be due to a number of factors, such as different optical absorption, film porosity and/or carrier mobility. We would like to emphasize that although our e-PT is not a high performing polymeric material, it is studied as a model to help us understand the relationship between the interfacial energy level alignment and device parameters, and to shed light on OPV design rules with an emphasis on the critical interface between the two phases.

Among the working photovoltaic devices, the ClO_4^- device shows a significantly higher J_{sc} of 0.097 mA/cm^2 than the other two devices. This is most likely due to the higher conjugation length and packing order within this polymer. It could also be related to a number of factors, such as different optical absorption, film porosity and/or carrier mobility. This finding was found to correlate with results from our XPS (Fig. 4-4-4) and CV studies (Fig. 4-4-17), both of which indicated higher regioregularity for the ClO_4^- polymer. Although the V_{oc} of the ClO_4^- device is lower than the other two polymers, it still has the best device efficiency thanks to a much superior J_{sc}.

The V_{oc} values for the BF_4^- and $CF_3SO_3^-$ devices, are 0.47 and 0.43 V, respectively (Table 4-4-3). These V_{oc} values are comparable with those observed for typical PT/ZnO hybrid solar cells.[93] The ClO_4^- device shows a lower V_{oc} of 0.24 V (Table 4-4-3), which is ~0.2 V lower than the other two hybrid devices. The difference between the actual V_{oc} values of these devices likely originates from the interfacial energy level alignment and is discussed further in the following discussion section.

4.4.3 Discussion

Based on the polymerization mechanism outlined in the introduction, the coordinating ability of the anions (BF_4^-, PF_6^-, ClO_4^- and $CF_3SO_3^-$) to the positively charged monomeric and oligomeric thiophene species in the solution is thought to regulate the extent of conjugation. Both molecular volume of the anion and the basicity of the peripheral atoms within the anion, were found to affect its coordinating ability.[63] A larger anion has a more delocalized charge distribution and thus a weaker coordinating ability. In addition, anions with fluorine atoms at the periphery should be more weakly coordinating than those with more accessible oxygen atoms: studies have shown that BF_4^- or PF_6^- have weaker coordinating ability than ClO_4^- or $CF_3SO_3^-$.[63]

As for BF_4^- and PF_6^- anions, the molecular volumes were found to be 53.4 and 73.0 $Å^3$, respectively.[94] If the molecular volume was the sole determining factor for coordinating ability, PF_6^- should have the weaker coordination ability of the two. However, the discrepancy in coordinating ability of these two anions in the literature point to other contributing factors such as the Lewis acid character of the boron atom and the variation in coordination to different molecular systems.[95-98] To complicate matters

further, large and weakly coordinating anions can dissociate into smaller and more strongly coordinating anions. In our experiments, PF_6^- and BF_4^- decompose into F^-, further complicating the analysis of the results. Based on the above considerations, it is not entirely straightforward to decouple the coordinating ability of the anions from the resulting polymer conjugation process.

Despite the complexity of the anion effect, we are still able to find a reasonable correlation between the polymer morphology, interfacial energy level alignment, and the photovoltaic properties of e-PT/ZnO hybrid solar cells. From UPS measurements on a clean ZnO substrate and four polymer thin films, together with the optical bandgap information for the polymers, a diagram representing the energy level alignment at the ZnO-polymer interface can be constructed (Fig. 4-4-19). The interface dipole (Δ), is defined as the vacuum level offset between e-PT and ZnO substrate. A negative Δ value means that the e-PT vacuum level is lower than the ZnO vacuum level, whereas a positive Δ value indicates the opposite.

The IP (HOMO to vacuum level) values by UPS are 4.9, 5.1, 5.1, 5.2 eV for BF_4^-, PF_6^-, ClO_4^- and $CF_3SO_3^-$ polymers, respectively. Considering the instrumental resolution ($\pm$0.1 eV), the measured IP values can be considered to be relatively close in range. It is therefore the interface dipole that is causing a more pronounced difference in the energy separation between the polymer HOMO and the ZnO valence band, which represents the theoretical V_{oc} of these e-PT/ZnO hybrid solar cells. The interface dipole in effect "pushed" the HOMO levels of the BF_4^- and $CF_3SO_3^-$ polymers down by 0.5 eV and 0.3 eV, respectively, while the absence of such an interface dipole (the small value of +0.1 eV is within the experimental error) for PF_6^- and ClO_4^- polymers did not change the

HOMO levels for these two polymers. This leads to a larger theoretical V_{oc} for BF_4^- and $CF_3SO_3^-$ devices compared to the other devices.

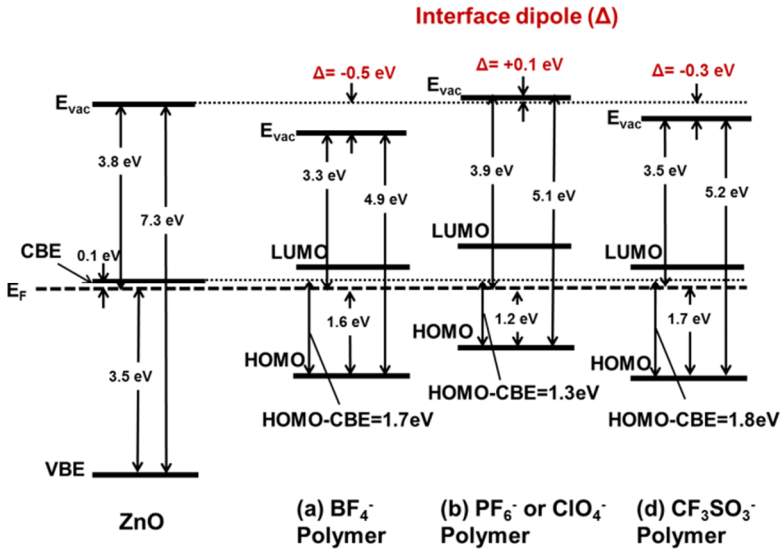

Fig. 4-4-19 Energy level alignment at the interface of ZnO and neutral e-PT polymer film synthesized in electrolyte solutions containing BF_4^-, PF_6^-, ClO_4^- or $CF_3SO_3^-$ (the PF_6^- and ClO_4^- polymers have similar energy levels).

The existence of such an interface dipole likely stems from the interaction between the polymer films and the underlying ZnO substrate. The interface dipole can be explained by an integer charge-transfer model.[99] The dipole is created by charge transfer at the interface, with electronic charges usually transferred from the polymer to ZnO producing a positively charged polymer and a negatively charged ZnO. Such an interface dipole downshifts the polymer vacuum level with respect to the ZnO vacuum level. Interface dipoles between the organic and inorganic phase (similar to our polythiophene/ZnO system) has also been observed by others.[54-56, 100] Recent work shows that the interfacial dipole moment (both its intensity and direction) affects V_{oc}.[101]

It should be noted that we have also investigated the dopant concentration at the e-PT/ZnO interface, which represents another possible factor that may influence the energy level alignment at the interface. From the XPS depth profile (Fig. 4-4-20), there is no obvious residual anion dopant gradient detected from the surface of a thick e-PT film to the interface of e-PT/ZnO. Therefore, the possibility of the dopant concentration as a contributor to the interface dipole is ruled out.

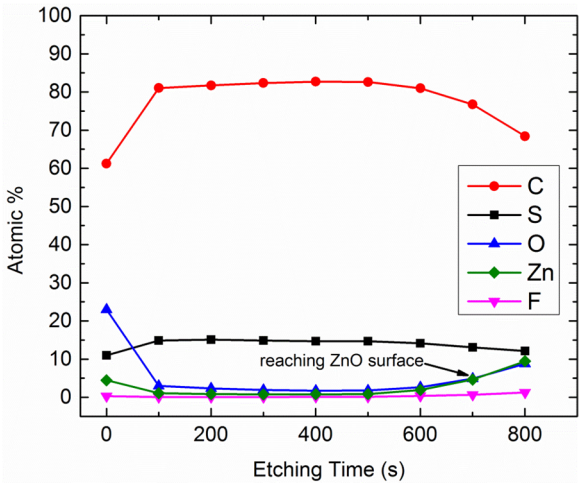

Fig. 4-4-20 XPS depth profile of a thick polymer film (BF_4^-) deposited on ZnO film with a fixed charge of 50 mC. At etching time ~700 s, Zn and O intensity (from ZnO film) increased significantly, indicating that the sputtering has reached the e-PT/ZnO interface. The F intensity from the dopant anion remained extremely low throughout the bulk of the e-PT film to the interface of e-PT/ZnO.

Photovoltaic studies showed that BF_4^- and $CF_3SO_3^-$ devices have V_{oc} values that are about 0.2 V higher than those for ClO_4^- devices. In comparison, as discussed above, the interfacial energy level alignment determines that the theoretical V_{oc} values for BF_4^- and $CF_3SO_3^-$ devices are 0.4-0.5 eV higher than that for the ClO_4^- device. Various loss

processes lead to less pronounced differences between theoretical and actual V_{oc} values.[93] From the studies of theoretical and actual V_{oc} values of these model devices, we have demonstrated correlation between energy level alignment at the interface and the device V_{oc}, and further confirmed the commonly accepted origin of the theoretical V_{oc}: relative band offsets of the two phases.

4.4.4. Conclusions

We have studied the effect of electrolyte anions on the structure of electrodeposited neutral polythiophene films on planar ZnO substrates, and on the energy level alignment at the polymer/ZnO interface. The origin of the anion effect arises from its coordination with the relevant radical cations before the species undergo coupling reactions and form longer conjugation units. Our XPS studies have identified dissociation reactions under our electrochemical conditions, wherein F^- anions were produced and were presumably more strongly coordinating than the larger anions BF_4^- and PF_6^-. This scenario complicates a direct comparison of coordinating ability among these four anions based on coordination rules for weakly coordinating anions.

Although the difference in the IP values for all relevant polymers remains small (0.2-0.3 eV), the interface dipole (energy offset in the vacuum levels between e-PT and ZnO) "pushed" the HOMO levels of the polymer down in two (BF_4^- and $CF_3SO_3^-$) of the four polymers, and resulted in a larger difference of 0.4-0.5 eV between the polymer HOMO level and ZnO CB. This latter observation is directly related to the photovoltaic properties of e-PT/ZnO hybrid solar cells as it represents the theoretical V_{oc}. The establishment of a correlation between the theoretical and actual V_{oc} values, further

validates the model that V_{oc} is determined by the relative band alignment at the interface. Although the device efficiencies are relatively low, our fundamental studies using e-PT/ZnO as model photovoltaic systems have demonstrated the role of interface dipole in regulating solar cell properties, especially by controlling the V_{oc}.

[Portion of this section is adapted from Ref (102) with permission from The Royal Society of Chemistry.]

4.5 Device Testing

The home-made PV device testing platform (Fig. 4-5-1) has two probes situated on the two magnetic "wings". Each probe is equipped with a tungsten tip. During measurement, the two tips are lowered such that they eventually make contact with the respective electrodes.

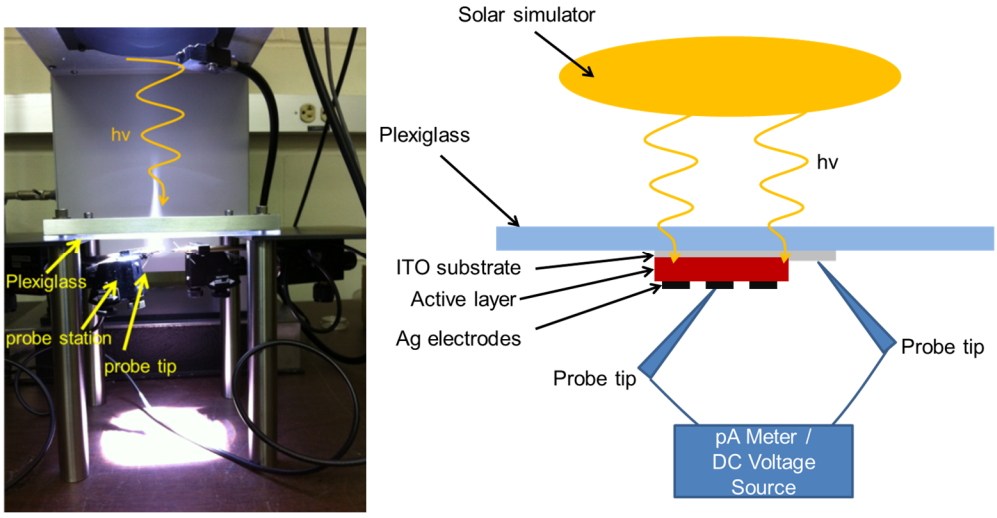

Fig. 4-5-1 PV device testing platform (left) with schematic illustration (right).

4.5.1 Calibration of Device Testing System

4.5.1.1 Silicon Reference Solar Cell

Our PV light source and system was calibrated using a standard silicon reference solar cell (Fig. 4-5-2) in collaboration with Jilin University in China. They have a very active program and have cross-calibrated their systems many times.

Fig. 4-5-2 Silicon reference solar cell

The silicon reference solar cell has an area of 1 cm^2 silicon encapsulated with two wires for connection to the pA meter/voltage source. Note that the probe station was not used in this testing. By not using the probe station, we can avoid intensity loss from the Plexiglass support, and we are able to quantitatively compare the *I-V* curve obtained at Rutgers University with that obtained at Jilin University (Fig. 4-5-3), itself multiply calibrated with commercial reference cells. The I_{sc} using our light source recorded a value that was ~12% lower than that recorded at Jilin University for the same reference sample, while the other parameters such as the V_{oc} and FF remained the same.

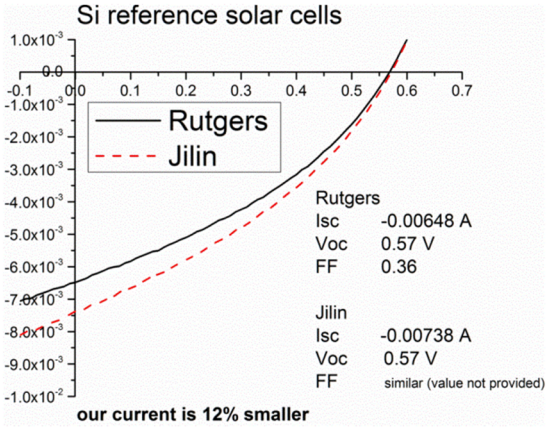

Fig. 4-5-3 *I-V* curves of silicon reference solar cell measured at Rutgers and Jilin University

In order to determine the exact irradiation intensity loss from absorption/reflection by the Plexiglass, we carried out testing of the silicon reference solar cell with and without the solar simulator irradiation going through the Plexiglass. This is achieved by simply placing the silicon solar cell on top of the Plexiglass (without interference) or below the Plexiglass (with interference). There is a 12% decrease in I_{sc} when the irradiation goes through the Plexiglass (Fig. 4-5-4). This amount of decrease is verified by earlier examinations of irradiation intensity with a power meter above and beneath the Plexiglass. The power meter reads 0.54 W on top of the Plexiglass, but only 0.47 W beneath the Plexiglass. It indicates a 13% loss by the Plexiglass, which is similar to the 12% loss inferred from our *I-V* testing (this is different from the 12% loss due to the light source).

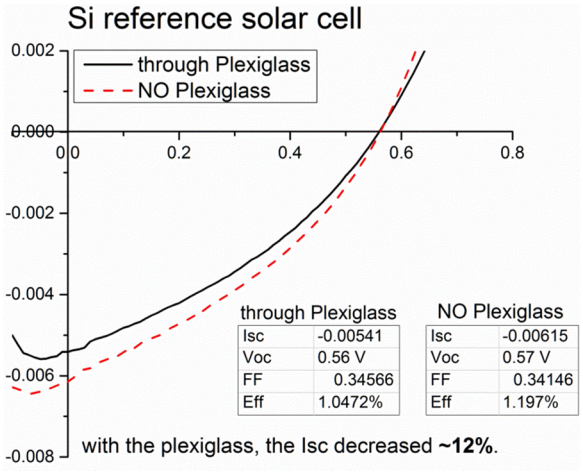

Fig. 4-5-4 *I-V* curve of silicon reference solar cell with and without irradiation going through the Plexiglass.

4.5.1.2 P3HT:PCBM

P3HT:PCBM is one of the most common organic solar cell materials combinations studied in the community, therefore it is fitting to use it to calibrate our system for organic/hybrid solar cell testing. Comparing the *I-V* curves obtained at Rutgers and Jilin University, there is a distinct difference in I_{sc} but almost identical in FF and V_{oc} (Fig. 4-5-5). Our testing was done immediately before we sent the sample to China for testing. There is a delay of several days due to the transit time between our testing and theirs. However, this time period should not cause degradation in the devices, as we have verified that there is almost no device degradation for a longer period of 20 days (Fig. 4-5-6), from the day we first received the sample (day 0) to just before we sent it back to Jilin University for testing (day 20). The well-encapsulated solar cell with plastic cover slips, retained the efficiency quite satisfactorily.

The fact that V_{oc} and FF are similar but I_{sc} appears to be smaller in our testing compared to Jilin's, points to possible current loss phenomena in our probe station. The electrical connection between the probe tips and the electrical measurement unit was suspected and tested, with no sign of bad connections (Fig. 4-5-7). We have not definitely identified the source of the current drop as of now. Therefore, before we can verify our efficiency numbers with a third institution, all reported efficiency data are the original data measured without any adjustment.

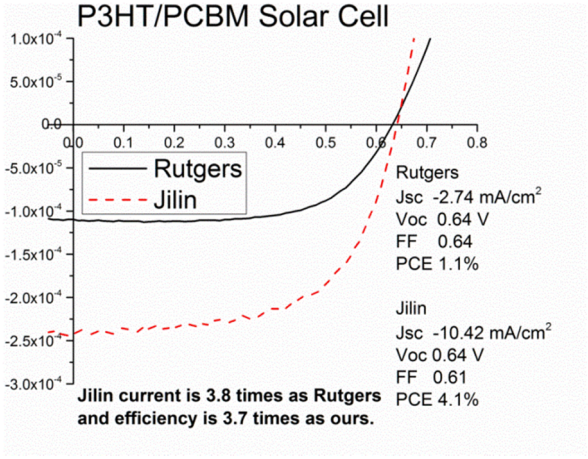

Fig. 4-5-5 *I-V* curve of P3HT/PCBM solar cell, measured at Rutgers and Jilin University

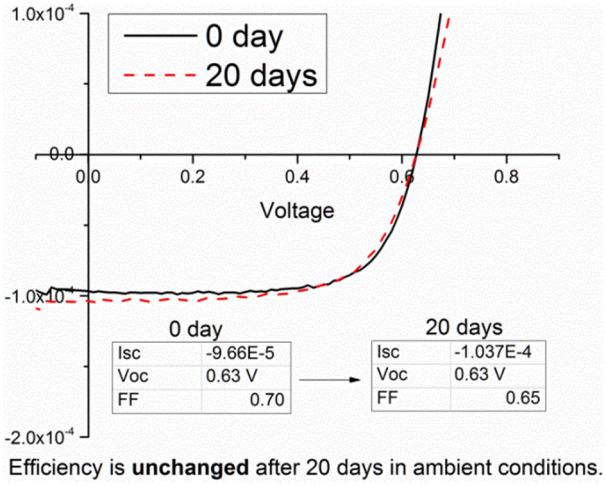

Fig. 4-5-6 *I-V* curve of P3HT/PCBM solar cell measured at the beginning (0 day) and 20 days later.

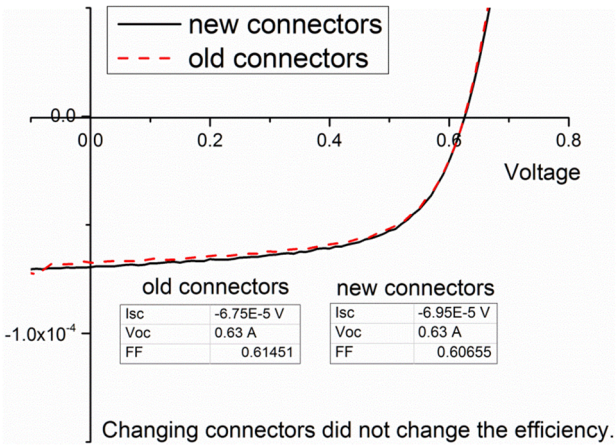

Fig. 4-5-7 *I-V* curve of P3HT/PCBM solar cell measured with old and new electrical connectors

4.5.2 Device Testing

4.5.2.1 e-PT/ZnO Device

Photovoltaic *J-V* device testing (Fig. 4-5-8, Table 4-5-1) was performed on e-PT/ZnO bilayer and nanorod structures, with and without a hole injection layer, PEDOT:PSS. It should be noted that unsubstituted PT without side chains is not an ideal polymer for a high efficiency solar cell. It is, however, a simple model system that we use to develop a more comprehensive understanding of bonding, structure and optoelectronic response, all key components of a polymer solar cell.

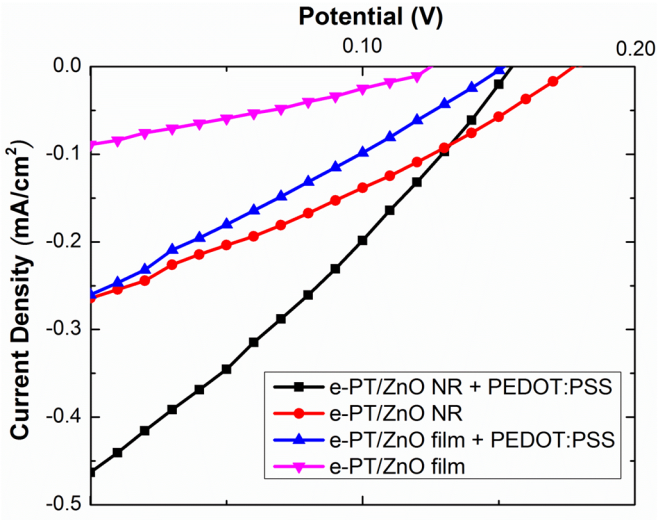

Fig. 4-5-8. *J-V* characterization of e-PT/ZnO solar cells. NR: nanorod.

Table 4-5-1. Device Parameters of e-PT/ZnO Solar Cells

sample	PEDOT:PS	J_{sc}	V_{oc} (V)	FF	PCE (%)
e-PT/ZnO	No	0.089	0.13	0.29	0.003
e-PT/ZnO	Yes	0.260	0.16	0.25	0.011
e-PT/ZnO	No	0.264	0.18	0.29	0.014
e-PT/ZnO	Yes	0.463	0.16	0.28	0.021

All e-PT samples were electropolymerized in acetonitrile with Bu_4NPF_6 as the electrolyte at a fixed polymerization charge of 75 mC which produces a thick polymer overlayer (~150 nm) on top of the ZnO nanorods. This overlayer acts as an electron blocking layer and prevents nanorods "poking through" the polymer and shorting the device. The nanostructured devices performed significantly better than the planar bilayer structures. This improvement, which shows up as a higher J_{sc}, occurs mainly because the ZnO nanorods improve the surface area of the organic-inorganic interface, enabling more charge separation and less recombination.[103] The conduction bands of the ZnO film and

nanorods are expected to be similar, therefore there should be little variation in V_{oc} between the bilayer and nanostructure active layers. The function of the hole injection layer, PEDOT:PSS, is to block the electrons from reaching the Ag electrode and thus reduce the leakage current and increase J_{sc} without sacrificing V_{oc} or FF. There, as expected, the efficiencies for devices with PEDOT:PSS are higher than those without such a layer due to a higher J_{sc}. The Ag/e-PT/PEDOT:PSS/ZnO NR/ZnO film/ITO device architecture is shown in Fig. 4-5-9.

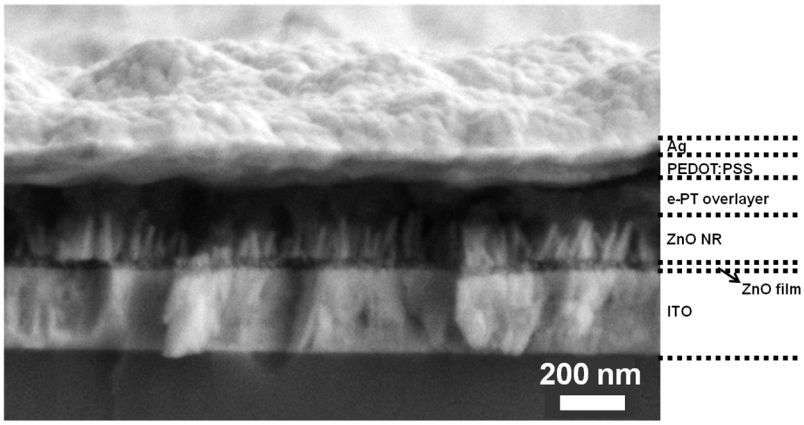

Fig. 4-5-9. Cross sectional SEM image of a typical Ag/e-PT/PEDOT:PSS/ZnO NR/ZnO film/ITO device.

Relatively low J_{sc} values indicate that the carrier mobility in the e-PT layer is poor. The e-PT film generally has carrier mobilities orders of magnitude lower than those of commercially available regioregular-P3HT,[7] which has relatively narrow polydispersity and low impurity concentrations (which comes from rigorous purification). XRD analysis of the e-PT/ZnO nanorods/ITO sample shows a broad peak instead of distinct sharp peaks, indicating low regioregularity and low crystallinity (Fig. 4-5-10). Electropolymerization produces regiorandom polymers with structural defects

such as crosslinking between adjacent chains. This results in a disruption to the conjugation length, poor chain packing, low crystallinity and low carrier mobilities. This is especially severe for thicker films, as the accumulation of structural defects increasingly degrades the electronic properties of the polymer.[104, 105]

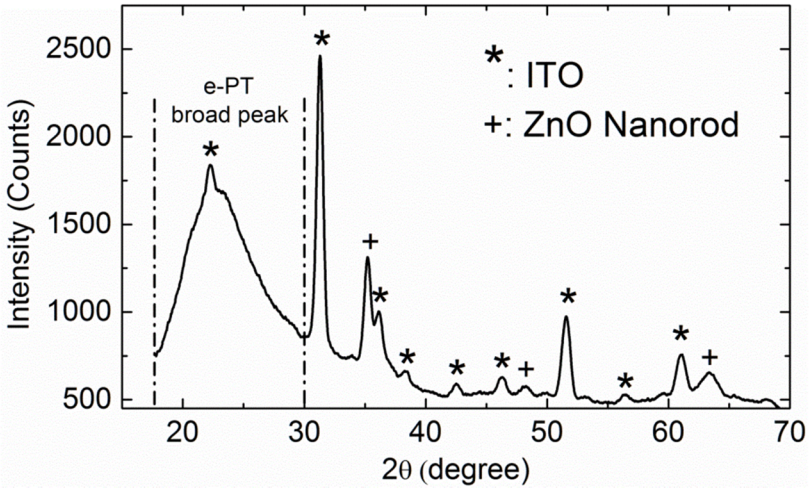

Fig. 4-5-10. XRD analysis of e-PT/ZnO nanorod/ITO sample. "+" signs indicates expected peaks from ZnO nanorods, while "*" signs indicate expected peaks from ITO substrate. The e-PT diffraction peak appears broad between the 2θ=20° and 2θ=30°.

Based on the above discussion, thinner polymer films that are more crystalline and compact will translate to higher carrier mobilities and fewer structural defects, resulting in better performing devices. The initial intention of growing a thick polymer overlayer originated from studies on P3HT/ZnO nanorods, in which the authors found that a polymer overlayer of a certain thickness (~250 nm) functions as an electron-blocking layer and improves the device efficiency.[50] However, the e-PT overlayer has a

much lower mobility than P3HT. It may still function as an electron blocking layer, but overall it is detrimental to the device performance.

In the several cases reported prior to our work, PV devices fabricated from electropolymerized polymers on high aspect ratio nanostructures usually consist of a thin polymer layer grown along the nanorods instead of a thick polymer overlayer grown above the nanorod arrays, as is in our devices.[7-11] The developing consensus in the literature, supported by our results, is that thin layers of electropolymerized polymer grown along the nanostructure surface, circumvents the inherent problem with electropolymerization for thicker polymeric layers and preserves the surface-initiating advantage of such a polymerization method to achieve high filling rates in the dense nanorod arrays. Unfortunately working with ultrathin layers may result in shunting problems.

4.5.2.1 P3HT/ZnO Device

For comparison purposes, we also fabricated regioregular-P3HT/ZnO solar cells. The regioregular electronic grade P3HT is purchased from Rieke Metals. A 30 mg/mL solution of P3HT in 1,2-dichlorobenzene is spin coated onto ZnO substrate with a spin speed of 1000 rpm for 60 seconds. The as-coated samples were allowed to dry slowly in a sealed Petri dish for 1 hour, followed by thermal annealing in a tube furnace at 225 °C for 1 minute in argon. Similarly to e-PT/ZnO devices, *J-V* characterization of P3HT/ZnO devices (Fig. 4-5-11) shows that the efficiency improved upon incorporation of PEDOT:PSS layer, as well as the usage of nanorod substrate instead of film substrate.

This confirms a universal theme that the hybrid devices benefit from the electron blocking layer (PEDOT:PSS) and a higher interface surface area (ZnO nanorod substrate vs. planar substrate).

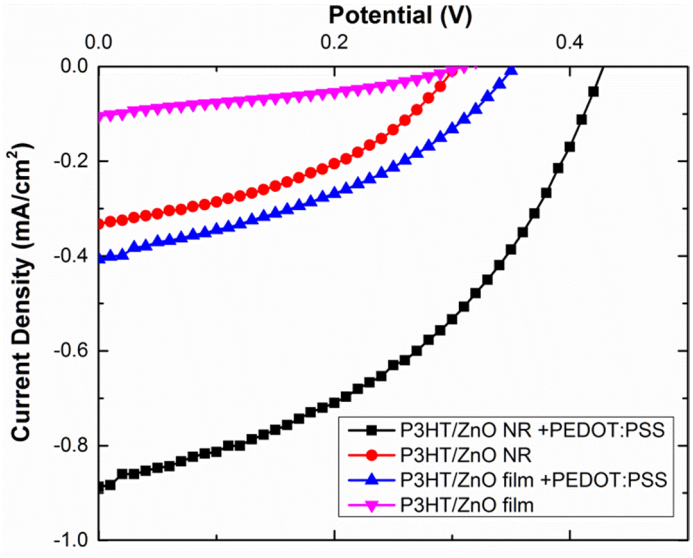

Fig. 4-5-11 *J-V* characterization of P3HT/ZnO solar cells

4.5.3 Aging Effect

Whereas all of the e-PT/ZnO solar cells showed a decreased efficiency after aging in the dark in ambient conditions (Table 4-5-2), most P3HT/ZnO devices showed an increase in efficiency with the exception of P3HT/PEDOT:PSS/ZnO NR device (Table 4-5-3, Fig. 4-5-12). This efficiency increase after aging in P3HT/ZnO solar cell has been well documented in the literature.[106] Within the P3HT/ZnO devices, those incorporating a layer of PEDOT:PSS show a much smaller efficiency gain or even an efficiency decrease compared to those without. This is most likely caused by the intrinsic acidity of

PEDOT:PSS which can initiate degradation within the solar cell.[107] The reason that all of the e-PT solar cells showed a reduced photovoltaic performance after aging is unclear and will be the subject of further investigation. We can only hypothesize at the moment: P3HT chains have some liberty of moving and adopting a better morphology and increasing its carrier mobility during aging. However, the e-PT chains are relatively rigid due to potential crosslinking side reactions and cannot move as freely as the P3HT.

Table 4-5-2. e-PT/ZnO Device Parameters with Aging Effect

	I_{sc} (A)	J_{sc} (mA/cm^2)	V_{oc} (V)	FF	PCE (%)
ZnO NR					
PT+PEDOT:PSS	1.39×10^{-5}	0.463	0.16	0.28	0.0209
PT+ PEDOT:PSS (14 days later)	1.15×10^{-5}	0.383	0.06	0.24	0.0055
PT	7.93×10^{-5}	0.264	0.18	0.29	0.0138
PT (5 days later)	3.26×10^{-6}	0.109	0.05	0.20	0.0011
PT (22 days later)	3.76×10^{-6}	0.125	0.03	0.22	0.00084
ZnO Film					
PT+PEDOT:PSS	7.81×10^{-6}	0.260	0.16	0.25	0.0105
PT+PEDOT:PSS (24 days later)	8.58×10^{-6}	0.286	0.06	0.22	0.0038
PT	2.67×10^{-6}	0.089	0.13	0.29	0.0034
PT (24 days later)	2.16×10^{-6}	0.072	0.04	0.23	0.00066

Table 4-5-3. P3HT/ZnO Device Parameters with Aging Effect

	I_{sc} (A)	J_{sc} (mA/cm^2)	V_{oc} (V)	FF	PCE (%)
ZnO NR					
P3HT+PEDOT:PSS	2.66×10^{-5}	0.887	0.43	0.42	0.162
P3HT+PEDOT:PSS (5 days later)	2.03×10^{-5}	0.677	0.39	0.43	0.113
P3HT	1.00×10^{-5}	0.333	0.31	0.40	0.041
P3HT (10 days later)	2.25×10^{-5}	0.750	0.36	0.41	0.111
ZnO Film					
P3HT+PEDOT:PSS	1.22×10^{-5}	0.407	0.36	0.37	0.055
P3HT+PEDOT:PSS (5 days later)	1.44×10^{-5}	0.480	0.32	0.37	0.057
P3HT	3.14×10^{-6}	0.105	0.31	0.33	0.011
P3HT (5 days later)	7.60×10^{-6}	0.253	0.30	0.38	0.029

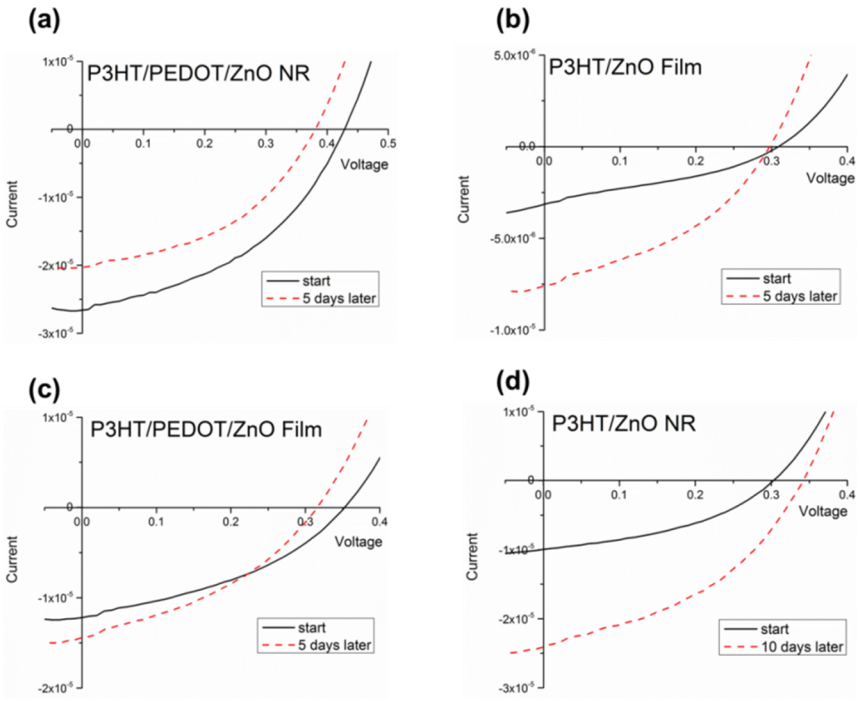

Fig. 4-5-12 *I-V* characterization of P3HT/ZnO solar cells and aging effect

4.5.4 Are FF and V_{oc} Correlated?

The e-PT/ZnO film devices were used to dissect whether there is a correlation between FF and V_{oc}. For e-PT devices synthesized in BF_4^-, there appears to be a rather weak or no correlation between FF and V_{oc} (Table 4-5-4). Lower FF samples (FF < 0.30) tend to have lower V_{oc} values, the average being 0.41 V. Higher FF samples (FF > 0.30) tend to have higher V_{oc}, the average being 0.47 V. The difference in FF of 0.09 yielded a slighter difference in V_{oc} of 0.06, meaning that there is a rather weak correlation between FF and V_{oc}.

Additionally, if we examine the aging effect of two particular samples listed in the Table 4-5-4, there appears to be a weak correlation or no correlation between the FF and V_{oc}. For sample 130329_4_1, aging for 3 days improved the FF by 0.10 but V_{oc} improved a very modest 0.03 V. For sample 130326_6_4, aging for 4 and 8 days brought an improvement in FF by 0.04 and 0.06, respectively. However, the V_{oc} values for the aged devices show no change at all from the original device. For this particular sample, it appears that V_{oc} has already reached a maximum value which is determined by the energy alignment at the interface and further FF enhancement was not able to push V_{oc} any higher.

For e-PT/ZnO devices in which e-PT was synthesized in ClO_4^-, there is again no observable correlation between FF and V_{oc}. The highest FF of 0.37 only yielded a modest V_{oc} at 0.29 V. The highest V_{oc} of 0.36 V, on the other hand, is accompanied by an equally modest FF of 0.32.

In summary, the correlation between the V_{oc} and FF appears to be weak or non-existing for our e-PT/ZnO device system.

Table 4-5-4. e-PT/ZnO film devices with e-PT synthesized in BF_4^-

Sample Names	FF	V_{oc}
130405_3_2bd	0.27	0.40
130329_4_1	0.25	0.41
130329_4_1 (3 days later)	0.35	0.44
130405_3_4	0.27	0.42
130405_6_4	0.36	0.47
130326_6_4	0.32	0.48
130326_6_4 (4 days later)	0.36	0.48
130326_6_4 (8 days later)	0.38	0.48
	Average FF	Average V_{oc}
For lower FF devices (FF<0.30)	0.26	0.41
For higher FF devices (FF>0.30)	0.35	0.47

Table 4-5-5. e-PT/ZnO film devices with e-PT synthesized in ClO_4^-

Sample Names	FF	V_{oc}
130405_1_6d2	0.30	0.19
130413_6_3redo3	0.32	0.36
130413_6_3redo3 (2 days later)	0.31	0.23
130330_5_1	0.34	0.30
130330_5_1 (4 days later)	0.31	0.24
130412_6_3	0.37	0.29

4.5.5 Device Performance Dependence on Polymer Layer Thickness

The e-PT/ZnO film device testing was carried out for different thicknesses of polymer layers synthesized in ClO_4^-; device parameters are listed in Table 4-5-6. The FF and V_{oc} are very similar for the two samples. The lower polymerization charge sample, corresponding to a thinner polymer layer, shows inferior I_{sc} and yields lower efficiency relative to the thicker polymer device. A thicker polymer will be more efficient in blocking the wrong charges reaching the electrode and, in effect, increase the I_{sc} values.[50]

We obtained similar results with e-PT/ZnO film devices with the e-PT layer synthesized in BF_4^-: the lower polymerization charge polymer showed lower performance (Table 4-5-7). The most notable difference between the two devices is in the I_{sc}, which is again similar to the ClO_4^- polymers. The FF and V_{oc} also improved slightly in this case.

In summary, based on the investigations on the ClO_4^- and BF_4^- polymers, we can conclude that the thicker polymer layer will assist electron blocking and results in a higher I_{sc} which translates to a higher efficiency.

Table 4-5-6. e-PT/ZnO Film Devices with Different Thicknesses of e-PT synthesized in ClO_4^-

Sample Names	Polymerization Charge (mC)	I_{sc} (A)	FF	V_{oc} (V)	PCE (%)
130406_1_4d3	25	1.99×10^{-6}	0.28	0.19	0.0035
130405_1_6d2	50	2.66×10^{-6}	0.30	0.19	0.0051

Table 4-5-7. e-PT/ZnO Film Devices with Different Thickness of e-PT synthesized in BF_4^-

Sample Names	Polymerization Charge (mC)	I_{sc} (A)	FF	V_{oc} (V)	PCE (%)
130413_2_5d (2 days later)	25	5.85×10^{-7}	0.33	0.43	0.0027
130326_6_4 (8 days later)	50	9.54×10^{-7}	0.38	0.48	0.0058

4.5.6 The Effect of Thermal Annealing

The e-PT/ZnO film devices in which e-PT was synthesized in ClO_4^-, showed an enormous increase of V_{oc} and FF upon annealing at 150 °C for 1 hour (Fig. 4-5-13, Table 4-5-8). However, the efficiency decreases for longer annealing times at the same temperature, mainly through the decrease of FF. If a higher temperature annealing is adopted (300 °C for 1 hour), the device suffers from a complete loss of PV activity (data not shown), which indicates that at 300 °C the polymer has been damaged. Our finding shows that the device can be improved upon thermal annealing, however, the annealing temperature as well as the duration needs to be carefully studied so that the performance can be optimized.

Our best e-PT/ZnO film device after thermal annealing has the same order of efficiency as P3HT/ZnO film solar cells (Table 4-5-3). In fact, it has a higher FF and V_{oc} than the best P3HT/ZnO sample we made. The I_{sc} for e-PT is not as good as that for P3HT (3.15×10^{-6} vs. 7.60×10^{-6} A), which is attributed to the lower carrier mobility of the

electropolymerized polymers in general compared to the regioregular polymers. This indicates that our e-PT/ZnO film device is highly optimized and by changing to a higher carrier mobility polymer than e-PT there is clear potential for significant further improvement in the I_{sc} and efficiency.

On the other hand, the e-PT/ZnO film devices in which e-PT was synthesized in BF_4^- show an efficiency that is essentially unchanged after annealing at 150 °C for 1 hour (Fig. 4-5-14). This different thermal annealing response in the two polymers devices, reflects the difference in the BF_4^- and ClO_4^- polymer devices, which has been extensively examined in the previous chapter.

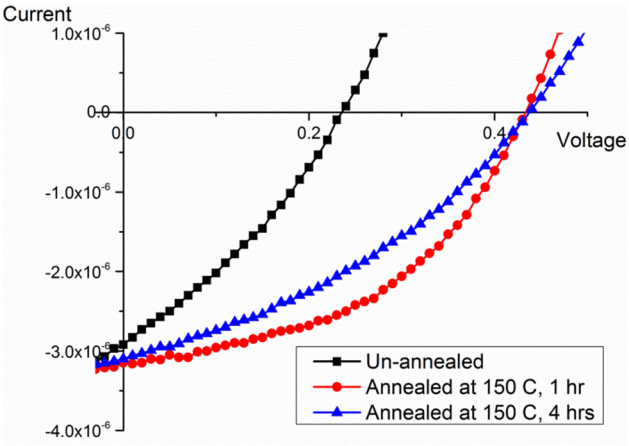

Fig. 4-5-13 *I-V* characterization of e-PT/ZnO film devices in which e-PT was synthesized in ClO_4^- (un-annealed, annealed at 150 °C for 1 hour or 4 hours).

Table 4-5-8. Device parameters for e-PT/ZnO film devices in which e-PT was synthesized in ClO_4^-

Sample Name	I_{sc} (A)	FF	V_{oc} (V)	PCE (%)
un-annealed	2.92×10^{-6}	0.31	0.24	0.0073
annealed at 150 °C for 1 hour	3.15×10^{-6}	0.46	0.44	0.0211
annealed at 150 °C for 4 hour	3.10×10^{-6}	0.36	0.44	0.0162

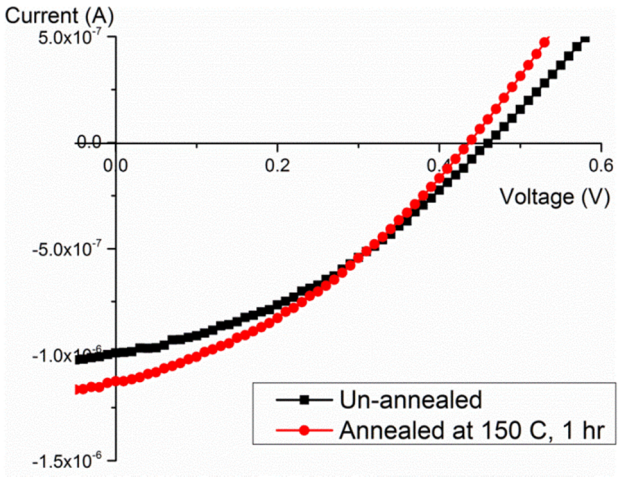

Fig. 4-5-14 *I-V* characterization of e-PT/ZnO film devices in which e-PT was synthesized in BF_4^- (un-annealed and annealed at 150 °C for 1 hour).

Table 4-5-9. Device parameters for e-PT/ZnO film devices in which e-PT was synthesized in BF_4^-

Sample Name	I_{sc} (A)	FF	V_{oc} (V)	PCE (%)
un-annealed	9.92×10^{-7}	0.38	0.48	0.0058
annealed at 150 °C for 1 hour	1.13×10^{-6}	0.35	0.44	0.0059

[Portion of this section is adapted with permission from Ref (47). Copyright (2013) American Chemical Society.]

References:

1. K. P. Loh and S. J. Chua, *Molecular Building Blocks for Nanotechnology*, Springer, New York, 2007.
2. M. H. Huang, Y. Wu, H. Feick, N. Tran, E. Weber and P. Yang, *Adv. Mater.*, 2001, **13**, 113-116.
3. W. I. Park, G.-C. Yi, M. Kim and S. J. Pennycook, *Adv. Mater.*, 2002, **14**, 1841-1843.
4. L. Vayssieres, *Adv. Mater.*, 2003, **15**, 464-466.
5. L. Vayssieres, K. Keis, A. Hagfeldt and S.-E. Lindquist, *Chem. Mater.*, 2001, **13**, 4395-4398.
6. R. Gonzalez-Moreno, P. L. Cook, I. Zegkinoglou, X. Liu, P. S. Johnson, W. Yang, R. E. Ruther, R. J. Hamers, R. Tena-Zaera, F. J. Himpsel, J. E. Ortega and C. Rogero, *J. Phys. Chem. C*, 2011, **115**, 18195-18201.
7. D. Xi, H. Zhang, S. Furst, B. Chen and Q. Pei, *J. Phys. Chem. C*, 2008, **112**, 19765-19769.
8. B. Sun, Y. Hao, F. Guo, Y. Cao, Y. Zhang, Y. Li and D. Xu, *J. Phys. Chem. C*, 2011, **116**, 1395-1400.
9. C. J. Harris, W. J. Belcher and P. C. Dastoor, *Sol. Energy Mater. Sol. Cells*, 2007, **91**, 1127-1136.
10. G. Mariani, R. B. Laghumavarapu, B. T. d. Villers, J. Shapiro, P. Senanayake, A. Lin, B. J. Schwartz and D. L. Huffaker, *Appl. Phys. Lett.*, 2010, **97**, 013107.

11. M. Giacomo, Y. Wang, P.-S. Wong, A. Lech, C.-H. Hung, J. Shapiro, S. Prikhodko, M. El-Kady, R. B. Kaner and D. L. Huffaker, *Nano Lett.* , 2012, **12**, 3581-3586.
12. K. Ogata, T. Hama, K. Hama, K. Koike, S. Sasa, M. Inoue and M. Yano, *Appl. Surf. Sci.*, 2005, **241**, 146-149.
13. O. Taratula, E. Galoppini, D. Wang, D. Chu, Z. Zhang, H. Chen, G. Saraf and Y. Lu, *J. Phys. Chem. B*, 2006, **110**, 6506-6515.
14. P. W. Sadik, S. J. Pearton, D. P. Norton, E. Lambers and F. Ren, *J. Appl. Phys.*, 2007, **101**, 104514.
15. C. L. Perkins, *J. Phys. Chem. C*, 2009, **113**, 18276-18286.
16. G. Liu, J. A. Rodriguez, J. Hrbek, B. T. Long and D. A. Chen, *J. Mol. Catal. A: Chem.*, 2003, **202**, 215-227.
17. T. Jirsak, J. Dvorak and J. A. Rodriguez, *J. Phys. Chem. B*, 1999, **103**, 5550-5559.
18. J. Ivanco, T. Haber, J. R. Krenn, F. P. Netzer, R. Resel and M. G. Ramsey, *Surf. Sci.*, 2007, **601**, 178-187.
19. M. A. Loi, E. D. Como, F. Dinelli, M. Murgia, R. Zamboni, F. Biscarini and M. Muccini, *Nat. Mater.*, 2005, **4**, 81-85.
20. N. Sai, K. Leung and J. R. Chelikowsky, *Phys. Rev. B*, 2011, **83**, 121309.
21. Y. Lee, Y. Zhang, S. L. G. Ng, F. C. Kartawidjaja and J. Wang, *J. Am. Ceram. Soc.* , 2009, **92**, 1940-1945.
22. L. E. Greene, M. Law, D. H. Tan, M. Montano, J. Goldberger, G. Somorjai and P. Yang, *Nano Lett.*, 2005, **5**.
23. B. L. Funt and S. V. Lowen, *Synth. Met.*, 1985, **11**, 129-137.
24. R. J. Waltman, J. Bargon and A. F. Diaz, *J. Phys. Chem.*, 1983, **87**, 1459-1463.
25. M. A. del Valle, P. Cury and R. Schrebler, *Electrochimica Acta*, 2002, **48**, 397-405.
26. D. Barreca, E. Tondello, D. Lydon, T. R. Spalding and M. Fabrizio, *Chem. Vap. Deposition*, 2003, **9**, 93-98.
27. J. Heeg, C. Kramer, M. Wolter, S. Michaelis, W. Plieth and W.-J. Fischer, *Appl. Surf. Sci.*, 2001, **180**, 36-41.
28. G. Morea, L. Sabbatini, P. G. Zambonin, A. J. Swift, R. H. West and J. C. Vickerman, *Macromolecules*, 1991, **24**, 3630-3637.
29. P. Dannetun, M. Boman, S. Stafstrom, W. R. Salaneck, R. Lazzaroni, C. Fredriksson, J. L. Bredas, R. Zamboni and C. Taliani, *J. Chem. Phys.*, 1993, **99**, 664-672.
30. K. Demirkan, A. Mathew, C. Weiland, M. Reid and R. L. Opila, *J. Appl. Phys.*, 2008, **103**, 034505.
31. S. Tanuma, T. Shiratori, T. Kimura, K. Goto, S. Ichimura and C. J. Powell, *Surf. Interface Anal.*, 2005, **37**, 833-845.
32. O. Dulub, U. Diebold and G. Kresse, *Phys. Rev. Lett.*, 2003, **90**, 016102.
33. A. I. Martin-Concepcion, F. Yubero, J. P. Espinos, A. R. Gonzalez-Elipe and S. Tougaard, *J. Vac. Sci. Technol. A*, 2003, **21**, 1393-1398.
34. D. Briggs and M. P. Seah, eds., *Practical Surface Analysis* 2nd edn., John Wiley & Sons, West Sussex, 1990.
35. Y.-K. Lan and C.-I. Huang, *J. Phys. Chem. B*, 2009, **113**, 14555-14564.

36. A. Sugunan, H. C. Warad, M. Boman and J. Dutta, *J. Sol-Gel Sci. Techn.*, 2006, **39**, 49-56.
37. S. Xu, C. Lao, B. Weintraub and Z. L. Wang, *J. Mater. Res.*, 2008, **23**, 2072-2077.
38. W. C. Tsoi, S. J. Spencer, L. Yang, A. M. Ballantye, P. G. Nicholson, A. Turnbull, A. G. Shard, C. E. Murphy, D. D. C. Bradley, J. Nelson and J.-S. Kim, *Macromolecules*, 2011, **44**, 2944-2952.
39. O. Dulub, L. A. Boatner and U. Diebold, *Surf. Sci.*, 2002, **519**, 201-217.
40. V. E. Henrich and P. A. Cox, *The surface science of metal oxides*, Cambridge University Press, Cambridge, 1994.
41. S. Lany and A. Zunger, *Phys. Rev. Lett.*, 2007, **98**, 045501.
42. B. J. Coppa, R. F. Davis and R. J. Nemanich, *Appl. Phys. Lett.*, 2003, **82**, 400-402.
43. J. C. C. Fan and J. B. Goodenough, *J. Appl. Phys.*, 1977, **48**, 3524-3531.
44. K. Ogata, T. Komuro, K. Hama, K. Koike, S. Sasa, M. Inoue and M. Yano, *Appl. Surf. Sci.*, 2004, **237**, 348-351.
45. E. D. l. Rosa, S. Sepulveda-Guzman, B. Reeja-Jayan, A. Torres, P. Salas, N. Elizondo and M. J. Yacaman, *J. Phys. Chem. C*, 2007, **111**, 8489-8495.
46. J. A. Rodriguez and A. Maiti, *J. Phys. Chem. B*, 2000, **104**, 3630-3638.
47. W. Feng, A. S. Wan and E. Garfunkel, *J. Phys. Chem. C*, 2013, **117**, 9852-9863.
48. R. J. Waltman and J. Bargon, *Can. J. Chem*, 1986, **64**, 76-95.
49. F. Garnier, G. Tourillon, J. Y. Barraud and H. Dexpert, *J. Mater. Sci.*, 1985, **20**, 2687-2694.
50. L. Baeten, B. Conings, H.-G. Boyen, J. D'Haen, A. Hardy, M. D'Olieslaeger, J. V. Manca and M. K. V. Bael, *Adv. Mater.*, 2011, **23**, 2802-2805.
51. E. Poverenov, M. Li, A. Bitler and M. Bendikov, *Chem. Mater.*, 2010, **22**, 4019-4025.
52. R. Schrebler, P. Grez, P. Cury, C. Veas, M. Merino, H. Gomez, R. Cordova and M. A. del Valle, *J. Electroanal. Chem.*, 1997, **430**, 77-90.
53. M. C. Scharber, D. Muhlbacher, M. Koppe, P. Denk, C. Waldauf, A. J. Heeger and C. J. Brabec, *Adv. Mater.*, 2006, **18**, 789-794.
54. J. H. Lee, J.-H. Shin, J. Y. Song, W. Wang, R. Schlaf, K. J. Kim and Y. Yi, *J. Phys. Chem. C*, 2012, **116**, 26342-26348.
55. S. J. Han, A. A. D. T. Adikaari, K. D. G. I. Jayawardena, N. A. Nismy, Y. H. Kim, J. W. Kim, Y.-B. Hahn and S. R. P. Silva, *Appl. Phys. Lett.*, 2013, **102**, 081607.
56. M. J. Tan, S. Zhong, J. Li, Z. Chen and W. Chen, *ACS Appl. Mater. & Interfaces*, 2013, **5**, 4696-4701.
57. J. Roncali, *Chem. Rev.*, 1992, **92**, 711-738.
58. M. Gratzl, D. F. Hsu, A. M. Riley and J. Janata, *J. Phys. Chem.*, 1990, **94**, 5973-5981.
59. P. Marque, J. Roncali and F. Garnier, *J. Electroanal. Chem.*, 1987, **218**, 107-118.
60. S. A. M. Refaey and G. Schwitzgebel, *Des. Monomers Polym.*, 2000, **3**, 389-398.
61. G. Zotti, G. Schiavon, S. Zecchin, F. Sannicolo' and E. Brenna, *Chem. Mater.*, 1995, **7**, 1464-1468.
62. Y. Li, *J. Electroanal. Chem.*, 1997, **433**, 181-186.
63. S. H. Strauss, *Chem. Rev.* , 1993, **93**, 927-942.
64. R. Cordova, M. A. d. Valle, A. Arratia, H. Gomez and R. Schrebler, *J. Electroanal. Chem.*, 1994, **377**, 75-83.

65. G. Tourillon and Y. Jugnet, *J. Chem. Phys.*, 1988, **89**, 1905-1913.
66. L. F. Warren and D. P. Anderson, *J. Electrochem. Soc.*, 1987, **134**, 101-105.
67. J. R. Reynolds, S.-G. Hsu and H. J. Arnott, *J. Polym. Sci. Polym. Phys.*, 1989, **27**, 2081-2103.
68. M. Ohyama, H. Kozuka and T. Yoko, *Thin Solid Films*, 1997, **306**, 78-85.
69. G. Gritzner and J. Kuta, *Pure Appl. Chem.*, 1984, **56**, 461-466.
70. R. R. Gagne, C. A. Koval and G. C. Lisensky, *Inorg. Chem.*, 1980, **19**, 2854-2855.
71. M. Namazian, C. Y. Lin and M. L. Coote, *J. Chem. Theory Comput.*, 2010, **6**, 2721-2725.
72. J. O. M. Bockris and S. U. M. Khan, *Surface Electrochemistry - A Molecular Level Approach*, Plenum Press, New York, 1983.
73. D. A. Arena, F. G. Curti and R. A. Bartynski, *Surf. Sci.*, 1996, **369**, L117-L121.
74. M. W. Schmidt, K. K. Baldridge, J. A. Boatz, S. T. Elbert, M. S. Gordon, J. H. Jensen, S. Koseki, N. Matsunaga, K. A. Nguyen, S. J. Su, T. L. Windus, M. Dupuis and J. A. J. Montgomery, *J. Comput. Chem.*, 1993, **14**, 1347-1363.
75. A. D. Becke, *Phys. Rev. A*, 1988, **38**, 3098-3100.
76. C. Lee, W. Yang and R. G. Parr, *Phys. Rev. B*, 1988, **37**, 785-789.
77. A. D. Becke, *J. Chem. Phys.*, 1993, **98**, 5648-5652.
78. K. L. Schuchardt, B. T. Didier, T. Elsethagen, L. Sun, V. Gurumoorthi, J. Chase, J. Li and T. L. Windus, *J. Chem. Inf. Model.*, 2007, **47**, 1045-1052.
79. G. Horowitz and F. Garnier, *Solar Energy Materials*, 1986, **13**, 47-55.
80. A. Tsumura, H. Koezuka and T. Ando, *Synth. Met.*, 1988, **25**, 11-23.
81. F. Garnier, *Chem. Phys.* , 1998, **227**, 253-262.
82. T. Yamamoto, K.-I. Sanechika and A. Yamamoto, *Bull. Chem. Soc. Jpn.*, 1983, **56**, 1497-1502.
83. G. Schopf and G. Kobmehl, *Polythiophenes - Electrically Conductive Polymers*, Springer-Verlag, 1997.
84. B. J. Lindberg, K. Hamin, G. Johansson, U. Gelius, A. Fahlman, C. Nordling and K. Siegbahn, *Phys. Scr.* , 1970, **1**, 286-298.
85. C. D. Wagner, W. M. Riggs, L. E. Davis, J. F. Moulder and G. E. Muilenberg, *Handbook of X-Ray Photoelectron Spectroscopy*, Perkin-Elmer Corporation, Physical Electronics Division, Eden Prairie, 1979.
86. Y. T. Yin, W. X. Que and C. H. Kam, *J. Sol-Gel Sci. Technol.*, 2010, **53**, 605-612.
87. Y. Sun, J. H. Seo, C. J. Takacs, J. Seifter and A. J. Heeger, *Adv. Mater.*, 2011, **23**, 1679-1683.
88. E. Poverenov, M. Li, A. Bitler and M. Bendikov, *Chem. Mater.*, 2010, **22**, 4019-4025.
89. J. H. Kaufman, C. K. Baker, A. I. Nazzal, M. Flickner, O. R. Melroy and A. Kapitulnik, *Phys. Rev. Lett.*, 1986, **56**, 1932-1935.
90. S. Rangan, S. Coh, R. A. Bartynski, K. P. Chitre, E. Galoppini, C. Jaye and D. Fischer, *J. Phys. Chem. C*, 2012, **116**, 23921−23930.
91. X. T. Hao, T. Hosokai, N. Mitsuo, S. Kera, K. K. Okudaira, K. Mase and N. Ueno, *J. Phys. Chem. B*, 2007, **111**, 10365-10372.
92. E. L. Ratcliff, J. L. Jenkins, K. Nebesny and N. R. Armstrong, *Chem. Mater.*, 2008, **20**, 5796-5806.
93. K. Noori and F. Giustino, *Adv. Funct. Mater.*, 2012, **22**, 5089-5095.

94. K. Nishi, S. Arata, N. Matsumoto, S. Iijima, Y. Sunatsuki, H. Ishida and M. Kojima, *Inorg. Chem.*, 2010, **49**, 1517-1523.
95. R.-D. Schnebeck, E. Freisinger and B. Lippert, *Angew. Chemie. Int. Ed.*, 1999, **38**, 168-171.
96. A. M. Bond, S. R. Ellis and A. F. Hollenkamp, *J. Am. Chem. Soc.*, 1988, **110**, 5293-5297.
97. O.-S. Jung, Y. J. Kim, Y.-A. Lee, K.-M. Park and S. S. Lee, *Inorg. Chem.*, 2003, **42**, 844-850.
98. M. G. Hill, W. M. Lamanna and K. R. Mann, *Inorg. Chem.* , 1991, **30**, 4687-4690.
99. S. Braun, W. R. Salaneck and M. Fahlman, *Adv. Mater.*, 2009, **21**, 1450-1472.
100. A. Tada, Y. Geng, Q. Wei, K. Hashimoto and K. Tajima, *Nat. Mater.*, 2011, **10**, 450-455.
101. P. Ruankham, S. Yoshikawa and T. Sagawa, *Mater. Chem. Phys.* , 2013, **141**, 278-282.
102. W. Feng, S. Rangan, Y. Cao, E. Galoppini, R. A. Bartynski and E. Garfunkel, *J. Mater. Chem. A*, 2014, DOI: 10.1039/C4TA00937A.
103. L. E. Greene, M. Law, B. D. Yuhas and P. Yang, *J. Phys. Chem. C*, 2007, **111**, 18451-18456.
104. A. Yassar, J. Roncali and F. Garnier, *Macromolecules*, 1989, **22**, 804-809.
105. L. Micaroni, D. Dini, F. Decker and M.-A. D. Paoli, *J. Solid State Electrochem.*, 1999, **3**, 352-356.
106. D. C. Olson, S. E. Shaheen, R. T. Collins and D. S. Ginley, *J. Phys. Chem. C*, 2007, **111**, 16670-16678.
107. R. Steim, F. R. Kogler and C. J. Brabec, *J. Mater. Chem.*, 2010, **20**, 2499-2512.

Chapter 5. Summary and Conclusions

We used an electropolymerization method to improve the filling of a polymer inside a high density nanorod array. Enhancing the polymer filling fraction may be advantageous for hybrid solar cell applications because it produces a high surface area for charge separation. The e-PT films were examined by multiple techniques including electrochemical, optical, photoelectron, ion scattering, scanning probe and electron microscopy methods. The growth of ZnO film and nanorods were studied. In particular, the ZnO nanorod growth was found to be influenced by growth time, growth temperature and solution concentration.

5.1 Interfacial Bonding and Morphological Control

Interfacial bonding between e-PT film and ZnO planar/nanorod substrate was investigated by XPS. We found that the e-PT films were chemisorbed onto ZnO planar substrates via Zn-S bonding and adopt an upright molecular geometry on the surface. By contrast, there was little to no covalent bonding detected for e-PT films adsorbed on ZnO nanorod substrates. The different bonding nature of e-PT films to the two surfaces is mainly attributed to the different surface polarities: ZnO planar substrates have a polar Zn-(0001) surface, whereas ZnO nanorods have mostly non-polar $(10\bar{1}0)$ sidewalls. Point defects, predominantly oxygen vacancies in ZnO, were found to have a relatively insignificant influence on the adsorption behavior of e-PT films on ZnO surfaces.

The solvent used in electropolymerization was found to affect the final morphology of the e-PT films on ZnO nanorods. Highly conformal growth along the nanorods with intimate contact between the two phases was observed in e-PT films electrodeposited in dichloromethane (DCM). On the other hand, when the solvent is changed to acetonitrile (ACN), the film growth becomes less conformal and more nodular around the nanorods. The film morphological control was attained by changing the polarity of the solvent, with ACN being the more polar molecule and competing more strongly with the monomer for adsorption on the electrode and hence reducing monomer coverage. In this core-shell structure produced in DCM, the ZnO nanorods can serve as a template for the production of e-PT nanoscale testtubes with one end open and the other end closed, simply by the dissolution of the ZnO nanorods by HCl acid.

5.2 Photovoltaic Properties

Although our e-PT is not necessarily high performing polymeric material, it is studied as a model to help us understand the relationship between the interfacial energy level alignment and device parameters, and to shed light on OPV design rules with emphasis on the critical interface between the two phases. The nanostructured e-PT/ZnO devices show higher performance than their bilayer counterparts, because of the higher surface area and therefore manifested mainly as an increase in the J_{sc}. Devices with an electron blocking layer such as PEDOT:PSS showed a higher J_{sc} as well. After aging in dark in ambient conditions, the e-PT/ZnO devices have shown a decline in conversion efficiency, whereas similar P3HT/ZnO devices exhibited higher (without PEDOT:PSS layer) or similar efficiencies (with PEDOT:PSS layer) after aging. This is likely due to

different interaction between the polymer and the contact in these two systems (e-PT vs. P3HT). In the P3HT/ZnO devices, it also highlights the chemical instability of the PEDOT:PSS layer over time. Comparing the overall efficiency of P3HT and e-PT devices, the most significant difference lies with the J_{sc} value. The e-PT devices have one order of magnitude lower J_{sc} values, which points to a low regioregularity of the e-PT polymers relative to the highly regioregular P3HT polymers resulting in a much lower carrier mobility in the e-PT polymers. The FF and V_{oc} of these solar cells were found to be weakly correlated. Higher electrochemical charge (50 mC vs. 25 mC), which corresponds to a thicker polymer deposit, leads to higher J_{sc} value which results in higher efficiency. Post-production thermal annealing effect was investigated. We found that the for e-PT films synthesized with ClO_4^- electrolyte anion the device efficiency increased significantly by annealing at 150 °C for 1 hour, however, longer time annealing at this same temperature provided lower efficiency due mostly to the deterioration of FF, and higher temperature annealing at 300 °C rendered the device no PV activity. For e-PT films synthesized with BF_4^- electrolyte anion, it was found that annealing at 150 °C for 1 hour does not affect its efficiency, which is a different observation to the ClO_4^- polymer. This is possibly due to the influence of the electrolyte anion on the resulting polymer morphology and structure.

5.3 Energy Level Alignment

We have studied the effect of electrolyte anions on the structure of electrodeposited neutral polythiophene films on planar ZnO substrates, and on the energy level alignment at the polymer/ZnO interface. The origin of the anion effect arises from

its coordination with the relevant radical cations before the species undergo coupling reactions and form longer conjugation units. Our XPS studies have identified dissociation reactions under our electrochemical conditions, wherein F^- anions were produced and were presumably more strongly coordinating than the larger anions BF_4^- and PF_6^-. This scenario complicates a direct comparison of coordinating ability among these four anions based on coordination rules for weakly coordinating anions as used in our study.

Although the difference in the IP values for all relevant polymers remains small (0.2-0.3 eV), the interface dipole (energy offset in the vacuum levels between e-PT and ZnO) "pushed" the HOMO levels of the polymer down in two (BF_4^- and $CF_3SO_3^-$) of the four polymers, and resulted in a larger difference of 0.4-0.5 eV between the polymer HOMO level and ZnO CB. This latter observation is directly related to the photovoltaic properties of e-PT/ZnO hybrid solar cells as it represents the theoretical V_{oc}. The establishment of a correlation between the theoretical and actual V_{oc} values, further validates the model that V_{oc} is determined by the relative band alignment at the interface. Although the device efficiencies are relatively low, our fundamental studies using e-PT/ZnO as model photovoltaic systems have demonstrated the role of interface dipole in regulating solar cell properties, especially by controlling the V_{oc}.